UNIVERSITÄT FREIBURG
Fakultät für Physik

Analysis of Excited B Mesons with the OPAL Detector at LEP

by
K. F. Michael Thiergen

Address:
Hermann-Herder-Str. 3
D-79104 Freiburg i. Br.
Germany

Universität Freiburg
Fakultät für Physik
December 1999

Abstract

A comprehensive high-statistics analysis of the low lying non-strange excited B meson states is performed. From 4 million hadronic Z^0 decays recorded by the OPAL detector on and near to the Z^0 resonance, a sample of more than 570 000 inclusively reconstructed B mesons is selected making use of improved tagging and reconstruction methods. B^* mesons are reconstructed using the decay $B^* \to B\gamma$. About 9 000 reconstructed B^* candidates using photon conversions and more than 64 000 B^* candidates using photons detected in the electromagnetic calorimeter constitute the largest sample of B^* mesons to date. More than 20 000 orbitally-excited mesons B_J^* are reconstructed using $B\pi^\pm$ combinations. A new method is used to determine the $B\pi^\pm$ combinatorial background and its systematic uncertainty. The selected B^* candidates are used to obtain samples enriched or depleted in the decay $B_J^* \to B^*\pi^\pm(\pi)$, where the (π) notation refers to decay modes with or without a second accompanying pion. From the number of signal candidates in the $B\pi^\pm$ mass spectra of the two samples, the first measurement of the branching ratio of orbitally-excited B mesons decaying into $B^*\pi(\pi)$ is performed:

$$\mathrm{BR}(\mathrm{B}_J^* \to \mathrm{B}^*\pi(\pi)) = 0.85\,^{+0.26}_{-0.27} \pm 0.12\,,$$

where the first error is statistical and the second systematic. In the framework of Heavy Quark Symmetry, a fit to the total $B\pi^\pm$ mass spectrum and a simultaneous fit to the $B\pi^\pm$ mass spectra of the samples enriched or depleted in the decay $B_J^* \to B^*\pi^\pm(\pi)$ yield the mass and the width of the $B_1(3/2)$ state, as well as the branching ratio of orbitally-excited B mesons decaying into $B^*\pi$:

$$\begin{aligned} M(\mathrm{B}_1(3/2)) &= (\,5.738\,^{+\,0.005}_{-\,0.006} \pm 0.007\,)\ \mathrm{GeV}/c^2 \\ \Gamma(\mathrm{B}_1(3/2)) &= (\,18\,^{+\,15\,+\,36}_{-\,13\,-\,29}\,)\ \mathrm{MeV}/c^2 \\ \mathrm{BR}(\mathrm{B}_J^* \to \mathrm{B}^*\pi) &= 0.74\,^{+\,0.12\,+\,0.21}_{-\,0.10\,-\,0.16}\,. \end{aligned}$$

The first error indicates the statistical and the second error the systematic uncertainty. In a separate analysis, a search for the first radial excitation of B and B^* has been performed. An excess observed in the $B\pi^+\pi^-$ mass spectrum is interpreted as a combined signal of $B^{(*)\prime} \to B^{(*)}\pi^+\pi^-$ and $B_J^* \to B^{(*)}\pi^+\pi^-$ decays. The measured product branching ratio is

$$\mathrm{f}(\bar{\mathrm{b}} \to \mathrm{B}^{(*)\prime},\, \mathrm{B}_J^*) \cdot \mathrm{BR}(\mathrm{B}^{(*)\prime},\, \mathrm{B}_J^* \to \mathrm{B}^{(*)}\pi^+\pi^-) = 0.0350 \pm 0.0070 \pm 0.0095\ ,$$

where the first error is statistical and the second systematic. The notation "$B^{(*)\prime}$, B_J^*" refers to B', $B^{*\prime}$ *and* B_J^*.

Analyse angeregter B Mesonen mit dem OPAL Detektor am LEP

INAUGURAL-DISSERTATION
zur
Erlangung des Doktorgrades
der
Fakultät für Physik
der
Albert-Ludwigs-Universität Freiburg im Breisgau

vorgelegt von

K. F. Michael Thiergen

aus

Weilburg an der Lahn

Anschrift:
Hermann-Herder-Str. 3
D-79104 Freiburg i. Br.
Germany

Universität Freiburg
Fakultät für Physik
Dezember 1999

Dekan	Prof. Dr. K. Königsmann
Leiter der Arbeit	Prof. Dr. G. Herten
Referent	Prof. Dr. G. Herten
Koreferent	Prof. Dr. K. Runge

Tag der Verkündung des Prüfungsergebnisses: 15.02.2000

– Three quarks for Muster Mark!
Sure he hasn't got much of a bark
And sure any he has it's all beside the mark.
But O, Wreneagle Almighty, wouldn't un be a sky of a lark
To see that old buzzard whooping about for uns shirt in the dark
And he hunting round for uns speckled trousers around by Palmer- stown Park?
Hohohoho, moulty Mark!
You're the rummest old rooster ever flopped out of a Noah's ark
And you think you're cock of the wark.
Fowls, up! Tristy's the spry young spark
That'll tread her and wed her and bed her and red her
Without ever winking the tail of a feather
And that's how that chap's going to make his money and mark!
Overhoved, shrillgleescreaming. That song sang seaswans.

James Joyce, Finnegans Wake.

Contents

List of Figures

List of Tables

Chapter 1

Introduction

The Standard Model of elementary particle physics provides a theoretical structure which has worked splendidly until the end of the 20^{th} century. In the Standard Model, the fundamental constituents of matter are the leptons and the quarks. The latter carry colour charge and are therefore engaged in the strong interactions which have been successfully described by a non-Abelian gauge field theory called Quantum Chromo-dynamics. The study of mesons, which can be thought of bound state systems of a quark and an anti-quark provides critical insights into the nature of Quantum Chromo-dynamics in the confinement domain. In order to fully understand the strong interactions of hadrons, a control of the non-perturbative regime of Quantum Chromo-dynamics is most important. Unfortunately, to date no established method is able to cope with the non-perturbative regime although some promising attempts are available. Therefore, the study of bound states (hadrons) is still one of the most interesting and challenging topics in particle physics. An understanding of how Quantum Chromo-dynamics makes hadrons forms the basis for an (eventual) understanding of the origin of the forces between nucleons and thence of the origin of the matter surrounding us. One of the keys to progress in this field is the identification of the appropriate degrees of freedom of the system under study. This leads us directly to the study of B mesons: first, a meson is the simplest system to study the strong forces between quarks. Second, mesons composed of a heavy quark and a light quark have an additional internal spin-flavour symmetry resulting in theoretical predictions of well defined uncertainty. The heavy-light mesons can be compared with atoms, where the heavy quark plays the role of the nucleus and electromagnetic interactions are replaced by strong interactions. It turns out that B mesons without strangeness are the best realisations of the heavy quark limit in nature. Furthermore, the study of B mesons is one of the best opportunities to gain insight into the mechanism of CP violation and new physics beyond the Standard Model. In this context, the study of charge-flavour correlations of $\mathrm{B} - \pi^{\pm}$ pairs is of great interest since it provides a powerful experimental technique to determine the flavour of a B meson at production. The ability of this flavour tagging is strongly enhanced by the

existence of orbitally-excited B meson states.

This thesis deals with the analysis of excited B meson states, especially orbital excitations. The main goal is to gain insight into the composition of the predicted B_J^* four-state multiplet by exploiting additional experimental information, namely the detection of a B^* meson in the decay of a B_J^*. For the first time, a link between B^* and B_J^* production is established. This analysis is performed on the data taken in the years 1990-1995 on and near to the Z^0 peak with the OPAL detector at LEP. It became feasible with the great improvements of selection efficiencies of $Z^0 \to b\overline{b}$ decays, B meson reconstruction and photon detection. A large amount of time was spent on systematic studies, especially to achieve a better understanding of the combinatorial $B\pi$ background. Even in the rather clean environment of Z^0 decays, our lack of knowledge of the fragmentation process and the limited detector resolution makes it hard to obtain high precision results in this field. Nevertheless, part of the results presented in this work will most likely survive for quite a while, as the new b physics machines working on the $\Upsilon(4S)$ do not produce B_J^* and the detection of low energetic photons at hadron collider experiments is a very hard task.

After a short overview about selected topics on QCD, heavy quark physics and spectroscopy relevant for this thesis, the experimental setup, i.e. the LEP accelerator and the OPAL detector are described. The analysis part of this thesis starts with a description of the $Z^0 \to b\overline{b}$ selection and the B meson reconstruction. Then the identification of photons and charged pions is described and the reconstruction of vector mesons, B^*, and orbitally-excited mesons, B_J^*, is reviewed. The information of the B^* and B_J^* analyses is combined to obtain samples of B_J^* mesons enriched or depleted in their B^* content and $BR(B_J^* \to B^*\pi(\pi))$ is measured. A fit to the $B\pi$ mass spectra of the two samples is performed within the framework of Heavy Quark Symmetry to determine the mass and the width of one of the narrow B_J^* states as well as $BR(B_J^* \to B^*\pi)$. Also an analysis of the $B^{(*)}\pi\pi$ final state is summarised. Systematic uncertainties of all results are discussed in detail and finally a conclusion is given.

Chapter 2

Theoretical Concepts

2.1 The Standard Model of particle interactions

The **S**tandard **M**odel (SM) of particle interactions [1, 2, 3, 4, 5, 6, 7, 8, 9, 10] is a synthesis of three of the four forces of nature as listed in Table 2.1 and has been tested by experiment with extremely high precision[1]. The forces are described by quantum field gauge theories, each of which is characterised by a coupling constant. The principle of gauge invariance is one of the most important concepts used in modern particle theories and relates symmetries with conservation laws. Gravity is not included in the Standard Model. The extremely weak gravitational forces between elementary particles can be ignored compared to the other three forces and a successful renormalizable[2] quantum field theory of gravity has not yet been formulated. The fundamental fermionic constituents of matter are the six

interaction type	strength	mediator(s)	range
weak	$G_{\mathrm{F}} \simeq 10^{-5} m_{\mathrm{p}}^{-2}$	$\mathrm{W}^{\pm}$, Z^0	$\approx m_{\mathrm{W}}^{-1} \simeq 10^{-3}$ fm
electromagnetic	$\alpha_{\mathrm{em}} \simeq 1/137$	γ	∞
strong	$\alpha_{\mathrm{s}} \simeq 1$	8 gluons	confinement $\simeq 1$ fm
gravitation	$G_{\mathrm{N}} \simeq 5.9 \cdot 10^{-39}$	graviton (?)	∞

Table 2.1: *Phenomenology of the four basic particle interactions.*

quarks, u, d, s, c, b, t, each of which occurs in three colours, and the six leptons e, ν_{e}, μ, ν_{μ}, τ, ν_{τ}. The quarks and leptons all have spin $\frac{1}{2}$ and are classified into three generations of families. The interactions between these particles are mediated by vector boson fields: the eight gluons mediate strong interactions, the $\mathrm{W}^{\pm}$ and Z^0 mediate weak interactions, and the electromagnetic interactions are carried by the photon γ. The weak bosons acquire a mass through the Higgs mechanism,

[1] For an up-to-date review, see e.g. [11].

[2] Only renormalizable field theories are believed to produce useful results. The concept of renormalization is explained in Section 2.2.

and in the framework of the minimal Standard Model there exists one neutral Higgs particle which has not yet been seen experimentally[3]. The mathematical structure that describes the interactions of these constituents is a local gauge field theory with the gauge group $\mathrm{SU(3)_C \otimes SU(2)_L \otimes U(1)_Y}$ [4] which is realized at large energies $\gg$ 100 GeV. At low energies $\ll$ 100 GeV after spontaneous symmetry breaking only the colour and electromagnetic symmetries are present:

$$\mathrm{SU(3)_C \otimes SU(2)_L \otimes U(1)_Y} \stackrel{100\mathrm{GeV}}{\longrightarrow} \mathrm{SU(3)_C \otimes U(1)_{EM}} \; . \tag{2.1}$$

The 19 parameters that characterise the SM are six quark masses, three lepton masses, the $\mathrm{W}^{\pm}$ mass, the mass of the Higgs boson, three gauge coupling constants, three mixing angles and one CP violating phase and the QCD vacuum angle. The masses of the quarks and charged leptons do not follow any evident pattern. No neutrino masses and no mixing angles are assumed for the lepton sector. If the experimental evidence for neutrino oscillations [13] is confirmed in the near future, the Standard Model has to be modified to implement non-vanishing neutrino masses and additional mixing angles. To date experimental data allow several different neutrino-mass scenarios. Current and future experiments will take important steps toward completing the neutrino picture. In the following, the implications of non-vanishing neutrino masses are ignored.

In the framework of the Standard Model, charged weak currents are purely left-handed. The left-handed components of the fields are combined in doublets

$$\begin{pmatrix} \mathrm{u} \\ \mathrm{d}' \end{pmatrix}_{\mathrm{L}} \quad \begin{pmatrix} \mathrm{c} \\ \mathrm{s}' \end{pmatrix}_{\mathrm{L}} \quad \begin{pmatrix} \mathrm{t} \\ \mathrm{b}' \end{pmatrix}_{\mathrm{L}} \quad \begin{pmatrix} \nu_{\mathrm{e}} \\ \mathrm{e}^- \end{pmatrix}_{\mathrm{L}} \quad \begin{pmatrix} \nu_{\mu} \\ \mu^- \end{pmatrix}_{\mathrm{L}} \quad \begin{pmatrix} \nu_{\tau} \\ \tau^- \end{pmatrix}_{\mathrm{L}} \quad , \tag{2.2}$$

where the prime for the down-type quarks indicates that the SU(2) quark eigenstates are different from the QCD mass eigenstates. Right-handed components are arranged in fermion-singlets. The right-handed neutrino component ν_{R} is absent in this theory corresponding to the non-observation of right-handed neutrinos. In the SM, the charged current interactions of the W bosons with the quarks are given by

$$\mathcal{L} = \frac{1}{2}(\; W^+_{\mu} J^{\mu} \; + W^-_{\mu} J^{\mu} \;) \tag{2.3}$$

where the V-A current is given by

$$J_{\mu} \;=\; \frac{\mathrm{g_w}}{2\sqrt{2}} \; (\bar{\mathrm{u}}, \bar{\mathrm{c}}, \bar{\mathrm{t}}) \; \gamma_{\mu}(1-\gamma_5) \; \mathbf{V}_{\mathrm{CKM}} \; \begin{pmatrix} \mathrm{d} \\ \mathrm{s} \\ \mathrm{b} \end{pmatrix} \tag{2.4}$$

and the Fermi coupling constant is related to the SU(2) coupling as $\mathrm{G_F}/\sqrt{2} = \mathrm{g_w^2}/8\mathrm{M_W^2}$ obtained in the limit of small momentum transfer ($1 \gg q^2/M_W^2$). $\mathbf{V}$ is the

[3] The current 95% C.L. limit on the SM Higgs boson mass is already above 100 GeV/c^2 [12].

[4] The indices stand for C=colour, L=left-handed, Y=weak hypercharge.

3×3 Cabibbo-Kobayashi-Maskawa (CKM) matrix that has a simple representation in terms of the flavour transformation matrix

$$\mathbf{V}_{\mathrm{CKM}} = \begin{pmatrix} \mathrm{V_{ud}} & \mathrm{V_{us}} & \mathrm{V_{ub}} \\ \mathrm{V_{cd}} & \mathrm{V_{cs}} & \mathrm{V_{cb}} \\ \mathrm{V_{td}} & \mathrm{V_{ts}} & \mathrm{V_{tb}} \end{pmatrix} , \tag{2.5}$$

which relates the quark mass eigenstates with the left-handed SU(2) eigenstates, i.e. the d, s, b quarks (or equivalently the u, c, t quarks) mix under weak interactions.

For three generations the unitarity condition $\mathbf{V}\mathbf{V}^{\dagger} = \mathbf{1}$ imposes constraints. As a result there are only four independent parameters that can be expressed in terms of three angles and a CP violating phase. A phenomenologically more useful representation of this matrix is the Wolfenstein parameterisation which expands a given matrix element of $\mathbf{V}$ in powers of λ to $O(\lambda^4)$:

$$\mathbf{V}_{\mathrm{CKM}} = \begin{pmatrix} 1-\lambda^2/2 & \lambda & \lambda^3\mathrm{A}(\rho - \mathrm{i}\eta) \\ -\lambda & 1-\lambda^2/2 & \lambda^2\mathrm{A} \\ \lambda^3\mathrm{A}(1-\rho-\mathrm{i}\eta) & -\lambda^2\mathrm{A} & 1 \end{pmatrix} + O(\lambda^4). \tag{2.6}$$

with $\lambda = \mathrm{V_{us}} \sin\theta_c = 0.2196 \pm 0.0023$. θ_c is the Cabibbo angle describing the amount of two-dimensional quark mixing if only the d and s quark is considered. While λ is known to 1% accuracy from direct measurements, we have $A = 0.819 \pm 0.035$ and $\sqrt{\rho^2+\eta^2} = 0.36 \pm 0.09$ [14]. The elements $\mathrm{V_{td}}$ and $\mathrm{V_{ub}}$ of the CKM matrix given in Equation 2.6 are complex if $\eta \neq 0$, and as a result there exists a natural mechanism for CP-violation in the SM.

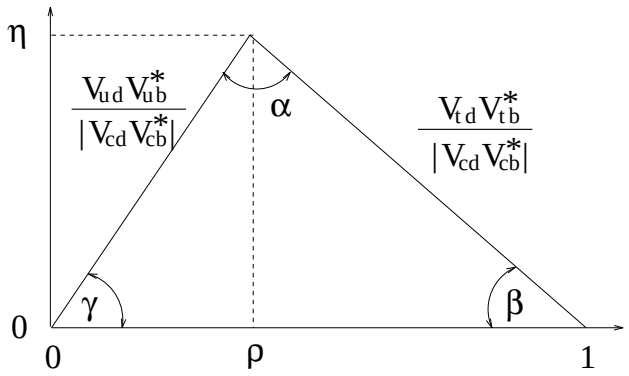

Figure 2.1: *The rescaled unitarity triangle with all sides divided by* $|\mathrm{V_{cd}V_{cb}^*}|$.

The unitarity of the CKM matrix defines relations among its elements. One relation of particular interest is

$$\mathrm{V_{ud}V_{ub}^* + V_{cd}V_{cb}^* + V_{td}V_{tb}^* = 0} , \tag{2.7}$$

which can be geometrically represented in the complex plane as a triangle, the so called *unitarity triangle*[5]. The rescaled unitarity triangle of Figure 2.1 is derived

[5]For a short introduction see e.g. [15].

from Equation 2.7 by choosing a phase convention such that $V_{cd}V_{cb}^*$ is real and dividing the lengths of all three sides by $|V_{cd}V_{cb}^*|$. Thus two corners of the unitarity triangle are $(0,0)$ and $(1,0)$. The coordinates of the remaining vertex are given by (ρ,η). Measurements of the CKM matrix elements related to the lengths and angles of the unitarity triangle determine the position (ρ,η). The area of the unitarity triangle is related to the SM CP violation. The constraints on the parameters defining the unitarity triangle will be largely improved by future B physics experiments. CP violation is one of the least tested aspects of the Standard Model and almost any extension of the SM provides new sources of CP violation.

2.2 Quantum Chromo-dynamics (QCD)

The basic idea of Quantum Chromo-dynamics is that the colour charges of the quarks act as sources of the chromo-dynamic force between quarks. As the quarks carry both colour and electrical charge, they experience both the strong and electromagnetic forces, as well as the weak interactions. Compared with electrodynamics, the situation is more complicated in the case of strong interactions, since two or three quarks have to be bound together on the basis of three different colours (and anti-colours) acting as colour charges to form the observed colour-neutral hadrons.

Quantum Chromo-dynamics [16, 17, 18] is the non-Abelian SU(3) gauge field theory which describes the strong interactions. A quark is described by a quantum field Dirac spinor ψ_j^α, where $\alpha = \mathrm{u,d,s,c,b,t}$ denotes the flavour and $j =$ red, green, blue the colour of the quark. The gauge bosons are called gluons and carry themselves a combination of colour and anti-colour. There exist eight different gluons and each is represented by a gauge field A_μ^a, $a = 1, ..., 8$. The (minimal) Lagrangian density describing the interactions of quarks and gluons is[6]

$$\mathcal{L} = -\frac{1}{4}F_a^{\mu\nu}F_{\mu\nu}^a + \sum_\alpha \bar{\psi}_j^\alpha (i\gamma^\mu D_{\mu,jk} - m^\alpha \delta_{jk})\psi_k^\alpha \,, \tag{2.8}$$

where repeated colour indices a summed over. The first term of $\mathcal{L}$ is a kinetic term consisting purely of the gauge fields which define the field strength tensor

$$F_{\mu\nu}^a = \partial_\mu A_\nu^a - \partial_\nu A_\mu^a - g_s f^{abc} A_\mu^b A_\nu^c \,, \tag{2.9}$$

where g_s is the QCD coupling constant and f^{abc} are the structure constants of the SU(3) algebra. A remarkable feature of the Lagrangian in Equation 2.8 is the appearance of self-interactions among the gauge fields through the last term in Equation 2.9 due to the non-Abelian structure of the symmetry group. The second term of the Lagrangian describes the fermion fields ψ_j^α in interaction with the gauge fields A_μ^a using the following definition of the covariant derivative:

$$D_{\mu,jk} = \delta_{jk}\partial_\mu - ig_s \sum_a \frac{\lambda_{jk}^a}{2} A_\mu^a \,. \tag{2.10}$$

[6] skipping gauge fixing terms

Here $\frac{\lambda^a_{jk}}{2}$ are the group generators of SU(3) transformations. The eight 3x3 matrices $\lambda^a_{jk} \equiv \boldsymbol{\lambda}_a$ obey the commutation and anti-commutation relations

$$[\boldsymbol{\lambda}_a, \boldsymbol{\lambda}_b] = 2if_{abc}\boldsymbol{\lambda}_c \tag{2.11}$$

$$\{\boldsymbol{\lambda}_a, \boldsymbol{\lambda}_b\} = \frac{4}{3}\delta_{ab}\mathbf{1} + 2d_{abc}\boldsymbol{\lambda}_c \tag{2.12}$$

with the totally antisymmetric structure constants f_{abc} and the totally symmetric coefficients d_{abc}. Note that the universal constant g_s defines the strength of all interactions in Equation 2.9 and Equation 2.10. The Lagrangian $\mathcal{L}$ is invariant under the local SU(3) transformations

$$\psi^\alpha(x) \rightarrow \mathbf{U}(x)\psi^\alpha(x) \tag{2.13}$$

$$A^a_\mu(x)\frac{\boldsymbol{\lambda}^a}{2} \rightarrow \mathbf{U}(x)A^a_\mu(x)\frac{\boldsymbol{\lambda}^a}{2}\mathbf{U}^{-1}(x) + \frac{i}{g_s}\mathbf{U}(x)\partial_\mu\mathbf{U}^{-1}(x) \tag{2.14}$$

$$\mathbf{U}(x) = \exp(i\theta^a(x)\frac{\boldsymbol{\lambda}^a}{2}) \, . \tag{2.15}$$

Here we have explicitly written the space-time dependence of ψ^α, A^a_μ, $\mathbf{U}$ and θ^a to stress the fact of *local* gauge invariance. Using the Lagrangian 2.8 the equations of motion for the quark and gluon fields can be obtained using the Euler-Lagrange formalism.

For a consistent quantum field theory involving non-Abelian gauge fields, the Lagrangian 2.8 is not yet complete. For the full Lagrangian of the theory, a (Lorentz-invariant) gauge fixing term $\mathcal{L}_{\text{gaugefix}}$ is required to ensure a proper quantisation procedure and a so called Fadeev-Popov ghost term $\mathcal{L}_{\text{ghost}}$ has to be added which depends on the choice of the gauge fixing and preserves unitarity. The term $\mathcal{L}_{\text{ghost}}$ describes an effective interaction in terms of unphysical "ghost" fields which occur only within loops and never appear as asymptotic states. The complete QCD Lagrangian is given by

$$\mathcal{L}_{\text{QCD}} = \mathcal{L} + \mathcal{L}_{\text{gaugefix}} + \mathcal{L}_{\text{ghost}} \tag{2.16}$$

For the Lagrangian 2.16 a complete set of Feynman rules can be derived and perturbative calculations of cross sections for arbitrary quark-gluon processes can be performed. The Feynman rules involve a total of four interaction vertices: two-quark-gluon vertex, three-gluon vertex, four-gluon vertex and two-ghost-gluon vertex. All four interaction vertices are described by the coupling strength g_s. The perturbation theory with the coupling g_s seems to work as good as QED. Since quarks and gluons are confined inside hadrons, the use of such calculations is limited to the regime of small g_s. It turns out that the lowest-order calculations reproduce the parton model results. Beyond the tree approximation, however, loop-contributions generate divergences which have to be taken care of by a *renormalization* procedure[7]. It has been proven that QCD is a renormalizable field

[7] This is of course not a specific QCD problem but also present in other theories such as QED.

theory. This means that there exists a well defined set of rules for calculating amplitudes which are free of ultraviolet divergences[8] order by order in the interaction coupling constant. To make the divergent integrals mathematically manageable for the final physical answer, a suitable convergence procedure has to be employed which is generically called *regularization*. The most commonly used method is the dimensional regularization. A divergent multiple integral may be made convergent by reducing the number of multiple integrals. In dimensional regularization the space-time dimension D is kept lower than four and all four-dimensional integrals are replaced by convergent D-dimensional ones.

In the subtraction of the mathematically controlled divergences, there exists an arbitrariness of how to define a divergent part. This arbitrariness lies in the fact that a specific scheme has to be used to subtract divergences and that a renormalization scale μ has to be chosen at which the subtraction is made. This results in many possible expressions for one physical quantity depending on the scheme and the fixed mass scale. Since all these expressions for a distinct physical quantity are derived starting from a unique Lagrangian, they should be equivalent. This is in fact true and different expressions obtained from different schemes and scales are connected by finite renormalizations. The divergences appearing in the integration procedure are manifest in the so called renormalization constants, Z_i. Writing this explicitly we obtain for the mass m and coupling constant $\mathrm{g_s}$ of Equation 2.8

$$g_{\mathrm{s}}^r(\mu) = Z_g^{-1}(\mu) \cdot \mathrm{g_s} \,, \quad m^r(\mu) = Z_m^{-1/2}(\mu) \cdot m \,, \tag{2.17}$$

where the index r indicates the renormalized quantities. A different scale μ' results in similar expressions. Now regarding the finite variation in renormalisation $\mu \to \mu'$ as a transformation it is obvious that such transformations form a group since the renormalization constants are multiplicative. This group is called the renormalisation group. Employing dimensional regularisation and regarding the bare parameters $\mathrm{g_s}$ and m as fixed constants, we obtain

$$\frac{\mathrm{d}\mathrm{g_s}}{\mathrm{d}\mu} = 0 \qquad \frac{\mathrm{d}m}{\mathrm{d}\mu} = 0 \tag{2.18}$$

We define the QCD coupling $\alpha_{\mathrm{s}} = g_{\mathrm{s}}^2/4\pi$ in analogy to the QED coupling. From Equations 2.17 and 2.18 the renormalization scale dependence of the effective coupling α_{s} can be derived[9] using the so called β-function:

$$\mu\frac{\partial\alpha_{\mathrm{s}}}{\partial\mu} = -\frac{\beta_0}{2\pi}{\alpha_{\mathrm{s}}}^2 - \frac{\beta_1}{4\pi^2}{\alpha_{\mathrm{s}}}^3 - \frac{\beta_2}{64\pi^3}{\alpha_{\mathrm{s}}}^4 - \dots \,, \tag{2.19}$$

$$\beta_0 = 11 - \frac{2}{3}n_f \,, \tag{2.20}$$

[8] Divergences which stem from very high momenta in e.g. loop integrals at short distances.

[9] For the calculation, dimensional regularisation and explicit expressions for the renormalization constants Z_i have to be used.

$$\beta_1 = 51 - \frac{19}{3} n_f \ , \tag{2.21}$$

$$\beta_2 = 2857 - \frac{5033}{9} n_f + \frac{325}{27} n_f^2 \ , \tag{2.22}$$

where n_f is the number of quark flavours with quark mass less than the energy scale μ. In solving this equation for α_s, a constant of integration is introduced. This constant is not predicted by QCD. It is the one fundamental parameter of QCD which must be deduced from experiment. The most common procedure is to introduce a dimensional parameter $\Lambda_{\overline{\rm MS}}$, and to write as a solution of Equation 2.19 in second order expansion

$$\alpha_s(\mu) = \frac{12\pi}{(33 - 2n_f) \cdot \ln(\frac{\mu^2}{\Lambda_{\overline{\rm MS}}^2})} \cdot \left(1 - 6 \cdot \frac{153 - 19n_f}{(33 - 2n_f)^2} \cdot \frac{\ln(\ln \frac{\mu^2}{\Lambda_{\overline{\rm MS}}^2})}{\ln(\frac{\mu^2}{\Lambda_{\overline{\rm MS}}^2})} + \mathcal{O}({\alpha_s}^3) \right) \ . \tag{2.23}$$

The index $\overline{\rm MS}$ refers to the so called modified minimal subtraction scheme. In this particular renormalization scheme the pole in the space-time dimension is subtracted off as well as the finite constant term $(\ln 4\pi - \gamma_{\rm E})$, where $\gamma_{\rm E}$ is the Euler-Mascheroni constant. It has become conventional to use the $\overline{\rm MS}$ scheme for calculating QCD cross sections beyond leading order.

At large scales μ, or equivalently at small distances, α_s vanishes logarithmically, an effect which is called asymptotic freedom. Note that the observed behaviour is opposite to the so called screening effect in QED, where the electromagnetic coupling increases with increasing scale. This QED effect is explained with the polarisation of the vacuum by a sea of electron-positron pairs in the environment of the electric charge under consideration. In fact, the electric charge is divergent for squared momentum transfer $q^2 \to \infty$ and has to be renormalized leaving a finite value for the classical electric charge. Also in QCD, quark-antiquark pairs cause a screening of the bare colour charge. Now the non-Abelian structure of QCD, which allows the self-interaction of gluons, causes a gluon shielding in addition to the quark-antiquark shielding. The special feature of the gluon shielding is that it acts opposite to the quark-antiquark shielding (*anti-screening*). This results in a decreasing of the coupling with increasing energy scale μ as long as $n_f < \frac{33}{2}$ (see Equation 2.23). Therefore, the quarks become asymptotically free at very small distances and they behave nearly as free particles within hadrons. At large distances on the other hand, the coupling becomes very large and this fact is of importance for the quark *confinement*, i.e. the observation that quarks only appear in $q\bar{q}$ pairs (Mesons) or qqq triple states (Baryons) to form colour singlets.

In regions where the strong coupling is sufficiently small, $\alpha_s \ll 1$, QCD may be solved by perturbation theory. At large distances however, α_s becomes very large such that perturbation theory no longer applies. In this region non-perturbative

methods must be used to describe the strong interactions. Such methods have not yet reached the same level of predictive power as perturbation theory in the large μ region. Therefore the QCD dynamics at large distances can be regarded as rather unsolved. Nevertheless, a considerable amount of different methods have been developed which are suitable for specific problems and specific energy scales. In the following Sections, several examples are presented. The emphasis is on methods which are useful to predict properties of excited B meson states.

2.3 Perturbative QCD: an example

The basic ideas of perturbative QCD have been explained in the previous section. From Equation 2.23 and its implications it is clear that the regime where perturbative QCD is applicable is rather restricted. Although perturbative QCD is not qualified to predict hadron properties, a simple example is presented here: the calculation of the ratio

$$R = \frac{\sigma(\mathrm{e^+e^-} \to \text{hadrons})}{\sigma(\mathrm{e^+e^-} \to \mu^+\mu^-)} \,. \tag{2.24}$$

Far away from any resonance, the electron and positron annihilate into a virtual photon which eventually decays into a muon pair. The corresponding cross section is given by

$$\sigma(\mathrm{e^+e^-} \to \mu^+\mu^-) = \frac{4\pi\alpha_{\mathrm{em}}^2}{3\,\mathrm{s}} \quad \text{with} \quad \mathrm{s} = E_{\mathrm{CM}}^2 \,. \tag{2.25}$$

In the case of a $\mathrm{q\bar{q}}$ final state instead of $\mu^+\mu^-$, the corresponding cross section is obtained taking into account the number of colours N_c and quark flavours n_f involved in the process. In lowest order, ignoring additional contributions to the Born cross sections, we obtain:

$$R_0 = N_c \cdot \sum_i^{n_f} q_i^2 \,. \tag{2.26}$$

For $\sqrt{\mathrm{s}} \geq 10$ GeV, experiments give values for R of around $\frac{11}{3}$, which is the expectation for two up and three down type quarks and a colour factor of $N_c = 3$. This is a nice confirmation for the hypothesis of three colour degrees of freedom and thus for the SU(3) structure of QCD. In the region of large $\sqrt{\mathrm{s}}$ a deviation from the constant behaviour of R is observed in experimental data. This discrepancy can be explained by higher order QCD corrections in R, which have been calculated in complete third order perturbation theory [19][10]

$$R = R_0 \cdot \left(1 + \frac{\alpha_{\mathrm{s}}}{\pi} + 1.4\left(\frac{\alpha_{\mathrm{s}}}{\pi}\right)^2 - 12.8\left(\frac{\alpha_{\mathrm{s}}}{\pi}\right)^3 + \mathcal{O}\left({\alpha_{\mathrm{s}}}^4\right)\right) \,. \tag{2.27}$$

[10] At higher centre-of-mass energies, the existence of the $\mathrm{Z^0}$ poles becomes more and more important and has to be considered in the calculation of R.

2.4 Non-perturbative methods

The non-perturbative nature of bound states such as mesons provokes the development of different approaches [15]. There is no complete solution for this problem. Rather, a variety of different theoretical approaches and techniques are available which are appropriate to a variety of specific problems and with varying levels of reliability. The available methods can be classified in three different categories. First, the category of effective field theories such as Chiral Perturbation Theory or Heavy Quark Symmetry (HQS), which make use of a small expansion parameter which is obtained by considering a particular limit or special kinematics. Second, theoretical approaches which are based on QCD such as lattice QCD or QCD sum rules. Although such techniques are rigourous, their practical use is limited due to a varying degree of uncontrolled model dependency. Third, we have the category of QCD inspired quark models. The advantage of such models is their flexibility in representing some behaviour of the true theory and they can be tuned to specific processes or hadronic states. The difficulty of quark models lies in the fact that it is difficult to access their reliability other than comparing them with measurements.

2.4.1 Lattice QCD

Lattice QCD [10] is Quantum Chromo-dynamics formulated on a discrete Euclidean space-time grid. The fundamental character of QCD is preserved since no new parameters of field variables are introduced. Lattice QCD has two important features. First, the discrete space-time lattice serves as a regularization scheme in providing a cutoff for ultraviolet divergences due to the finite lattice spacing a. In the limit $a \to 0$, renormalized physical quantities have well defined limits. Second, lattice QCD can be simulated on the computer using methods borrowed from Statistical Mechanics. The only input parameters for the simulation are the strong coupling α_s and the bare quark masses. Thus the results obtained from simulations can be studied in dependence of these input parameters. Lattice QCD calculations are based on the Feynman path integral approach. The starting point is the partition function in Euclidian space-time

$$Z = \int [\mathrm{d}A_\mu][\mathrm{d}\bar{\psi}^\alpha][\mathrm{d}\psi^\alpha] e^{iS(A_\mu, \bar{\psi}^\alpha, \psi^\alpha)} \,, \tag{2.28}$$

where the functional is over all configurations with given gauge potential A_μ and quarks ψ^α and $S(A_\mu, \bar{\psi}^\alpha, \psi^\alpha) = \int \mathrm{d}^4x \mathcal{L}_{\mathrm{QCD}}$ is the QCD action. Z is computed by replacing the continuous integration by a summation via discretizing space-time on a grid with spacing a. Given enough configurations of A_μ and ψ^α as well as a fine enough grid, this method provides an arbitrarily accurate solution to QCD. The masses and properties of all hadrons should be calculable with such a method. Another topic of special interest is the calculation of matrix elements occuring in the weak decays of hadrons since non-perturbative QCD corrections to the weak process become large due to soft gluon exchange.

The use of lattice QCD is limited due to several different difficulties. A practical limitation is the enormous amount of computer power needed to perform the calculations. Expecially the inclusion of quark loops makes such calculations extremely expensive. Computing time can be saved by working in the so called *quenched approximation*, where quark loops are neglected. The problem with this ansatz is the largely unknown effect on the results. Due to the enormous increase of computing power in the recent years, some unquenched calculations are feasible. Some other approximations like the use of large light quark masses of $\approx$ 100 MeV/c^2 to avoid singularities and extrapolating to $a \to 0$ and overall lattice size $\to \infty$ are believed to be well under control. In Figure 2.2 recent QCD lattice results [20] are compared with experimental data. The low-lying B meson states appear to be rather well calculated by the lattice calculation. The statistical errors of the calculations are still quite large, especially for higher excitations. Nevertheless, this is a very promising lattice QCD example and improved results are expected in the near future.

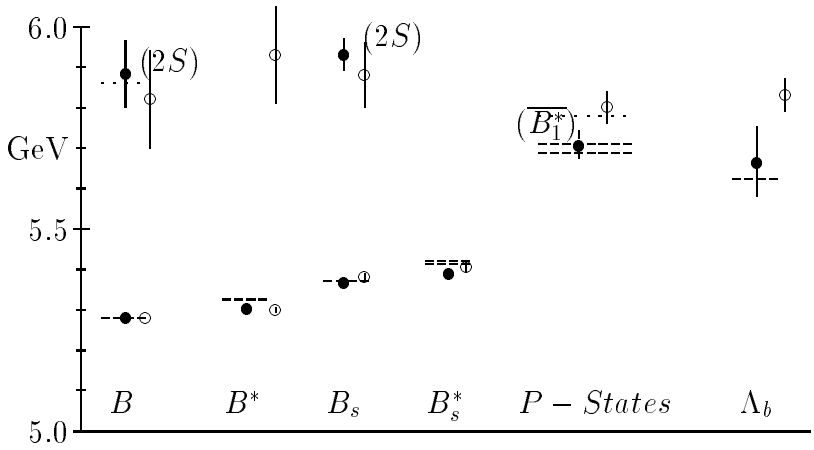

Figure 2.2: *The lower lying* B *and* Λ_{b} *mass spectrum. The open circles denote results obtained from a lattice QCD calculation [20]. The dashed lines denote the upper and lower bounds on the experimental results. The dotted lines indicate unconfirmed experimental results. For the* $L = 1$ *states the dashed and dotted lines represent different* B_J^* *states. The errors shown are purely statistical. The filled circles represent preliminary results from a quenched simulation at* $\beta^{n_f=0} =$ 6.0 *[21]. The figure is taken from [20].*

2.4.2 The Operator Product Expansion (OPE)

An important theoretical tool in heavy quark physics is the Wilson **O**perator **P**roduct **E**xpansion (OPE) [22]. The idea of the OPE, formulated in the late 60's by K. Wilson, is based on the concept of separating effects originating at large and small distances in a given physics process. The QCD Lagrangian is formulated at very high energy scales with some normalization point μ_0 well above all other mass scales appearing in the theory. An effective theory to be used in the low energy regime is obtained by evolving the Lagrangian from the high scale μ_0 down to low energies $\mu \ll m_W$ or $\mu \ll m_\mathrm{b}$. In this procedure all high momentum contributions are step by step integrated out and in the end an effective Lagrangian $\mathcal{L}(\mu)$ is obtained. A well known example of integrating out high-momentum contributions

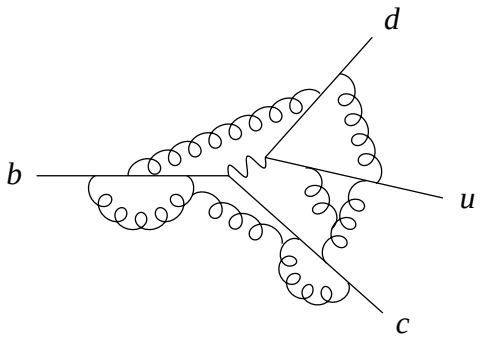

Figure 2.3: *Non-leptonic decay of a b quark.*

is the low-energy four-fermion weak decay Lagrangian. To give a concrete example, let us consider a non-leptonic decay of a b quark, $\mathrm{b} \to \mathrm{c\bar{u}d}$, mediated by a virtual W boson (see Figure 2.3) [15]. The momenta of the virtual gluons and gauge bosons can be classified according to the energy scales involved such as $\mu \gg m_W$ or $\mu \simeq \Lambda_\mathrm{QCD}$, corresponding to different distance scales. Examining the decay with a high resolution $\Delta x < 1/m_W$ we find

$$\bar{\mathrm{c}}\gamma^\mu(1-\gamma^5)\mathrm{b}\bar{\mathrm{d}}\gamma_\mu(1-\gamma^5)\mathrm{u} \cdot \frac{(\mathrm{i}g_\mathrm{w})^2/4}{p^2 - {m_W}^2} \tag{2.29}$$

where the highly virtual W boson travels a distance of $\simeq 1/m_W$. Viewed with a lower resolution $\Delta x > 1/m_W$, the decay appears to be a local interaction at the point where the four quarks coincide. To understand this, we make a Taylor expansion of the propagator in powers of p^2/m_W^2:

$$\bar{\mathrm{c}}\gamma^\mu(1-\gamma^5)\mathrm{b}\bar{\mathrm{d}}\gamma_\mu(1-\gamma^5)\mathrm{u} \cdot \frac{g_\mathrm{w}^2}{8{m_W}^2}\left(1 + \frac{p^2}{m_W^2} + \frac{p^4}{m_W^4} + \ldots\right) , \tag{2.30}$$

where the coefficient before the Taylor expansion is simply $G_\mathrm{F}/\sqrt{2}$. The momentum dependent propagator of Equation 2.29 describing the propagation of the W

boson between two points in space-time thus corresponds to a matrix element of the following sum of *local* operators:

$$\frac{\mathrm{G_F}}{\sqrt{2}}\bar{\mathrm{c}}\gamma^\mu(1-\gamma^5)\mathrm{b}\left(1+\frac{i\partial^2}{m_W^2}+\frac{i\partial^4}{m_W^4}+\ldots\right)\bar{d}\gamma_\mu(1-\gamma^5)u\ . \tag{2.31}$$

This expansion with the derivatives acting on the current on the right is valid for $p^2 \ll m_W^2$. A field theory constructed for this low energy region with the high mass W integrated out is called an *effective* theory. It is non-renormalizable and therefore only defined up to a certain cutoff, in this specific case up to $\mu = m_W$. As long as $p^2 \ll m_w^2$, the theory is well defined.

In heavy quark physics, the peculiarity of the theory lies in the fact that the in- and out-going states contain heavy quarks Q. Although we can integrate out contributions down to $\mu < m_Q$, the heavy quark field itself should not be eliminated completely since it is present in the initial state. How this problem is solved using the Heavy Quark Expansion is explained in the next section.

2.4.3 Heavy Quark Effective Theory (HQET)

Fist of all, an illustration of the meaning of "heavy" is given. In the Standard Model there are six quarks with different masses. The masses of u and d are only a few MeV/c^2 and therefore much smaller than Λ_{QCD}. The s quark mass is about 150 MeV/c^2 and therefore already in the Λ_{QCD} range of several hundred MeV/c^2. Quarks with $m_Q \gg \Lambda_{\mathrm{QCD}}$ are called heavy. The top quark, $m_{\mathrm{t}} \simeq 175$ GeV/c^2, decays too fast to allow the formation of bound states since the width of the decay $\mathrm{t} \to \mathrm{b}W^+$ is $,_{\mathrm{t}} \simeq 1$ GeV/c^2. The charm quark has a mass which is sometimes too low for a reasonable approximation in powers of $1/m_{\mathrm{c}}$. Therefore, each case involving charmed hadrons has to be studied before an answer can be given. The bottom quark is heavy enough to confidently use the $1/m_{\mathrm{b}}$ expansion but still light enough to allow bound states. In summary, a quark Q is called heavy if $m_Q \gg \Lambda_{\mathrm{QCD}}$, or even better $m_Q > m_{\mathrm{c}}$. The bottom quark is obviously the perfect candidate to apply the $1/m_{\mathrm{b}}$ expansion.

According to the previous paragraph, the mass scale μ to separate short- and long-distance effects is given by $\Lambda_{\mathrm{QCD}} \ll \mu \ll m_{\mathrm{b}}$. A heavy quark bound into a hadron with light degrees of freedom of energies $\simeq \Lambda_{\mathrm{QCD}}$ is subject to fluctuations around its mass shell. The virtualities involved are of the order Λ_{QCD} and instead of removing the heavy particle completely from the effective theory only the small fluctuations are integrated out. The situation is displayed in Figure 2.4: whereas at high energies the physics is treated perturbatively, non-perturbative methods have to be employed at low energies to describe the rather complicated physics in the confinement region. The idea of Heavy Quark Effective Theory [15, 23] is to find a simplified description in the non-perturbative region by integrating out the high-momentum components. In the limit of high energies, this effective theory has to be identical to QCD. After the separation of the short-distance physics, some new, approximate symmetries may be realized in a particular kinematic

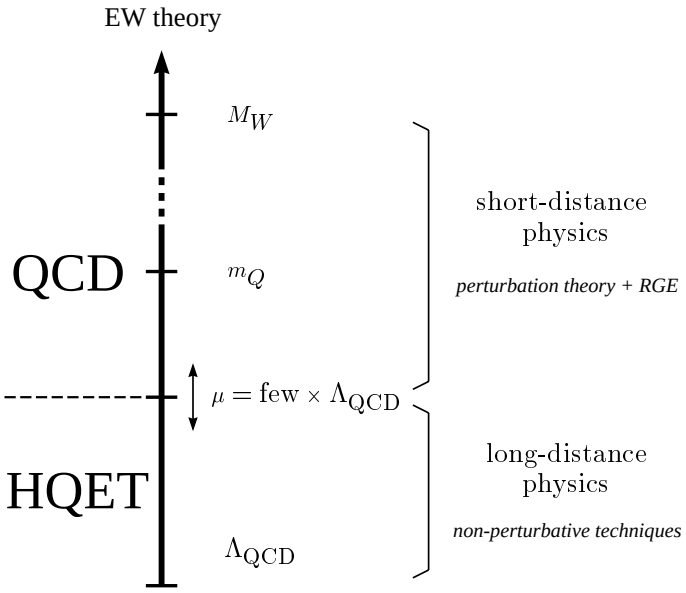

Figure 2.4: *Energy scales in QCD and definition of the HQET regime. The Figure is taken from [23].*

situation leading to welcome simplifications. Thus an effective Lagrangian has to be constructed that is explicitly invariant under the new symmetries and a systematic expansion in powers of $1/m_Q$ is performed.

The physics of a meson containing one heavy quark is similar to that of the Hydrogen atom. While the change in momentum of the heavy quark is of order Λ_{QCD}, its change in velocity, $\Lambda_{\text{QCD}}/m_Q \ll 1$, is negligible in the limit $m_Q \to \infty$. In this limit, the heavy quark appears to be at rest, acting as a static colour source and therefore the binding and in consequence the mass spectrum of excited states becomes flavour independent. Furthermore, the heavy quark carries spin $S_Q = \frac{1}{2}$, resulting in a magnetic moment $\mu_Q \propto \text{g}/2m_Q$. In the heavy quark limit we have $\mu_Q \to 0$ and thus the light degrees of freedom are also independent of $S_Q = \frac{1}{2}$ leading to degenerate pairs of states according to $S_{Q,z} = +\frac{1}{2}$ and $S_{Q,z} = -\frac{1}{2}$. When effects of order $1/m_Q$ are included, the chromo-magnetic interaction cause a hyperfine splitting of the states. This leads in the theory e.g. to relations such as [24]

$$m^2_{\text{B}^*} - M^2_{\text{B}} = m^2_{\text{D}^*} - M^2_{\text{D}} \,, \tag{2.32}$$

which is accurate up to $\Lambda^3_{\text{QCD}}(1/m_{\text{c}} - 1/m_{\text{b}}) \simeq 0.1\ \text{GeV}^2$ and in agreement with experiment. In this case, the heavy quark limit holds for charm quarks as well. Obviously, the light degrees of freedom are the same when combined with any of the four heavy quark states $\text{b}(+\frac{1}{2})$ $\text{b}(-\frac{1}{2})$ $\text{c}(+\frac{1}{2})$ $\text{c}(-\frac{1}{2})$ and thus an SU(4) symmetry holds in lowest order $(1/m_Q)^0$.

How can we take the limit $m_Q \to \infty$ of the QCD Lagrangian? Rewriting the mass dependent part of Equation 2.8 for one heavy quark Q with some obvious simplifications in notation, we obtain

$$\mathcal{L}_Q = \bar{\psi}(i\gamma^\mu D_\mu - m_Q)\psi \; . \tag{2.33}$$

Making use of the fact that the heavy hadron defines a rest frame where the (unchanged) hadron four-velocity is $v^\mu = (1, \mathbf{0})$ allows a re-definition of the quark field:

$$\psi \to e^{-im_Q x^0} \begin{pmatrix} h \\ H \end{pmatrix} , \tag{2.34}$$

where h is the two-component part of light degrees of freedom and H is the two-component part of heavy degrees of freedom. Inserting the field 2.34 in the heavy quark Lagrangian 2.33 gives

$$\mathcal{L}_Q = \bar{h} i D^0 h + \bar{H}(-iD^0 - 2m_Q)H - \bar{h} i\boldsymbol{\gamma}\boldsymbol{D} H - \bar{H} i\boldsymbol{\gamma}\boldsymbol{D} h \; , \tag{2.35}$$

where h looks like a massless field and H like a field with mass $2m_Q$. Using the equations of motion $\delta\mathcal{L}_Q/\delta\bar{H} = 0$ and the fact that the heavy quark components are small: $H \simeq \frac{\Lambda_{\mathrm{QCD}}}{m_Q} h$, the heavy degrees of freedom H are eliminated from the Lagrangian. The final result is

$$\mathcal{L}_{\mathrm{HQET}} = \bar{h} i D^0 h - \frac{1}{2m_Q}\left(\bar{h}(i\boldsymbol{D})^2 h + \mathrm{g}\bar{h}\boldsymbol{\sigma}\mathbf{B}h\right) + \mathcal{O}(1/m_Q^2) \; , \tag{2.36}$$

where $\mathbf{B}$ is the chromo-magnetic field of the heavy quark and $\boldsymbol{\sigma}$ are the three Pauli matrices. The first term of the effective Lagrangian is invariant under SU(4), as already stated earlier.

2.4.4 Quark models

A variety of models exist to describe bound states made up of quarks and gluons and many of these are invented for a very limited purpose, to describe some particular feature of hadron phenomenology such as spectroscopy, fragmentation or weak decays. Nevertheless, there are some basic theoretical constraints which must be fulfilled by any reasonable model. This is because the models have to be consistent with QCD. Typical constraints for such models are the compatibility with symmetries such as Heavy Quark Symmetry and unitarity bounds. In the following two quark models are described in some detail: the Potential Model and the Relativistic Quark Model. The first is chosen because it is very simple and already gives insight in the standard spectroscopic notations used for excited meson states. The second is described because it produces quite useful results for the mass spectrum of orbitally and radially excited B (and D) meson states.

The Potential Model

The Potential Model [16] is based on the assumption that hadrons are composed of constituents which move non-relativistically within a confining potential. The quantum mechanical treatment can be directly compared with e.g. the calculation of the hydrogen atom. It is assumed that QCD interactions dress each quark with a cloud of virtual gluons and quark-antiquark pairs. The constituent quark mass is therefore a different concept and constituent quark masses are larger than the bare quark masses used in the Lagrangian 2.8. The Potential Model provides a simple framework based on the Schrödinger equation to describe both ground and excited hadronic states. The mass of a hadron α is given by

$$M_\alpha = \sum_i M_i + E_\alpha \ , \tag{2.37}$$

where the sum is over all constituent quarks in the hadron and the energy E_α is an eigenvalue of the Schrödinger equation

$$\mathrm{H}\psi_\alpha = E_\alpha \psi_\alpha \tag{2.38}$$

with the Hamiltonian

$$\mathrm{H} = \sum_i \frac{1}{2M_i}\mathbf{p}_i^2 + \sum_{i<j} \mathrm{V}(\mathbf{r}_{ij}) \tag{2.39}$$

and $\mathbf{r}_{ij} = \mathbf{r}_i - \mathbf{r}_j$. The inter-quark potential V is usually chosen to have the properties of a spin and flavour independent long range confining potential and a spin and flavour dependent short range potential. Relativistic corrections can be implemented to derive a more realistic behaviour. In the case of mesons ($\mathrm{q\bar{q}}$) the centre-of-mass dependence of the Schrödinger equation is removed by introducing the reduced two-body mass $m = \frac{m_\mathrm{q} m_\mathrm{\bar{q}}}{m_\mathrm{q}+m_\mathrm{\bar{q}}}$ and $\mathbf{r} = \mathbf{r}_\mathrm{q} - \mathbf{r}_\mathrm{\bar{q}}$:

$$\left(\frac{\mathbf{p}^2}{2m} + \mathrm{V}(\mathbf{r})\right)\psi_\alpha(\mathbf{r}) = E_\alpha \psi_\alpha(\mathbf{r}) \ . \tag{2.40}$$

With the total spin $\boldsymbol{S} = \boldsymbol{S}_\mathrm{q} + \boldsymbol{S}_\mathrm{\bar{q}}$ and the angular momentum $\boldsymbol{L}$ the total angular momentum $\boldsymbol{J} = \boldsymbol{S} + \boldsymbol{L}$ is formed using the LS coupling scheme. The infinite number of eigenstates of the two-quark system is defined by the radial quantum number n and the angular momentum quantum numbers J, J_z, L, S. The standard spectroscopic notation of meson states is given by ${}^{2S+1}L_J(J^{PC})$ which the following definitions for parity P and charge conjugation C:

$$P = (-1)^{L+1} \qquad\qquad C = (-1)^{L+S} \ . \tag{2.41}$$

Although C can be only defined for electrically neutral eigenstates, it is often introduced for a whole multiplet like (π^+, π^0, π^-). For orbitally-excited states $L = 1$ for example we obtain a singlet ${}^1P_1(1^{+-})$ and a triplet ${}^3P_{0,1,2}(0^{++}, 1^{++}, 2^{++})$. In spectroscopy, the series $J^P = 0^+, 1^-, 2^+, \ldots$ is called *natural* and the alternate

series $J^P = 0^-, 1^+, 2^-, \ldots$ is called *unnatural*. The meson states belonging to the natural series have a superscript "$*$" added, e.g. B^*. There is also a number of J^{PC} configurations which cannot be accommodated with $q\bar{q}$, e.g. 0^{--}. Therefore, such states are called *exotic*.

With a hadron radius of the order of $R \simeq 1$ fm we deal with quark energies in the range of a few hundred MeV. Thus the nonrelativistic treatment can be questioned. In fact even for heavy quark states the model does not provide a very good approximation. A more adequate model to cope with this problem is the so called Relativistic Quark Model.

The Relativistic Quark Model

The Relativistic Quark Model [25] is based on the quasi-potential approach in quantum mechanics and is in this Section applied to meson states containing one heavy and one light quark (Qq). Instead of employing an expansion in inverse powers of the light quark mass, the light quark is treated fully relativistically. For the heavy quark, the $1/m_Q$ expansion is applied up two the first order. The bound states of heavy-light mesons are the solution of the following quasi-potential equation:

$$\left(\frac{b^2(M)}{2\mu_R} - \frac{\mathbf{p}^2}{2\mu_R}\right)\Psi_M(\mathbf{p}) = \int \frac{d^3q}{(2\pi)^3} V(\mathbf{p},\mathbf{q};M)\Psi_M(\mathbf{q}) \,, \tag{2.42}$$

where the relativistic reduced mass is

$$\mu_R = \frac{E_q E_Q}{E_q + E_Q} = \frac{M^4 - (m_q^2 - m_Q^2)^2}{4M^3} \,, \tag{2.43}$$

and E_q, E_Q are given by

$$E_q = \frac{M^2 - m_Q^2 + m_q^2}{2M}, \quad E_Q = \frac{M^2 - m_q^2 + m_Q^2}{2M} \,. \tag{2.44}$$

$M = E_q + E_Q$ is the meson mass, $m_{q,Q}$ are the masses of light and heavy quarks, and $\mathbf{p}$ is their relative momentum. In the centre-of-mass system the relative momentum squared is given by

$$b^2(M) = \frac{[M^2 - (m_q + m_Q)^2][M^2 - (m_q - m_Q)^2]}{4M^2}. \tag{2.45}$$

The quasi-potential of the quark-antiquark interaction, $V(\mathbf{p},\mathbf{q};M)$, is the sum of a one-gluon exchange term, a long-range vector and a linear scalar confining potential and defined by:

$$V(\mathbf{p},\mathbf{q};M) \quad = \quad \bar{u}_q(p)\bar{u}_Q(-p)\left\{\frac{4}{3}\alpha_s G_{\mu\nu}(\mathbf{k})\gamma_q^\mu\gamma_Q^\nu\right.$$

$$+V^V_{\rm conf}(\mathbf{k}),\, {}^{\mu}_{q},\, {}_{Q;\mu} + V^S_{\rm conf}(\mathbf{k}) \Big\} u_q(q) u_Q(-q), \qquad (2.46)$$

where $\alpha_{\rm s}$ is the QCD coupling constant, $G_{\mu\nu}$ is the gluon propagator and $\mathbf{k} = \mathbf{p} - \mathbf{q}$. γ_μ and $u(p)$ are the Dirac matrices and spinors. The vector and scalar confining potentials in the nonrelativistic limit reduce to

$$\begin{aligned} V^V_{\rm conf}(r) &= (1-\varepsilon)(Ar+B) \\ V^S_{\rm conf}(r) &= \varepsilon(Ar+B) \\ V^S_{\rm conf}(r) + V^V_{\rm conf}(r) &= Ar + B\,, \end{aligned} \qquad (2.47)$$

where ε is the mixing coefficient of the two potential types. In the heavy quark

State $n^j L_J$	RQM $m_Q \to \infty$	RQM $1/m_Q$	experiment
$1\frac{1}{2}S_0$	5.394	5.285	5.2792 ± 0.0018 [26]
$1\frac{1}{2}S_1$		5.324	5.3249 ± 0.0018 [26]
$1\frac{1}{2}P_0$	5.778	5.738	5.698 ± 0.012 [26]
$1\frac{1}{2}P_1$		5.757	
$1\frac{3}{2}P_1$	5.680	5.719	5.698 ± 0.012 [26]
$1\frac{3}{2}P_2$		5.733	
$2\frac{1}{2}S_0$	5.835	5.883	$\simeq 5.90$? [27]
$2\frac{1}{2}S_1$		5.898	$\simeq 5.94$? [28]

Table 2.2: *Mass spectrum of* B *mesons predicted by the Relativistic Quark Model in comparison with experimental data. n denotes the radial quantum number and* $j_q = S_q + L$ *is the angular momentum of the light degrees of freedom. The notation used here is different from the* $^{2S+1}L_J$ *notation because in the heavy quark limit the spin and the orbital momentum of the light degrees of freedom are combined first, whereas in the standard spectroscopic notation first the spins of the quarks are added up and then combined with the orbital momentum (LS coupling). The experimental results presented for the radial excitations should be taken with great care as they have not been confirmed by other experiments so far.*

limit $m_Q \to \infty$

$$\left(\frac{E_q^2 - m_q^2}{2E_q} - \frac{\mathbf{p}^2}{2E_q} \right) \Psi_M(r) = V_{m_Q \to \infty}(r) \Psi_M(r)\,, \qquad (2.48)$$

where the mass of the meson is given by $M = m_Q + E_q$. Equation 2.48 can be compared with the non-relativistic equation 2.40. Equation 2.48 can be solved numerically and eigenvalues E_q and wave functions ψ_M are obtained as well as

heavy-light meson mass spectra. In table 2.2 the masses derived from Equation 2.48 for B mesons are listed. To further improve the calculation, the $1/m_Q$ correction is included. This results in a correction term $\delta V_{1/m_Q}(r)$ to be added to $V_{m_Q\to\infty}(r)$. The calculated masses including first order $1/m_Q$ corrections are shown in table 2.2 and compared with experimental data, if available. The model seems to describe the experimental data quite well although it is hard to estimate the uncertainties of the calculation. The $1/m_Q$ correction clearly improves the calculated mass spectrum and causes a so called spin-orbit inversion of $L = 1$ states, i.e. the $j_q = 1/2$ states lie above the $j_q = 3/2$ states.

2.5 Production and decay of b hadrons

In e^+e^- interactions at centre-of-mass energies $\sqrt{s} \simeq M_{Z^0}$, the ingoing leptons annihilate to a Z^0/γ^* resonance which decays into a fermion-antifermion pair. The exchange of a virtual photon instead of a Z^0 is largely suppressed and thus b hadrons are predominantly produced in the decay $Z^0 \to b\bar{b}$. The fragmentation process which transforms an initial set of partons such as $q\bar{q}$ into a final set of hadrons is theoretically not well understood. Therefore, phenomenological models are used to describe this transition.

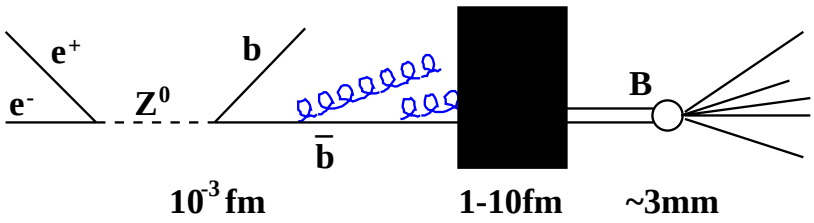

Figure 2.5: *Time scales in the formation of b hadrons. 1. Electro-weak phase up to* 10^{-3} *fm. 2. Perturbative QCD phase. 3. The non-perturbative phase is indicated by a black box. 4. The phase of the decay of the hadron.*

In the evolution of the process $e^+e^- \to Z^0 \to b\bar{b}$, several different time steps can be distinguished as indicated in Figure 2.5. The first is the electro-weak phase and includes production and decay of the Z^0. This phase is completed after a time of order $m_{Z^0}^{-1} \simeq 10^{-3}$ fm and is calculable with high accuracy using electro-weak perturbation theory. The second phase is the perturbative QCD phase including gluon radiation. As α_s becomes large for soft gluon emission, the accuracy is not as good as for electro-weak expansions. In the third phase colourless hadrons such as b-flavoured mesons are produced from coloured partons after a time of about $\gamma\Lambda_{QCD} \simeq 10$ fm where the distance is calculated in the lab frame. The forth phase is the decay of unstable hadrons into observable final state particles, e.g. the weak decay of b hadron ground states. Assuming a lifetime of about 1 ps, the b hadrons travel a distance of up to a few mm in the lab frame before they decay.

Electro-weak phase

The Z^0 boson couples to quarks through vector and axial-vector charges with the strength

$$\sqrt{\frac{G_F m_Z^2}{2\sqrt{2}}}\gamma_\mu(v_q - a_q\gamma^5)\,, \tag{2.49}$$

where the vector and axial vector couplings are defined as

$$\begin{aligned} v_q &= 2I_q^3 - 4e_q \sin^2\theta_W \\ a_q &= 2I_q^3 \end{aligned} \tag{2.50}$$

$$\tag{2.51}$$

with $2I_q^3 = \pm 1$ for up/down type quarks and θ_W is the weak mixing angle. The Born approximation provides already a quite accurate determination of the partial decay width

$$,\,(Z^0 \to b\overline{b}) = \frac{G_F m_Z^3}{8\sqrt{2}\pi}\beta\left(\frac{3-\beta^2}{2}v_b^2 + \beta^2 a_b^2\right) \tag{2.52}$$

with the b quark velocity $\beta = \sqrt{1 - 4m_b^2/s}$. The leading electro-weak corrections are due to initial and final state radiation and loops with bottom and top quarks and can be absorbed in shifts of the Fermi coupling and the mixing angle:

$$\begin{aligned} G_F &\to G_F(1+\Delta\rho)\,; \\ \sin^2\theta_W &\to \sin^2\theta_W(1+\Delta\kappa_{\rm SE})\,. \end{aligned} \tag{2.53}$$

Next to the electro-weak corrections, QCD corrections have to be considered.

Perturbative QCD phase

QCD corrections to the width $,\,(Z^0 \to b\overline{b})$ have been calculated up to second order for vector and axial-vector contributions for arbitrary quark masses. A quantity of high interest is the ratio $,\,(Z^0 \to b\overline{b})/,\,(Z^0 \to \text{hadrons})$. Most of the QCD corrections cancel in this ratio and in the end one finds [29]

$$\left.\frac{,\,(Z^0 \to b\overline{b})}{\sum_q ,\,(Z^0 \to q\overline{q})}\right|_{m_b=0} \cdot \left(1 - 0.0031 - 0.005\left(\frac{\alpha_s}{\pi}\right) - 2.3\left(\frac{\alpha_s}{\pi}\right)^2 - 6.9\left(\frac{\alpha_s}{\pi}\right)^3\right)\,. \tag{2.54}$$

Typical values for the correction factor at $q^2 \approx M^2(Z^0)$, depending on the values used for α_s and m_b, are around $(1 - 7\cdot 10^{-4})$ [11].

For the simulation of this phase, two different models are used. First, QCD shower models are based on calculations which derive probabilities for the process $q \to qg$, $g \to gg$ $g \to qq$ by summing leading and next-to-leading logarithms of

[11] Note that the correction factor in Equation 2.54 holds for $m_b = 0$ and becomes smaller for larger m_b.

the perturbative expansion to all orders. Thus several quarks and gluons can be produced per event at centre-of-mass energies $\sqrt{s} \simeq M_{Z^0}$. Second, fixed order QCD models are based on the complete calculation of QCD matrix elements for $q\bar{q}$, $q\bar{q}g$, $q\bar{q}gg$ and $q\bar{q}q\bar{q}$. So far the highest order calculations available are of $\mathcal{O}({\alpha_s}^2)$.

Fragmentation phase

To describe the transition of quarks and gluons into hadrons, no rigourous calculations are available and only phenomenological models exist. A realistic description of the fragmentation stage is presently feasible only within the context of stochastic, non-perturbative models. The models can be classified in three different categories: independent fragmentation, string and cluster models.

Independent fragmentation describes the hadronization of each individual parton in isolation within a sequence of iterative $q \rightarrow q' +$ hadron branchings. The sharing of energy and momentum at each branching is given by a probability distribution $f(z)$ with $z = \frac{(E+p_z)_{\mathrm{hadron}}}{(E+p_z)_{\mathrm{q}}}$. The process is stopped when a certain energy bound is violated, depending on the specific model.

The widely used *string model* is based on the idea that when oppositely coloured quarks move apart, the colour field between them makes up a narrow flux tube which is called a string. The traverse dimension of such a string is of the order of 1 fm. As the quarks move apart, the potential energy of the string increases linearly and finally the string brakes by creation of a new $q\bar{q}$ pair. As long as the invariant mass of produced strings is large enough, further breaks into $q\bar{q}$ pairs may occur. As the different string breaks are thought of disconnected events, an independent fragmentation function $f(z)$ to describe the energy and momentum distribution is used. Typical examples of fragmentation functions that fit experimental data are the Lund symmetric function for light flavours [30]

$$f(z) \propto \frac{(1-z)^a}{z} e^{-bm_\perp^2/z} \,, \tag{2.55}$$

where $m_\perp^2 = m_q^2 + p_\perp^2$ is the transverse quark mass squared, and the Peterson function [31]

$$f(z) \propto \left(z \left(1 - \frac{1}{z} - \frac{\epsilon_Q}{1-z} \right)^2 \right)^{-1} \,, \tag{2.56}$$

where ϵ_Q is free parameter relating different quark masses: $m_{Q_1}^2 \epsilon_{Q_1} = m_{Q_2}^2 \epsilon_{Q_2}$. The Peterson function describes well experimental data for heavy flavours charm and bottom.

The concept of *cluster fragmentation* gives a rather simple description of hadronization. In the cluster model, clusters are assumed to be the basic units leading to the production of hadrons. Clusters may be characterised by their mass and flavour content and are produced in a process similar to string fragmentation

but creating a cluster instead of a $q\bar{q}$ pair by a break of the string. In some cluster fragmentation models the concept of the string is replaced by forced $g \to q\bar{q}$ branchings. If most of the produced clusters happen to have masses around several GeV, the cluster mass spectrum may be interpreted as a superposition of broad resonances.

Final state hadron decay phase

The last step in the whole generation procedure is the phase of hadronic final states and the subsequent decay of unstable hadrons. In Monte Carlo programs, this phase is usually simulated by implementing available decay tables e.g. taken from the Particle Data Book [26]. Also the production rate of specific hadrons can be tuned to some extend, depending on the fragmentation scheme used. This work makes several contributions to improve our experimental knowledge on production rates and decays of excited B mesons.

2.6 Properties of excited B mesons

In this section, we further exploit the symmetries of heavy-light mesons described in Section 2.4.3. We already mentioned an important prediction of Heavy Quark Effective Theory: the existence of an approximate spin-flavour symmetry for hadrons containing one heavy quark Q ($m_Q \gg \Lambda_{\rm QCD}$) [32, 33, 34, 35, 36, 37, 38, 39, 40, 41, 42]. In the limit $m_Q \to \infty$, mesons composed of a heavy quark Q and a light quark q are characterised by the spin of the heavy quark S_Q, the total angular momentum of the light quark $j_q = S_q + L$ and the total angular momentum J, where S_q and L denote the spin and the orbital angular momentum respectively of the light quark. In the heavy quark limit, both S_Q and j_q are good quantum numbers and the total angular momentum of the meson is given by $J = S_Q + j_q$. For $L = 0$ we obtain $J = S_Q \pm \frac{1}{2}$ corresponding to the pseudo-scalar meson B

state	J_j^P	predicted B_J^* properties		
		mass [GeV/c^2]	width [GeV/c^2]	decay mode
B_0^*	$0^+_{1/2}$	5.738	0.20-1.00	$(B\pi)_{S-wave}$
B_1	$1^+_{1/2}$	5.757	0.25-1.30	$(B^*\pi)_{S-wave}$
B_1	$1^+_{3/2}$	5.719	0.021	$(B^*\pi)_{D-wave}$
B_2^*	$2^+_{3/2}$	5.733	0.025	$(B^*\pi)_{D-wave}$, $(B\pi)_{D-wave}$

Table 2.3: *Masses, widths and dominant decay modes based on theoretical predictions [43, 44, 25, 45, 46, 47, 48, 49, 50, 51, 52]. Recent calculations using a bag model predict widths of* , $(B_0^*) = 0.141$ GeV/c^2 *and* , $(B_1(1/2)) = 0.139$ GeV/c^2 *for the broad states [53].*

($J^P = 0^-$) and the vector meson B^* ($J^P = 1^-$). For $L = 1$, there are four states with spin-parity $J^P = 0^+$, 1^+, 1^+ and 2^+. If the heavy quark Q is a bottom quark, these states are labelled B_0^*, B_1 for both 1^+ states[12] and B_2^* [26], respectively. The four states, commonly called B_J^*, or alternatively B^{**} [13], are grouped into two sets of degenerate doublets, corresponding to $j_q = 1/2$ and $j_q = 3/2$ as indicated in Table 2.2 and Table 2.3. Parity and angular momentum conservation put restrictions on the strong decays of these states to $B^{(*)}\pi$ [14] (see Figure 2.6). The 0^+ state can only decay to $B\pi$ via an S-wave transition, both 1^+ states can

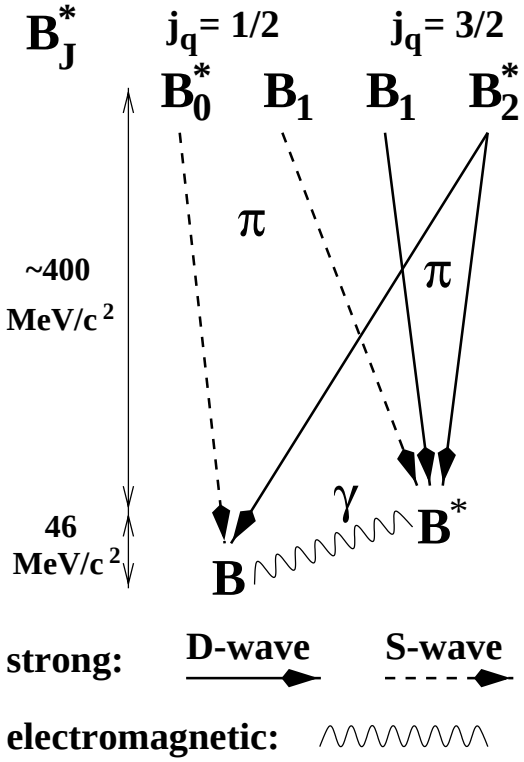

Figure 2.6: *The four* B_J^* *states and their dominant decays to the ground state doublet* (B, B^*). *Strong decays via single pion emission are indicated as solid (D-wave) and dashed (S-wave) lines. The* B^* *decays radiatively because of the small* B^*–B *mass splitting of* 46 MeV/c^2.

decay to $B^*\pi$ via either S-wave or D-wave transitions, and the 2^+ state can decay

[12] In the case of mixing of the $J = 1$ states, the notation $B_1(H)$ and $B_1(L)$ is used to distinguish the physical states.

[13] Throughout this thesis, I use the Particle Data Group notation B_J^* for orbitally-excited B mesons.

[14] Throughout this thesis, $B^{(*)}\pi$ denotes the final states $B\pi$ *and* $B^*\pi$. The notations $B^{(*)}\pi\pi$ and $B^*\pi(\pi)$ are to be interpreted in the same way.

to both $B\pi$ and $B^*\pi$ only via D-wave transition. States decaying via an S-wave transition are expected to be much broader than the states decaying via a D-wave transition [45].

In addition to the decays via a single pion also decays to $B^*\pi\pi$ and $B\pi\pi$ exist. The restrictions for single pion transitions to the ground states B and B^* do not hold for $B^*_J \to B^{(*)}\pi\pi$ decays. Although these decays are phase space suppressed, intermediate states with large width like $B^*_J \to B^{(*)}\rho \to B^{(*)}\pi\pi$ may cause a significant enhancement of the $B^*\pi\pi$ and $B\pi\pi$ final states [43, 44].

Excitations with radial quantum number $n = 2, 3, \ldots$ are expected to show the same mass spectrum properties at higher mass scale. B mesons with $n > 1$ are predicted to be suppressed with respect to the $n = 1$ ground states.

B meson states containing a bottom and a strange quark show a behaviour similar to $B_{u,d}$ states. E.g. the $B^* - B$ mass splitting is approximately the same for states with and without strangeness. Orbitally-excited strange B mesons, B^*_{sJ}, are not allowed to decay to $B^*_s\pi$ because of isospin conservation. Therefore, the strangeness is always carried by a kaon in the decay $B^*_{sJ} \to B^{(*)}K$. This leads to a substantial suppression of the B_s ground state in Z^0 in decays in comparison with $B_{u,d}$ as observed at LEP.

The expected mass spectrum for B_c states should be qualitatively similar to the other B meson spectra, although differences in the size of mass splittings are expected, since the heavy quark limit is not a good approximation anymore. For the B_c, relativistic corrections are expected to be smaller.

2.7 The experimental status of B meson spectroscopy

An overview of B meson states observed and identified by experiment is shown in Figure 2.7. All pseudo-scalar ground states are well established. Their lifetimes and masses as well as major decay modes have been measured accurately [26]. The b hadron sample composition in $Z^0 \to b\overline{b}$ decays, masses and lifetimes are presented in Table 2.4.

Also the vector ground states except the B^*_c have been observed by e^+e^- experiments operating at $\sqrt{s} = M(\Upsilon(4S))$ or $\sqrt{s} = M(Z^0)$. Due to the small mass splitting of the ground state doublet, the vector meson decays radiatively. A separation of the B^*_s from $B^*_{u,d}$ is a challenging experimental task and therefore most B^* results average over strange and non-strange mesons. Figure 2.8 shows measurements of the $B^* - B$ mass splitting and the B^* production rate in Z^0 decays with respect to the production of B mesons. The observed production rate is consistent with a simple spin counting picture: $\frac{\sigma_{B^*}}{\sigma_{B^*}+\sigma_B} = 0.75 \pm 0.04$. Since the measured B^* production rate is the production rate of the final state but not the primary production rate, the situation is in fact more complicated. The measured B^* production rate may be altered by feed-down from B^*_J and B^*_{sJ} decays. Under the assumption that only B^*_J states contribute significantly, we obtain for the

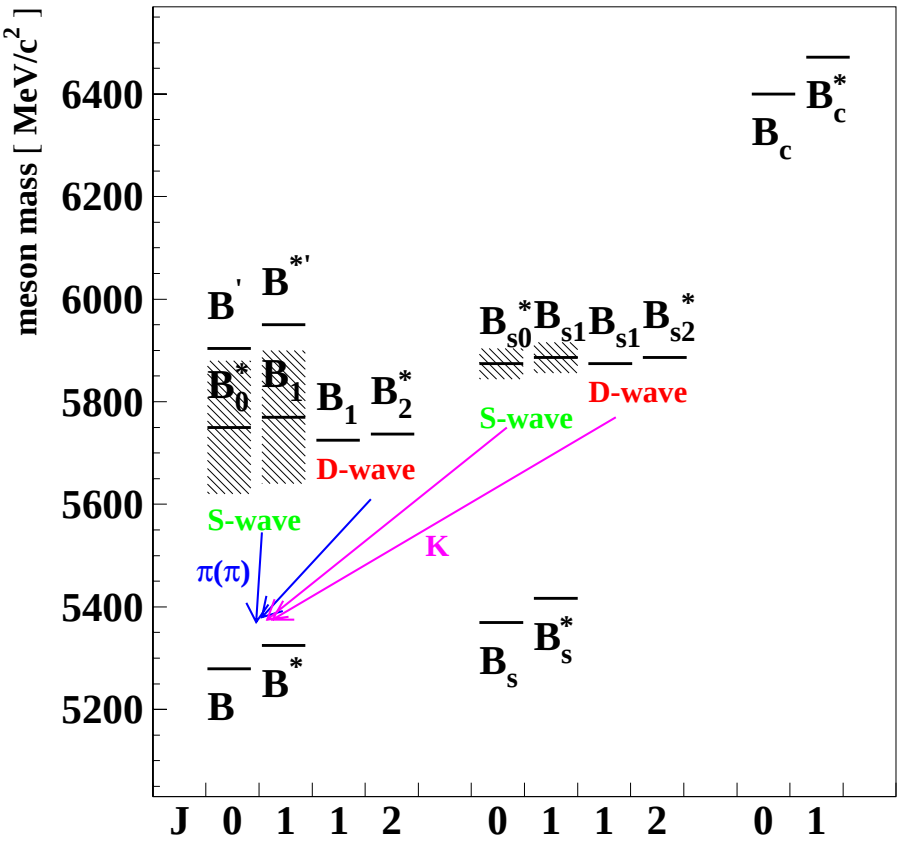

Figure 2.7: *Spectrum of* B *mesons. Only the* B_c^* *has not yet been observed. The status of the* $B^{(*)\prime}$ *is unclear. The* B_J^* *and* B_{sJ}^* *multiplets have been observed but no individual states have been isolated so far. The* B *ground states are well established.*

b hadron	fraction [%]	mass [MeV/c^2]	lifetime [ps]
B^-	$39.7^{+1.8}_{-2.2}$	5278.9 ± 1.8	1.65 ± 0.03
$\bar{B}^0$	$39.7^{+1.8}_{-2.2}$	5279.2 ± 1.8	1.54 ± 0.03
$\bar{B}_s$	$10.5^{+1.8}_{-1.7}$	5369.3 ± 2.0	1.54 ± 0.07
$\bar{B}_c$	$\simeq 0$	6400 ± 400	0.46 ± 0.18
Λ_b	$10.1^{+3.9}_{-3.1}$	5624 ± 9	1.24 ± 0.08

Table 2.4: *Admixture, masses and lifetimes of weakly decaying* b *hadron species in* $Z^0 \to b\bar{b}$. *For the production fractions in* $Z^0 \to b\bar{b}$, $f_{B^0} = f_{B^+}$ *and* $f_{B^0} + f_{B^+} + f_{B_s} + f_{\Lambda_b} = 1$ *is assumed.* Λ_b *denotes all* b *baryon species for the production fractions whereas the numbers for mass and lifetime refer to the* Λ_b *baryon only. The numbers are taken from the 1999 update of [26].*

primary B^* production ratio[15]

$$\frac{V}{V+P} = \frac{1}{1-f_{B_J^*}} \left(\frac{\sigma_{B^*}}{\sigma_{B^*}+\sigma_B} - f_{B_J^*} \cdot \mathrm{BR}(B_J^* \to B^*\pi) \right) , \qquad (2.57)$$

where $f_{B_J^*}$ is the production fraction of B_J^* mesons. Obviously $\frac{V}{V+P}$ is the interesting quantity to be compared with fragmentation models and simulations. According to Equation 2.57 the measured B^* production rate is exactly the primary B^* production rate if $\mathrm{BR}(B_J^* \to B^*\pi) = \frac{\sigma_{B^*}}{\sigma_{B^*}+\sigma_B}$. In addition to the feed-down from B_J^*, the B^* production fraction is affected by the $B^* - B$ mass difference since heavier particles are suppressed in the production mechanism. According to a simple fragmentation model [55] where the production of a quark pair in a colour string field is considered as a tunnelling process and the recombining of quarks to hadrons occur at an effective hadronization temperature $T \simeq 300$ MeV, the result $\frac{V}{V+P} = 0.72$ is obtained. Therefore, $\mathrm{BR}(B_J^* \to B^*\pi)$ is expected to be around 0.75 or slightly higher.

The analysis of the B^* production rate consequently leads us to the orbitally-excited B mesons. Given the predictions listed in Table 2.2 and Table 2.3, the four B_J^* states are expected to overlap in mass. So far analyses at LEP [56, 57, 58, 59] have reconstructed B_J^* in the $B\pi$ final state only, observing one single peak in the $B\pi$ mass spectrum. This is not sufficient to resolve any substructure of the four expected B_J^* states. In addition, for decays to $B^*\pi$ where the photon in the decay $B^* \to B\gamma$ is not detected, the reconstructed $B\pi$ mass is shifted by -46 MeV/c^2. A recent analysis [28] tries to cope with these problems by constraining all properties of the four B_J^* states according to HQET predictions except for the masses and widths of $B_1(1/2)$ and B_2^*.

In this thesis a different approach is presented. Using information of the photon in the decay $B^* \to B\gamma$, the $B_J^* \to B^*\pi^\pm(\pi)$ transitions can be separated from the $B_J^* \to B\pi^\pm(\pi)$ transitions. This allows a model independent measurement of

[15] See for example [54].

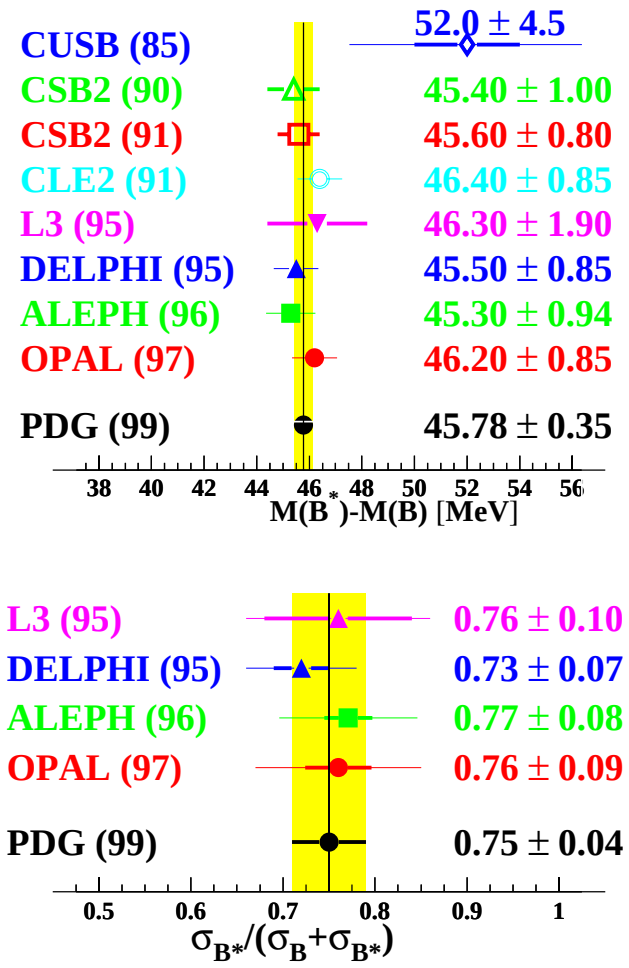

Figure 2.8: $B^* - B$ *mass splitting and* B^* *production rate.*

$BR(B_J^* \to B^*\pi(\pi))$ and thus a test of Equation 2.57. Furthermore, this method gives insight into the decomposition of the B_J^* into the states allowed to decay to $B\pi$ (B_0^* and B_2^*) from the other states that can only decay to $B^*\pi$. In this work, the information of B^* mesons and B_J^* mesons is combined and exploited in a systematic way for the first time.

In addition to the model independent measurement a model dependent fit to the $B\pi$ mass spectrum is performed. High statistics, extensive background studies and the tagging of the B^* decay are important prerequisites to perform this fit. Due to the complexity of the B_J^* signal and its different decay modes, several constraints, as provided by HQET, are imposed. From the fits, I obtain measurements of the masses and widths of B_0^* and $B_1(3/2)$, $BR(B_J^* \to B^*\pi)$, $BR(B_J^* \to B^{(*)}\pi\pi)$ and the fraction of narrow B_J^*, i.e. $B_1(3/2)$ and B_2^*, produced in the fragmentation process of a bottom quark.

Radially-excited B mesons, B' and $B^{*\prime}$, are expected to decay to the ground states B and B^* via single- and di-pion transitions. The experimental status of radially-excited B mesons is unclear. A preliminary DELPHI result [27, 60] is not yet confirmed. Also the $B^{(*)\prime}$ evidence presented in [28] is marginal and has to be questioned. In a separate project [61], the author was also involved in a search for radially-excited be mesons using the same data set as for the B^* and B_J^* analyses.

Chapter 3

The Experiment

3.1 The LEP storage ring

The **L**arge **E**lectron **P**ositron collider (LEP) at CERN (**C**entre **E**uropéen pour la **R**echerche **N**ucléaire) is a 26.6 km circumference storage ring designed to study e^+e^- interactions at centre-of-mass energies of up to 200 GeV [62, 63]. This ring is situated underground and has an approximate eightfold symmetry with 8 arcs and 8 long straight sections. The latter are used for particle physics experiments with the detectors ALEPH [64], L3 [65], DELPHI [66] and OPAL [67]. LEP uses a chain of other accelerators that already existed at CERN to pre-accelerate electrons and positrons, which are injected into the main ring with an energy of 22 GeV. The whole accelerator complex is shown in Figure 3.1.

From 1989-95, during the first phase of LEP (LEP1), Z^0 bosons were produced at rest with beam energies around 46 GeV. This energy was obtained with about 120 copper cavities. Since 1995, the beam energy has been raised in several steps to allow the production of W^+W^- and Z^0Z^0 pairs (LEP2 phase). This is made possible with the addition of about 200 superconducting cavities. This year the beam energy exceeded the maximum design value of 100 GeV, opening up an important new discovery domain. The work presented here deals with the data collected during the LEP1 phase on and near the Z^0 peak. The LEP program will be largely completed by the end of the year 2000 and the experimental facilities will be replaced by the next research instrument in Europe's particle physics armoury, the **L**arge **H**adron **C**ollider (LHC), making use of the LEP tunnel and the existing pre-accelerators.

Apart from the beam energy, the most important machine parameter is the luminosity defined as the interaction rate per unit cross section. For two beams with k bunches each having Gaussian transverse distributions with widths of σ_x and σ_y, number N_b of particles per bunch and revolution frequency f_0 the luminosity is given by

$$L = \frac{kN_b^2 f_0}{4\pi\sigma_x\sigma_y} .$$

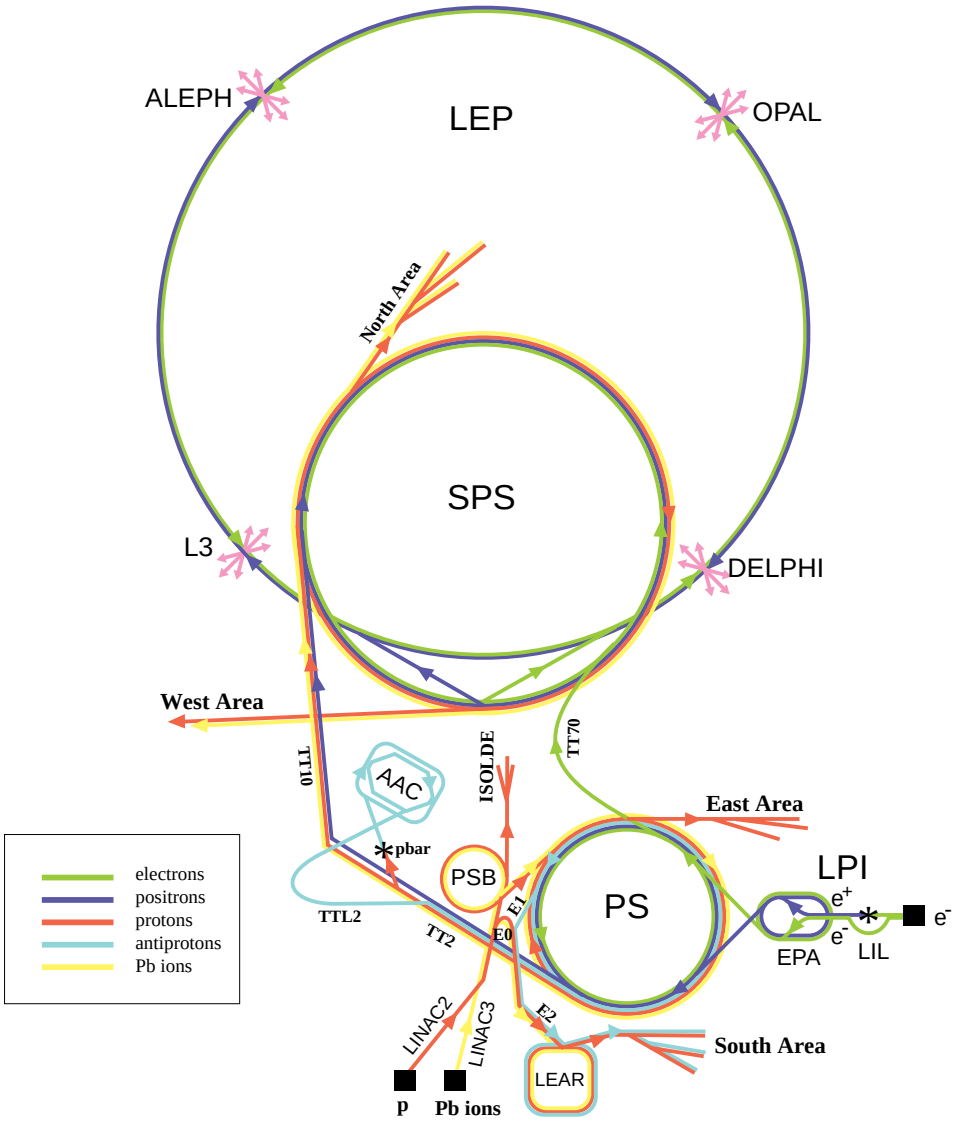

LEP: Large Electron Positron collider
SPS: Super Proton Synchrotron
AAC: Antiproton Accumulator Complex
ISOLDE: Isotope Separator OnLine DEvice
PSB: Proton Synchrotron Booster
PS: Proton Synchrotron
LPI: Lep Pre-Injector
EPA: Electron Positron Accumulator
LIL: Lep Injector Linac
LINAC: LINear ACcelerator
LEAR: Low Energy Antiproton Ring

Figure 3.1: *CERN accelerators including the LEP ring [68].*

During the years 1989-1995 a total integrated luminosity of $\mathcal{L} = \int L dt \approx 200\,\mathrm{pb}^{-1}$ has been delivered to each of the four experiments. As shown in Figure 3.2 the machine performance has increased every year. This improvement has been made possible by tuning of the beam optics and introducing different bunch train schemes. The number of bunches has been increased from 4+4 to 8+8. In 1995, tests

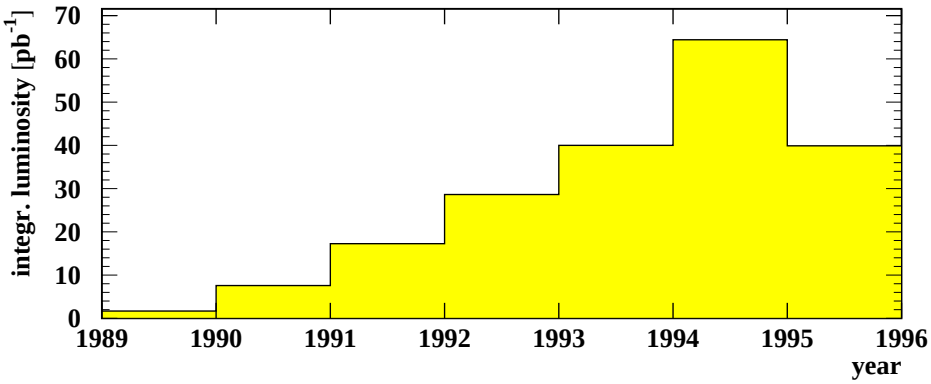

Figure 3.2: *Integrated luminosity per year and per experiment at centre-of-mass energies around $M(\mathrm{Z}^0)$. Part of 1995 data were already taken at higher energies, with another* $6.4\,\mathrm{pb}^{-1}$ *of luminosity produced.*

with a higher number of bunches and bunch trains produced similar luminosities. While the total current was increased, the running conditions were not as stable as in the 8+8 mode. The main limitation in luminosity comes from beam-beam effects caused by non-linear forces between the e^+ and the e^- beam. The design luminosity of about $14 \cdot 10^{30}\,\mathrm{cm}^{-2}\mathrm{s}^{-1}$ was exceeded already in 1993 and in 1994 and 1995 peak values of $20 \cdot 10^{30}\,\mathrm{cm}^{-2}\mathrm{s}^{-1}$ were reached. For the calibration of the mean energy of the beams a fantastic precision has been gained. The expected beam energy precision of 20 MeV has been outreached by an order of magnitude, taking into account many subtle effects such as the tide effects of the moon and the sun as well as leakage currents from the rails of trains passing near the LEP site [69].

3.2 The OPAL detector

OPAL (**O**mni-**P**urpose **A**pparatus for **L**EP) is a multipurpose apparatus designed to reconstruct products of $\mathrm{e}^+\mathrm{e}^-$ interactions over a solid angle of nearly 4π. Almost all types of events can be detected and reconstructed efficiently and classified unambiguously. A three-dimensional view of the detector is shown in Figure 3.3. Full details of the OPAL detector can be found in [67]. Only a brief introduction is

given here which partially summarises the subdetector descriptions given in [70]. The emphasis is on the subdetectors most important for this thesis. Also the central jet chamber is discussed in more detail since the author was involved in the online monitoring and control of the jet chamber high voltage system.

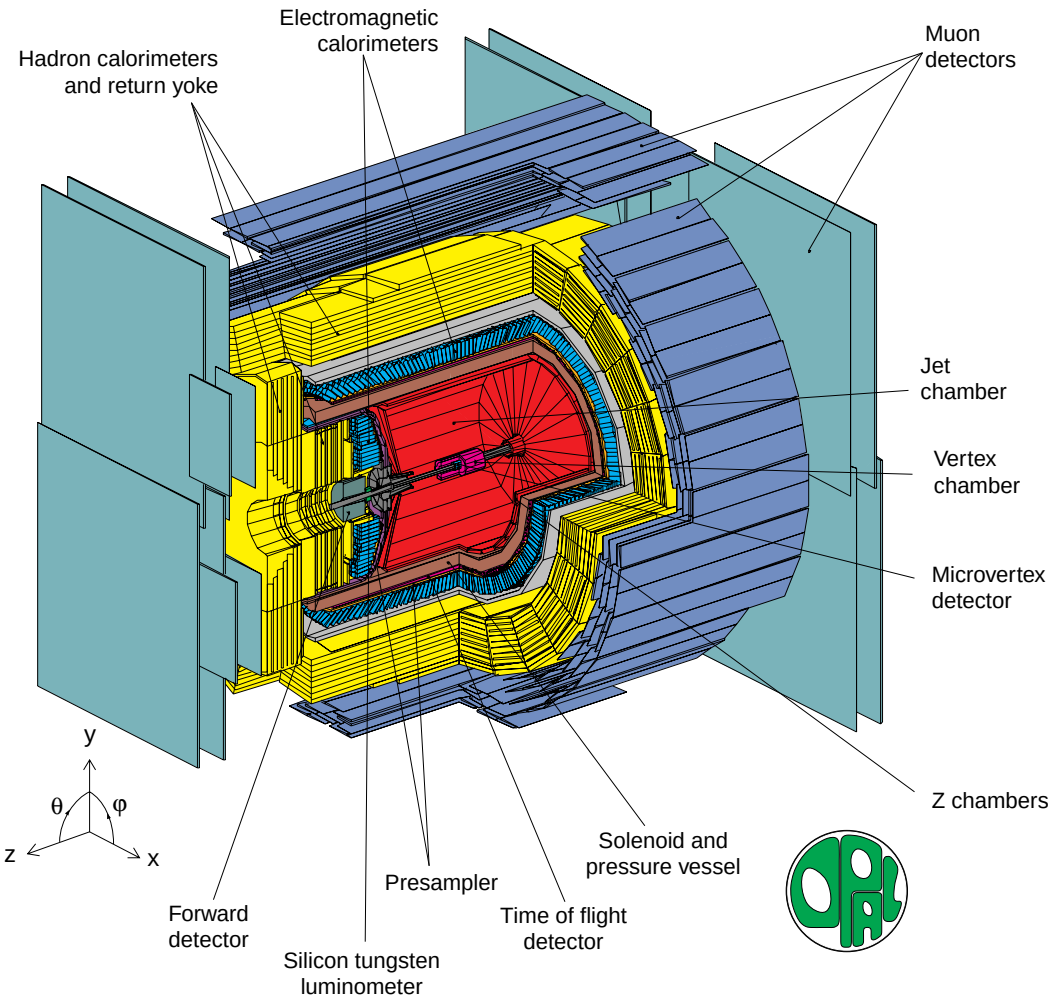

Figure 3.3: *General layout of the OPAL detector.*

3.2.1 The OPAL coordinate system

The OPAL **M**aster of **R**eference **S**ystem (MRS) is a three-dimensional Cartesian coordinate system as illustrated in Figure 3.3. The origin is at the nominal interaction point. The z axis lies along the beam pipe with the incident e^- direction as positive. The x axis points towards the centre of the LEP ring and the direction

of the y axis is chosen upwards to complete the right-handed coordinate system. Spherical coordinates have their standard definition relative to the OPAL coordinate system: the polar angle θ is measured from z and the azimuthal angle ϕ from x. Note that the plane defined by the LEP ring and thus the MRS is at an angle of 1.39% with respect to the horizontal plane.

A set of five parameters (κ, ϕ_0, d_0, $\tan\lambda$ z_0) describes a track within the MRS. The parameters are defined as follows:

- the curvature of the track is defined by $|\kappa| = 1/2\rho$ were ρ is the radius of curvature of the track at the point of closest approach to the MRS origin;
- ϕ_0 is the track tangent angle in the $x-y$ plane at the point of closest approach;
- d_0 is the impact parameter, i.e. is the distance from the origin to the point of closest approach in the $r-\phi$ plane;
- $\tan\lambda = \cot\theta$, where θ is the track polar angle from the $+z$ axis;
- z_0 is the z coordinate when the track is at the point of closest approach.

The impact parameter d_0 is defined with respect to the origin of the coordinate system and not with respect to the actual beam interaction point. For lifetime studies usually the impact parameter is calculated with respect to the primary event vertex. The so called corrected impact parameter is also denoted by d_0. The sign of the re-defined d_0 is positive if the point of closest approach of the track is in the same hemisphere of the event as the track. The hemisphere is defined as the plane containing the primary event vertex perpendicular to the axis of the jet containing the track under study.

3.2.2 The central detector

The Central Detector consists of a Silicon Microvertex detector [71, 72] and several drift chamber devices, the vertex detector, jet chamber [73, 74, 75] and surrounding z-chambers situated inside a pressure vessel holding a pressure of 4 bar. The central detector is inside a solenoid supplying a uniform axial magnetic field of 0.435 T. Before 1991 there was no Silicon detector and the inner wall of the pressure vessel at 7.8 cm radius formed the beam pipe. This beam pipe consists of 0.13 cm thick carbon fibre with a 100μm aluminium inner lining. In 1991 a second beam pipe at a radius of 5.35 cm, consisting of 0.11 cm thick Beryllium, was added and the Silicon detector inserted between them.

Silicon microvertex detector

The Silicon Microvertex Detector (SI) shown in Figures 3.4 and 3.5 consists of two barrels of single sided Silicon Microstrip Detectors at radii of 6 and 7.5 cm. The addition of this tracking device to OPAL became possible after the first LEP runs

when it was found that the low beam backgrounds permitted the use of a beam pipe with smaller diameter. The desire for a high spatial resolution detector was motivated by the need to measure or identify particles with typical decay lengths below a centimetre such as B mesons and τ leptons. Originally, the inner layer

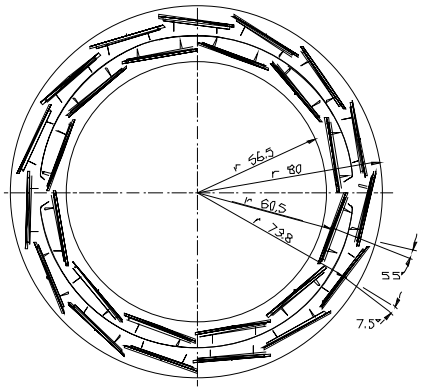

Figure 3.4: *$x-y$ view of the OPAL silicon microvertex detector μVTX3.*

consisted of 11 ladders and the outer of 14. Each ladder was 18 cm long and made of 3 silicon wafers daisy chained together. The detector was originally installed in OPAL in 1991 and had $r-\phi$ readout only. In 1993 an upgraded detector was installed that had $r-\phi$ and $r-z$ wafers glued back to back. For 1995, the detector was further upgraded (μVTX3). The number of ladders was increased to 12 and 15 and the ladders tilted to close ϕ gaps (Figure 3.4), thus ensuring 100% single hit coverage. The outer layer was also extended from 3 to 5 wafers with the interaction point still at the centre of the detector.

Vertex detector

The vertex detector (CV) is a high precision cylindrical jet drift chamber. It is 100 cm long with a radius of 23.5 cm and consists of two layers of 36 sectors each. The vertex detector is a 1 m long, 47 cm diameter, cylindrical drift chamber based on a scaled down jet chamber design. The chamber consists of an inner layer of 36 cells with axial wires and an outer layer of 36 small angle (4°) stereo cells.

A precise measurement of the drift time on to the axial sector sense wires allows the $r-\phi$ position to be calculated. Measuring the time difference between signals at either end of the sense wires allows a fast but relatively coarse z coordinate that is used by the OPAL track trigger and in pattern recognition. A more precise z measurement is then made by combining axial and stereo drift time information offline.

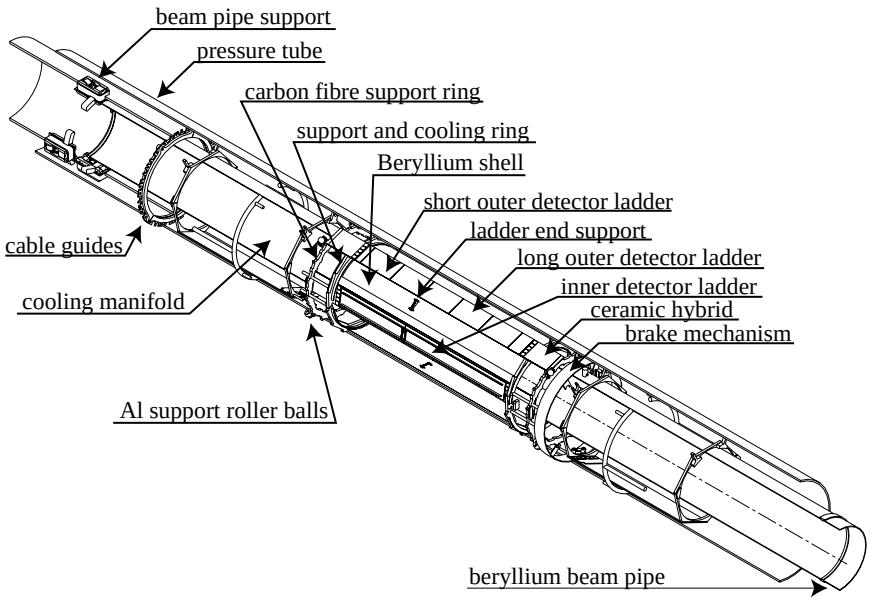

Figure 3.5: *Cutaway view of the OPAL silicon microvertex detector.*

Jet chamber

The jet chamber (CJ) is designed to measure the direction and the momentum of charged particles as well as the specific energy loss in the chamber gas. The general design principle was first established with the jet chamber of the JADE experiment [76] at PETRA. At each point true three-dimensional coordinates are determined from the wire position (r), the drift time (ϕ) and from a charge division measurement (z). The ratio of the integrated charges for each hit at both wire ends determines z, and the sum is used to calculate the energy loss, $\mathrm{d}E/\mathrm{d}x$. Many CJ details can be found in [73, 74, 75]. A few important aspects are briefly summarised in the following paragraphs.

The jet chamber is a cylindrical drift chamber of length 400 cm with an outer radius of 185 cm and inner of 25 cm (Figure 3.6). The chamber consists of 24 identical sectors each containing a plane of 159 sense wires and the same number of potential wires mounted alternately. For each sector, two cathode wire planes form the boundaries between adjacent sectors. The maximum drift distance varies from 3 cm to 25 cm. A schematic drawing of a jet chamber sector is given in Figure 3.7. All wires are stretched between two end plates which are held apart by a shell of 24 hollow aluminium plates located at the outer radius of the cylinder. To minimise the bending of the end plates under the force of the wires of about 14 tons the end plates are of conical shape with an angle of 15°. In order to resolve the left/right ambiguity the sense wires are mechanically staggered by ± 100 μm with respect to the potential wire plane. The sense wires are at ground potential. The

voltage at the potential wires determines the gas gain and is normally maintained at -2.38 kV.

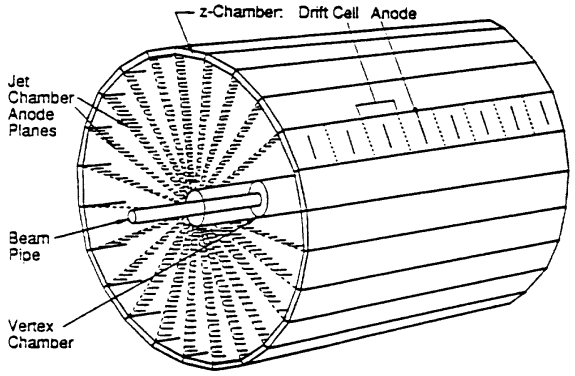

Figure 3.6: *Central detector schematic view.*

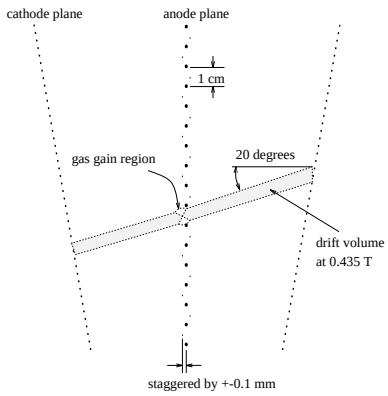

Figure 3.7: *CJ sector.*

The high voltage (HV) system has to supply voltages ranging from -25 kV at the outer feed points to -2.5 kV at the inner feed points of the cathodes. In order to avoid non-linearities in the drift field, four intermediate points are also supplied with high voltage. All 24 cathode planes are connected to the same power supplies to guarantee the same voltages throughout the chamber. The currents flowing into the resistor chains of the cathodes are monitored separately at each feed point of each cathode with high accuracy. All potential wires of one sector are supplied by one power supply but the currents in the chamber are monitored individually per group of 16 wires using similar current meters as for the cathodes. The sense wire currents are monitored with a precision of 1 nA again in groups of 16 wires. For adjusting the voltages a master/slave system is used where the master ramps all voltages simultaneously according to the slave settings.

To protect the chamber against overcurrents, the current measuring circuits are equipped with comparators. If the current in any of the HV lines of the cathode exceeds the hardwired threshold, all power supplies are disconnected and the potential wires are grounded by a fast transistor switch in about 2 μs. An overcurrent in one of the potential wire groups activates only the potential wire protection circuit.

For the safety of the central jet chamber, a monitoring and alarm system of the high voltage is mandatory. In a one-year project, a new monitoring system has been developed and implemented by the author in collaboration with other jet chamber hardware experts. The goal of the new system was a faster determination of the chamber high voltage status and a faster and more flexible reaction in critical situations. The new expert system became necessary because of the changed beam and background conditions at higher beam energies. The new monitoring software is based on a client-server structure written in C and is running on a UNIX workstation. The graphics user interface is written in Tcl/Tk and guarantees a

simple and safe handling of all necessary actions to steer the high voltage, analyse critical situations and react on high voltage alarms triggered by the software or directly by the chamber hardware. A complete simulation of all chamber features relevant for the high voltage monitoring has been developed and can be used to determine software errors, to study special situations or to train new shift crew members. In the context of the monitoring software development also a thesis for the first state examination for teachers was completed. The results of this thesis are documented in [77]. The new monitoring software is much more flexible, provides more information in a customised data format and allows a faster reaction in the case of a high voltage alarm condition. Therefore, the new software decreased the dead time of the chamber after an alarm substantially and thus helped to increase the total data taking efficiency of the OPAL detector. The new monitoring system is also much more comfortable for the experts, as all important informations concerning the high voltage status are e.g. transferred via internet and warning/alarm messages are automatically sent to the experts mobile phone. After a test phase of several months the new HV monitor is running permanently without any problems.

z-chambers

The z-chambers are arranged to form a barrel layer around the jet chamber covering the polar angle $|\cos\theta| < 0.72$ and 94% of the azimuthal angle. They are designed to make precise measurements of the z coordinates of charged particles as these leave the jet chamber and thus to improve both the polar angle and invariant mass resolutions. They consist of a layer of 24 drift chambers 400 cm long, 50 cm wide and 5.9 cm thick. Each chamber is divided in z into 8 cells of 50 cm$\times$50 cm, with every cell containing 6 sense wires spaced at 0.4 cm.

Performance of the inner tracking system

The most important essential of the tracking system performance is the spatial resolution of charged tracks. The observed resolutions are different for different subdetectors as well as different directions. In Table 3.1 the observed single and double hit resolutions are presented [78].

resolution	SI	CV	CJ	CZ
single hit resolution in $r-\phi$	10 μm	55 μm	135 μm	1.5 cm
single hit resolution in z	15 μm	1.0 mm	4.5-6.0 cm	300 μm
double hit resolution in $r-\phi$		2 mm	2.5 mm	

Table 3.1: *Single and double hit resolutions for different subdetectors of the inner tracking system. White space indicates that the corresponding quantity is not precisely known.*

More important for physics analyses is the combined tracking performance of the entire tracking system. The numbers shown in Table 3.2 were obtained from $Z^0 \to \mu^+\mu^-$ decays of 1995 data [78]. The performance from year to year varies by a few percent. The momentum resolution in the barrel can be parameterised by

$$\frac{\sigma_p}{p} = \frac{\sigma_{p_t}}{p_t} = \sqrt{0.02^2 + (1.5 \cdot 10^{-3} \cdot p_t)^2}\,,$$

where 0.02 is a constant to account for the multiple scattering error and the factor $1.5 \cdot 10^{-3}$ is the measurement error with p_t measured in GeV/c. Tor a track with $p_t = 45$ GeV/c we thus obtain a relative momentum resolution of 7%. In the endcap region the momentum resolution depends strongly on $|\cos\theta|$ due to the given detector geometry. Note that the silicon microvertex detector clearly improves the impact parameter resolutions for d_0 and z_0. Good impact parameter resolutions are essential for a precise lifetime information. The latter dominates the $Z^0 \to b\overline{b}$ tagging performance which is essential for any B meson analysis.

resolution	CJ only	CV+CJ+CZ	SI+CV+CJ+CZ
mom. res. σ_p/p^2 [GeV/c^{-1}]	$41.4 \cdot 10^{-3}$	$1.3 \cdot 10^{-3}$	$1.25 \cdot 10^{-3}$
d_0 resolution	88 μm	39 μm	16 μm
z_0 resolution	5.3 cm	930 μm	22 μm
θ resolution	13.9 mrad	1.4 mrad	1.4 mrad (?)
ϕ resolution	0.32 mrad	0.29 mrad	0.275 mrad

Table 3.2: *The combined tracking performance of the entire tracking system obtained from* $Z^0 \to \mu^+\mu^-$ *decays.*

3.2.3 The electromagnetic calorimeter

The electromagnetic calorimeter detects and measures the energies and positions of electrons and photons ranging from tens of MeV to 100 GeV. It consists of a lead glass total absorption calorimeter split into a barrel and two end cap arrays. This arrangement or partially overlapping assemblies together with two forward lead scintillator calorimeters of the forward detector gives an acceptance for electron and photon detection of almost 99% of the solid angle.

The presence of ~2 radiation lengths of material in front of the calorimeter (mostly due to the solenoid and pressure vessel), results in most electromagnetic showers initiating before reaching the lead glass. Presampling devices are therefore installed in front of the lead glass in the barrel and endcap regions to measure the position and energy of showers to improve overall spatial and energy resolution and give additional γ/π^0 and electron/hadron discrimination. In front of the Barrel Presampler is the Time of Flight Detector.

Time-of-flight counters

The Barrel time-of-flight (TB) system provides charged particle identification in the range 0.6 to 2.5 GeV, fast triggering information and an effective rejection of cosmic rays. It consists of 160 scintillation counters forming a barrel layer 684 cm long at a mean radius of 236 cm surrounding the OPAL coil covering the polar angle range $|\cos\theta| < 0.82$.

Electromagnetic presampler

The Barrel Electromagnetic Presampler (PB) consists of 16 chambers forming a cylinder of radius 239 cm and length 662 cm covering the polar angle range $|\cos\theta| < 0.81$. Each chamber consists of two layers of drift tubes operated in the limited streamer mode with the anode wires running parallel to the beam direction. Each layer of tubes contains 1 cm wide cathode strips on both sides at $\pm 45°$to the wire direction. Spatial positions can then be determined by reading out the strips in conjunction with a measurement of the charge collected at each end of the wires to give a z coordinate by charge division. The hit multiplicity is approximately proportional to the energy deposited in the material in front of the presampler allowing the calorimeter shower energy to be corrected with a corresponding improvement in resolution.

The endcap presampler (PE) is a multi-wire proportional counter located in the region between the pressure bell and the endcap lead glass detector. The device consists of 32 chambers arranged in 16 sectors covering all ϕ and the polar angle range $0.83 < |\cos\theta| < 0.95$.

Lead glass calorimeter

The barrel lead glass calorimeter (EB) consists of a cylindrical array of 9440 lead glass blocks at a radius of 246 cm covering the polar angle range $|\cos\theta| < 0.81$. Each block is 24.6 radiation lengths, 37 cm in depth and $\sim 10 \times 10$ cm^2. In order to maximise detection efficiency the longitudinal axis of each block is angled to point at the interaction region. The focus of this pointing geometry is slightly offset from the e^+e^- collision point in order to reduce particle losses in the gaps between blocks.

Čerenkov light from the passage of relativistic charged particles through the lead glass is detected by 3 inch diameter phototubes at the base of each block.

The endcap electromagnetic calorimeter (EE) consists of two dome-shaped arrays of 1132 lead glass blocks located in the region between the pressure bell and the pole tip hadron calorimeter. It has an acceptance coverage of the full azimuthal angle and $0.81 < |\cos\theta| < 0.98$.

As opposed to the barrel calorimeter, the endcap lead glass blocks follow a non-pointing geometry being mounted coaxial with the beam line. The lead glass blocks provide typically 22 radiation lengths of material and come in three lengths

(38, 42 and 52 cm) to form the domed structure following the external contours of the pressure bell.

The blocks are read out by special Vacuum Photo Triodes (VPTs) operating in the full OPAL magnetic field.

3.2.4 The hadron calorimeter

The hadron calorimeter is built in three sections - the barrel, the endcaps and the pole-tips. By positioning detectors between the layers of the magnet return yoke a sampling calorimeter is formed covering a solid angle of 97% of 4π and offering at least 4 interaction lengths of iron absorber to particles emerging from the electromagnetic calorimeter. Essentially all hadrons are absorbed at this stage leaving only muons (and the undetected neutrinos) to pass on into the surrounding muon chambers.

To correctly measure the hadronic energy, the hadron calorimeter information must be used in combination with that from the preceding electromagnetic calorimeter. This is necessary due to the likelihood of hadronic interactions occurring in the 2.2 interaction lengths of material that exists in front of the iron yoke.

The barrel region (HB) contains 9 layers of chambers sandwiched between 8 layers of 10 cm thick iron. The barrel ends are then closed off by toroidal endcap regions (HE) which consist of 8 layers of chambers sandwiched between 7 slabs of iron. The chambers themselves are limited streamer tube devices.

Complementing the barrel and endcap regions, the pole-tip (HP) extends the coverage of hadron calorimetry from $|\cos\theta| = 0.91$ down to 0.99. The sampling frequency in this region is increased to 10 in an effort to improve the OPAL energy resolution in the forward direction.

3.2.5 The muon detector

The barrel muon detector (MB) consists of 110 drift chambers mounted in (at least) four layers in the region $|\cos\theta| < 0.68$. As the particles incident on the detector have traversed the equivalent of 1.3 m of iron the probability of a hadron not interacting before reaching the muon chambers is less than 0.001. Each chamber is split into two adjoining cells each containing an anode signal wire running the full length of the cell, parallel to the beamline. The inner surfaces of the cells have 0.75 cm cathode strips etched in them to define the drift field and in the regions directly opposite the anode wires are diamond shaped cathode pads. In all, six signals are read out from each cell namely, one from each end of the anode wire and four from the cathode pads and are digitised via an 8-bit FADC.

Spatial position in the ϕ plane is derived using the drift time onto the anode and can be reconstructed to an accuracy of better than 0.15 cm. A rough estimate of the z coordinate is also achieved by using the difference in time and pulse height of the signals arriving at both ends of the anode wire. A much better measure

of the z coordinate is given by using induced signals on two sets of cathode pads resulting in a z coordinate accuracy of 0.2 cm.

Each endcap muon detector (ME) consists of two layers of four quadrant chambers (6 m×6 m) and two layers of two patch chambers (3 m×2.5 m), for an angular coverage of $0.67 < |\cos\theta| < 0.985$. Each chamber is an arrangement of two layers of limited streamer tubes in the plane perpendicular to the beam line, where one layer has its wires horizontal and the other vertical.

3.2.6 The forward detector

The forward detector (FD) consists of an array of the following devices: A lead scintillating sampling calorimeter divided in a presampler and a main calorimeter, three layers of proportional tube chambers, a ring of lead scintillator sandwich sections called Gamma Catcher and the Far Forward Monitor mounted on either side of the beampipe about 8 m from the interaction point. The primary task of the forward detector is to detect low angle Bhabha scattering events as a way of determining the LEP luminosity for the normalization of measured reaction rates from Z^0 decays.

3.2.7 The silicon tungsten detector

The silicon tungsten detector (SW) is a sampling calorimeter designed to detect low angle Bhabha scattering events in order to measure the luminosity. There are 2 calorimeters at ±238.94cm in z from the interaction point with an angular acceptance of 25 mrad to 59 mrad. Each calorimeter consists of 19 layers of silicon detectors and 18 layers of tungsten. At the front of each calorimeter is a bare layer of silicon to detect pre-showering, the next 14 silicon layers are each behind 1 radiation length (3.8mm) of tungsten and the final 4 layers are behind 2 radiation lengths (7.6 mm) of tungsten.

3.3 The trigger and online system

Events are only recorded by the data acquisition system if they satisfy certain (pre-)trigger conditions. The trigger system is designed to keep a high efficiency for all considered physics reactions while the trigger rates are kept low. It reduces the 45 kHz beam crossing rate to a trigger rate of a few Hz, using information from the tracking chambers, the time-of-flight system, calorimetry and muon detectors. Subdetector trigger signals divide into two categories, stand-alone signals such as multiplicity counts or energy sums, and lower threshold signals from a 6×24 binning in θ and ϕ respectively. The trigger processor makes its decision by forming correlations in space between subdetectors in θ/ϕ together with the stand-alone signals. If an event is selected by the trigger, each of the subdetectors is read out separately by its own special front-end readout electronics into its local

system crates. The event builder assembles the complete event observed by the subdetectors.

The so called filter acts as a second-level software trigger and performs a partial online reconstruction of the digitised events to allow a further rejection of backgrounds (15-35 % of all triggers). This further reduces backgrounds like interactions of off-momentum electrons with the beam pipe, cosmic rays and detector noise and performs an event classification of the surviving reactions. The surviving events are checked, analysed and compressed before being written in 20 Mbyte partititions to disk. All these files are copied from the filter disk to the so called ROPE farm (**R**econstruction of **O**PAL **P**hysics **E**vents), which is a collection of HP UNIX workstations. At this stage the raw data from the subdetectors and the information from the OPAL calibration database is used to reconstruct tracks and energy clusters and to produce a summary of the most important information in the event. Data copied from the filter are written to optical disk as a permanent store. Events passing the special physics selections (`phys1`) are stripped off, and copied over the network to the SHIFT (**S**caleable **H**eterogeneous **I**ntegrated **F**acili**T**y) system on the main CERN site. Now the data files can be used for the offline data analysis.

More information on the OPAL trigger system and the online event filter can be found in [79, 80, 81].

3.4 Detector simulation

The whole OPAL detector and its inner workings are simulated using the GOPAL [82, 83] program which is based on the CERN GEANT3 detector modelling package [84].

GEANT is a toolkit for the simulation of the passage of particles through matter. Its application areas include high energy physics and nuclear experiments, medical, accelerator and space physics studies. GEANT provides a set of tools for all the domains of detector simulation: geometry, tracking, detector response, run, event and track management, visualisation and a user interface. An abundant set of physics processes handle the diverse interactions of particles with matter across a wide energy range. For many physics processes a choice of different models is available. In addition a large set of utilities, including a powerful set of random number generators, physics units and constants, Particle Data Group compliant particle management, as well as interfaces to event generators complete the toolkit.

In a first step of the simulation procedure events are produced using a Monte Carlo event generator. Then the generated particles of each event are tracked through the detector volumes. The interactions of these particles with the material and the detector response is simulated by GOPAL. Finally the simulated events are digitised producing the raw data equivalent to that from the real experiment (plus additional information on the nature of the simulated physics process). The simulated raw data produced by GOPAL can be analysed using the OPAL

reconstruction software in the same way as the real data from the detector.

Chapter 4

Analysis Overview

The aim of this thesis is a comprehensive analysis of the spectroscopy of all low lying recurrences of non-strange B mesons. Inclusively reconstructed B mesons are combined with photons or charged pions to form B^*, B_J^*, $B^{(*)\prime}$ or any other excitation giving the same set of particles in the decay. Signals for excited states are sought in the invariant mass spectra.

The focus of this work is on a separation of B_J^* transitions to B^* from B_J^* transitions to B. This allows a model independent measurement of $BR(B_J^* \to B^*\pi(\pi))$ and gives insight into the decomposition of the B_J^* multiplet (see Chapters 2 and 9). The main part of the analysis is based on the reconstruction of B^* in the $B\gamma$ final state and a separate reconstruction of B_J^* in the $B\pi^\pm$ final state. A direct reconstruction of B_J^* decaying to $B^*\pi$, $B^* \to B\gamma$ giving $B\gamma\pi^\pm$ in the final state is inappropriate because of the large combinatorial background and the insufficient detector resolution. Therefore, this approach employs a statistical separation of $B_J^* \to B^*\pi^\pm(\pi)$ from $B_J^* \to B\pi^\pm(\pi)$ decays.

B mesons produced in $Z^0 \to b\overline{b}$ events (Chapter 5) are selected inclusively to achieve high efficiency. No attempt is made to reconstruct specific B decay channels. On the contrary, properties common to all weakly decaying b hadrons are used for the B reconstruction (Chapter 6). For each B candidate, a weight $\mathcal{W}(B^*)$ is constructed using photon conversions and photons measured in the electromagnetic calorimeter. This weight represents the probability that the B meson is produced in the decay of a B^* (Chapter 7). All B candidates are then combined with charged pions to form B_J^* meson candidates (Chapter 8). Using the weight $\mathcal{W}(B^*)$ two mutually exclusive subsamples of $B\pi^\pm$ combinations are selected, one enriched and the other depleted in its B^* content. Invariant $B\pi^\pm$ mass distributions are formed for both samples. The shape of the non-B_J^* background of the two distributions is taken from Monte Carlo simulations and normalised to the data in the upper sideband region and subtracted from the corresponding data distributions. From the observed number of B_J^* and the different efficiencies for $B_J^* \to B^*\pi^\pm(\pi)$ and $B_J^* \to B\pi^\pm(\pi)$ decays in the B^*-enriched and the B^*-depleted samples the branching ratio $BR(B_J^* \to B^*\pi(\pi))$ is obtained (Section 9.1). Apply-

ing a simultaneous fit to the $B\pi$ mass spectra of both samples several details of the B_J^* four-state composition and of the B_J^* decay modes are extracted. These fit results are compared with the results obtained from a fit to the total $B\pi$ mass spectrum where no B^* information is available. Whereas the $BR(B_J^* \to B^*\pi(\pi))$ result obtained from counting the number of B_J^* signal entries of the samples enriched or depleted in the decay $B_J^* \to B^*\pi^\pm(\pi)$ is model independent and does not rely on the shape of the $B\pi$ signal, the fits to the $B\pi$ mass spectra make use of HQET assumptions on the composition and the decay modes of the B_J^* signal.

Also the $B\pi^+\pi^-$ final state is studied to search for radially-excited states. The additional pion increases the number of random track combinations drastically. The di-pion selection is optimised to maximise the signal significance. The observed excess in the $B\pi^+\pi^-$ mass spectrum is expected to contain a substantial $B_J^* \to B^{(*)}\pi\pi$ contribution and is compared with the results obtained from the fits to the B_J^* mass spectrum (Chapter 10).

Extensive systematic studies are performed to define the size of systematic uncertainty for each measurement. The poor knowledge of the fragmentation process and uncertainties of the background composition cause the dominant error contributions (Chapter 11).

Chapter 5

Selection of $Z^0 \to b\bar{b}$ Decays

At LEP, B mesons are predominantly produced in the process $e^+e^- \to Z^0/\gamma^* \to b\bar{b}$. Since the photon exchange is suppressed by a factor of about 100 with respect to the Z^0 exchange at $\sqrt{s} \approx M(Z^0)$, only the Z^0 notation is used in the following. To suppress background sources such as leptonic decays of the Z^0 and photon-photon interactions, a pre-selection of $Z^0 \to q\overline{q}$ decays is performed where q denotes all quark flavours except the top quark. The criteria used to select those multi-hadronic Z^0 decays are based on energy clusters in the electromagnetic calorimeters and the charged track multiplicity.

About 21.6% of the hadronic decays are $Z^0 \to b\overline{b}$ decays. To discard the background of light and charm quark decays, the $Z^0 \to b\overline{b}$ selection makes use of lifetime information, event shape variables and a high p_t lepton tag.

The first section of this chapter describes the selection of hadronic decays of the Z^0. In the second section the tagging of $Z^0 \to b\overline{b}$ decays is presented. Both the $Z^0 \to q\overline{q}$ and the $Z^0 \to b\overline{b}$ selections are standard OPAL procedures. Whereas the selection of hadronic decays is widely used in LEP1 analyses, the described selection of decays into bottom quarks so far has been used in LEP2 analyses only.

5.1 Selection of hadronic decays

For the $Z^0 \to q\overline{q}$ selection, the following criteria are applied to clusters and tracks. Clusters in the barrel region are required to have a minimum energy of 100 MeV, and clusters in the end cap detectors are required to contain at least two adjacent lead glass blocks with a combined energy of at least 200 MeV. Tracks are required to have at least 20 measured space points out of a possible 159 per jet chamber sector and a distance of closest approach to the interaction point of less than 2 cm in the direction perpendicular to the beam axis and less than 40 cm along the beam axis. Only tracks with a minimum momentum component transverse to the beam direction of 50 MeV/c are selected. The radial distance with respect to the z axis of the first measured hit in the inner tracking chambers is required to be smaller than 60 cm and the χ^2 of the track fit has to be smaller than 999. A

hadron candidate is defined by the following requirements[1] [85]:

- at least 7 clusters;
- at least 5 tracks;
- a total energy deposited in the lead glass calorimeters of at least 10% of the centre-of-mass energy: $\sum E_{\text{cluster}}/\sqrt{s} > 0.1$, where E_{cluster} is the energy of each cluster;
- an energy imbalance along the beam direction with

$$\left| \sum (E_{\text{cluster}} \cdot \cos\theta) \right| / \sum E_{\text{cluster}} < 0.65 \,,$$

  where θ is the polar angle of the cluster.

The cuts on the number of clusters and the number of tracks mainly remove background from charged lepton pairs. The other two cuts efficiently reject photon-photon, beam-gas and beam-wall events as well as interactions caused by cosmic rays. The principal remaining backgrounds in the hadronic data sample are $\tau^+\tau^-$ events and two-photon multi-hadronic events. The total background is estimated to be less than 2%. The efficiency of the $Z^0 \to q\overline{q}$ selection is determined to be $(98.4 \pm 0.4)\%$. At this stage, a sample of about 4 million hadronic events is selected using the whole LEP1 data set. The event display of a typical hadronic decay is shown in Figure A.1 in Appendix A. Further details and systematic studies concerning the hadronic event selection can be found in [85].

In addition to the standard detector status requirements of the hadronic event selection only data with the silicon microvertex detector being fully functional are considered. This ensures an excellent tracking data quality (see also Table 3.2). Each event is divided into two hemispheres by the plane perpendicular to the thrust axis and containing the interaction point of the event. The thrust axis is calculated using charged tracks and electromagnetic clusters not associated with any tracks. To select events within the fiducial acceptance of the silicon microvertex detector and the barrel electromagnetic calorimeter, the thrust axis direction[2] is required to satisfy $|\cos\theta_T| < 0.8$.

5.2 Selection of $Z^0 \to b\overline{b}$ decays

Standard methods for the tagging of b flavoured quarks are based mainly on lifetime information. At OPAL several different tagging algorithms are available. The best performance in terms of efficiency versus purity is obtained with the highly developed b-tagger described in Section 5.2.1. This tool has been used e.g. in the search for the Standard Model Higgs boson. In Section 5.2.2 its performance is compared with other b-tagging methods.

[1] This is the so called Tokyo Multi-hadron Event Selection.

[2] The definition of the OPAL coordinate system and spherical coordinates is given in Section 3.2.1.

5.2.1 The LEP2 standard b-tagger

To achieve optimal b-tagging performance, each event is forced into a 2-jet topology using the Durham jet finding scheme [86, 87, 88, 89]. In calculating the visible energies and momenta of the event and of individual jets, corrections are applied to prevent double counting of energy in the case of tracks with associated clusters [90]. The b-tagging algorithm is applied to each jet using three independent methods: lifetime tag, high p_T lepton tag and jet shape tag. These three tagging methods, described below, are combined using an unbinned likelihood method to form a single discriminating variable $\mathcal{B}_{\text{jet}}$ for each jet. The following description of the algorithm summarises the information given in [91].

The lifetime tag makes use of the long lifetime, high decay multiplicity and high mass of b hadrons. Five quantities are calculated from the tracks and clusters assigned to a given jet and input to an artificial neural network. The neural network output is the b-flavour lifetime tag variable β_τ. The first three of the input quantities rely on the reconstruction of secondary vertices in sub-jets. The last two are based on track impact parameters only to compensate any losses in b-tagging efficiency from the secondary vertex reconstruction:

- The secondary vertex likelihood
  is based on secondary vertex multiplicity and vertex decay length significance (i.e. the decay length divided by its error) information.

- The reduced secondary vertex likelihood
  is calculated like the secondary vertex likelihood but using all tracks except the one with the largest impact parameter significance with respect to the primary vertex.

- The critical track discriminator
  is obtained from neural networks designed to separate b hadron decay tracks from fragmentation tracks. All tracks in a sub-jet are ordered according to their neural net output in descending order. Tracks are added one by one and for each resulting subset of tracks the invariant mass is calculated assuming the pion mass for each track. The neural network output of the track which causes the invariant mass to exceed 1.9 GeV/c^2 is the critical track discriminator.

- The impact parameter joint probability
  is the joint probability of all tracks in a jet to have come from the primary vertex and is calculated from the two-dimensional impact parameter significances of all tracks and the impact parameter resolution function. The latter is obtained from tracks with negative impact parameter significances.

- The impact parameter mass tag
  is derived from tracks of a sub-jet sorted in descending order of the impact parameter significance. The invariant mass is calculated as in the case of the

critical track discriminator. The impact parameter significance of the track which causes the invariant mass of the subset of tracks to exceed 1.2 GeV/c^2 is used as another input for the lifetime neural network.

Figure 5.1a shows the distribution of the lifetime neural network output β_τ per jet in the central detector region for $Z^0 \to q\bar{q}$ events for OPAL data at $\sqrt{s} = M(Z^0)$ together with the Monte Carlo simulation.

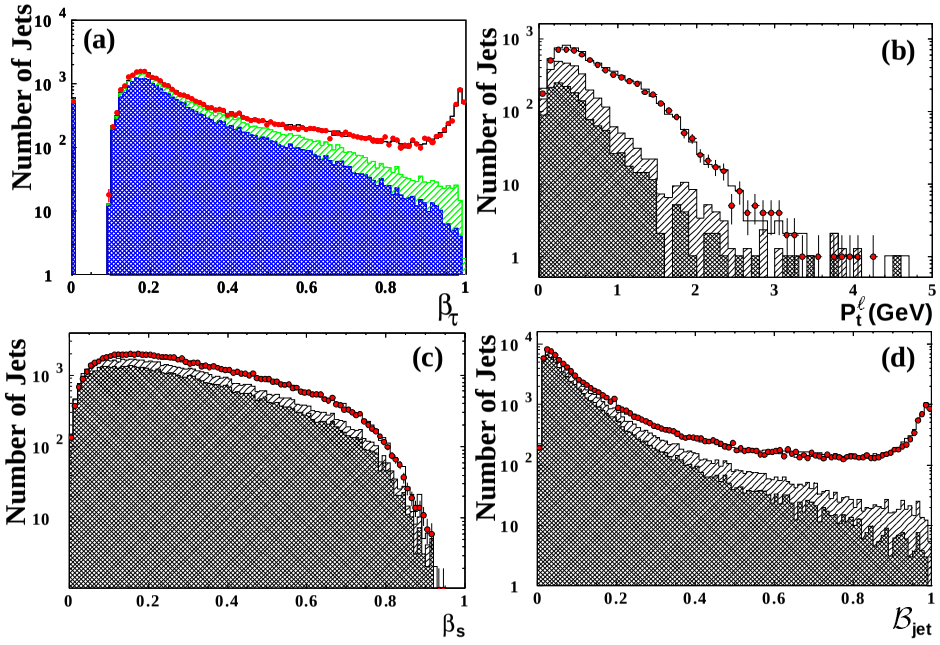

Figure 5.1: *(a) Lifetime neural network output β_τ for jets with the jet axis within the region $|\cos\theta_{jet}| \leq 0.75$; (b) p_t spectrum for events with tagged electrons/muons; (c) distribution of boosted sphericity, β_s; (d) distribution of $\mathcal{B}_{\rm jet}$. The histograms are Monte Carlo simulations of $Z^0 \to q\bar{q}$ decays for different flavours (cross-hatched: uds; hatched: charm; open: bottom); the dots with error bars are OPAL data taken in 1997 at $\sqrt{s} = M(Z^0)$. The figure is taken from [91].*

Semileptonic b-decays are identified using electron and muon selections. Electrons from γ conversions are rejected. The transverse momentum p_t^ℓ of the lepton, calculated with respect to the direction of the sub-jet which includes the lepton track, is used as a b-tag variable. The p_t^ℓ spectrum of the tagged leptons for $Z^0 \to q\bar{q}$ events is shown in Figure 5.1b together with the Monte Carlo simulation.

The larger decay multiplicity and higher mass of the b-flavoured hadrons tend to result in a more spherical shape for b-jets compared to lighter flavour jets. As a measure of the jet shape, the boosted sphericity β_s, defined as the sphericity of the jet calculated in its rest frame, is used as a jet shape tag. The distribution of β_s is shown in Figure 5.1c.

The three quantities β_τ, p_t, and β_s, exploit different properties of b hadron decays which are almost uncorrelated. Therefore they are combined using an unbinned likelihood method to obtain the final b-tagging discriminant $\mathcal{B}_{\text{jet}}$ shown in Figure 5.1d. Good agreement can be seen between data and Monte Carlo simulation. The efficiency of the algorithm has been verified from identified $Z^0 \to b\overline{b}$ events at $\sqrt{s} = M(Z^0)$ using a double tagging method.

The b-tagging discriminants calculated for each of the two jets in the event are combined to yield an event b likelihood $\mathcal{B}_{\text{event}}$:

$$\mathcal{B}_{\text{event}} = \frac{\mathcal{B}_{\text{jet}1} \cdot \mathcal{B}_{\text{jet}2}}{(1 - \mathcal{B}_{\text{jet}1}) \cdot (1 - \mathcal{B}_{\text{jet}2}) + \mathcal{B}_{\text{jet}1} \cdot \mathcal{B}_{\text{jet}2}} \,. \tag{5.1}$$

For each event, $\mathcal{B}_{\text{event}} > 0.6$ is required. After this cut, the $Z^0 \to b\overline{b}$ event purity is about 96%. The cut on the direction of the event thrust axis, $|\cos\theta_T| < 0.8$, as described in Section 5.1, removes roughly a quarter of all $Z^0 \to b\overline{b}$ events and after the cut on $\mathcal{B}_{\text{event}}$, the total b event tagging efficiency with respect to all produced $Z^0 \to b\overline{b}$ events is about 49%, where these numbers are obtained from Monte Carlo simulation. At this stage, about 750 000 b hadron candidates are selected.

5.2.2 Comparison with other b-taggers

Traditional b-tagging algorithms are based on separated secondary vertices with high multiplicity. In [92] for example, a secondary vertex is reconstructed by fitting the charged tracks passing a set of track quality criteria to a common point in the x-y plane. Each track considered in the fit is required to have a momentum greater than 0.5 GeV/c, a distance of closest approach $|d_0|$ in the x-y plane to the primary vertex smaller than 0.3 cm, and an error σ_{d_0} smaller than 0.1 cm. Tracks with a large χ^2 contribution to the fit are removed one by one, until all remaining tracks contribute less than 4 to the χ^2. In a b jet, because of the large average track multiplicity of b hadron decays and the hard fragmentation of the b quark, the tracks retained by the algorithm are more likely to be those from the b hadron decay. With cuts on the vertex multiplicity and the vertex decay length significance, the desired impurity or efficiency can be selected. In Figure 5.2 the impurity-efficiency curve of this vertex finder (adapted to work in 3 dimensions) is presented (BTGVFT 3 track). The efficiency is calculated with respect to the $Z^0 \to q\overline{q}$ selection presented in Section 5.1. In contrast to the BTGVFT 'tear down' vertex finder, the BTSVTX 'build up' vertex finder starts by forming a nucleus secondary vertex from tracks with high impact parameter significances with respect to the primary vertex. Tracks are added to the nucleus if they are closer to the secondary than the primary vertex. Although the approaches of both vertex finders are quite different, the performance is rather similar (see Figure 5.2). Neural networks can be trained using the same information as the vertex finders as input variables. The neural networks have superior performance since they make optimal use of the available information and exploit additional information

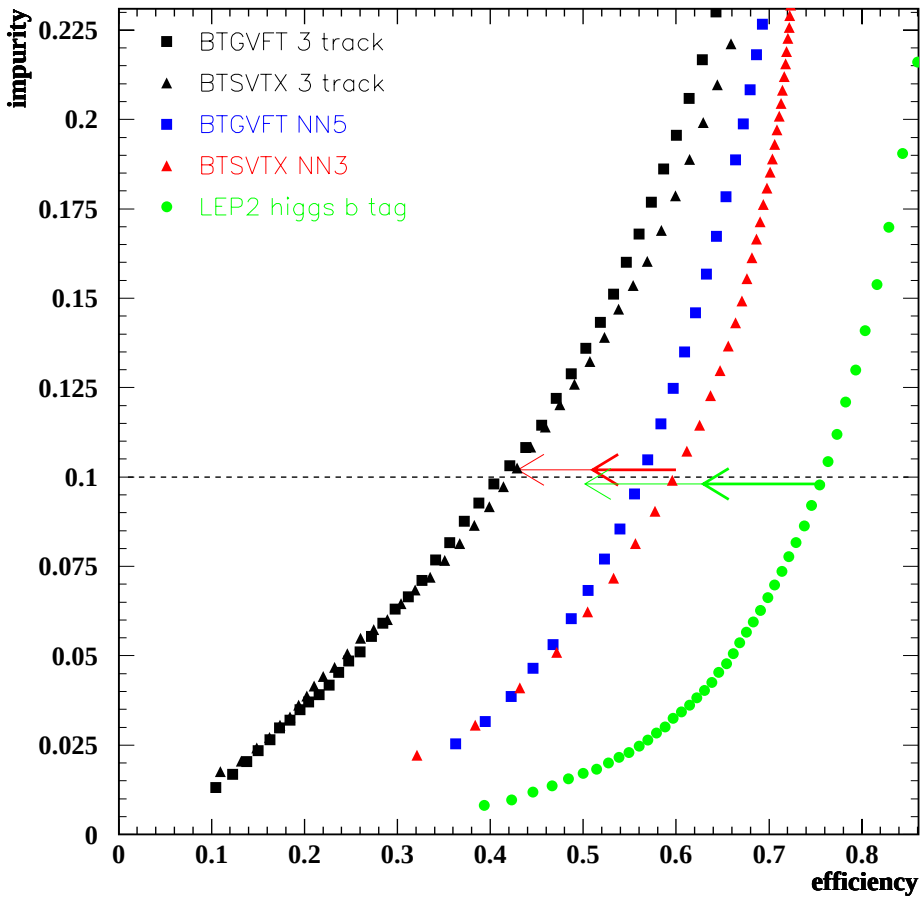

Figure 5.2: *Impurity versus efficiency for different* b*-tagging algorithms.* BTGVFT *(3 track) and* BTSVTX *(3 track) are secondary vertex finders based on a simple cut selection. The vertex finders* BTGVFT (NN5) *and* BTSVTX (NN3) *are neural networks using similar input information. The* LEP2 b*-tagger is described in Section 5.2.1. Further details are given in the text.*

via the critical track discriminant described in Section 5.2.1. Figure 5.2 shows the impurity-efficiency curves for all described b-taggers in comparison with the LEP2 b-tagger. All efficiencies presented in Figure 5.2 are calculated with respect to the selection of hadronic decays described in Section 5.1.

Figure 5.2 gives a clear ordering of the different b-taggers according to their impurity-efficiency performance. Yet not for all analyses this is the ultimate criterion. For the reconstruction of excited B mesons, the mass resolution of the excited state plays an important role, too. Using inclusive b hadron reconstruction methods the mass resolution is in general dominated by the b hadron direction resolution. It turns out that the b direction resolution of jets tagged with e.g. BTSVTX (3 track) is better than for BTSVTX (NN3). To achieve the same direction resolution, additional selection criteria have to be applied on the BTSVTX (NN3) sample. The loss in statistics reduces for a given impurity of 10% the efficiency by more than 15% as indicated by the thin red arrow in Figure 5.2. Therefore, if good b direction resolution is mandatory, the neural network taggers are not superior to the cut based vertex finders. For the LEP2 b-tagger, a similar efficiency reduction is observed (green arrow) but still the efficiency is the highest of all described b-taggers. For the analyses presented in this work, a moderate b hadron direction resolution is appropriate, corresponding to a moderate loss in efficiency indicated by the thick arrows in Figure 5.2.

If systematic errors play an important role, b-taggers with a high complexity are disfavoured. For a high precision analysis such as the measurement of R_{b}, systematic uncertainties like mistagging efficiencies and hemisphere correlations have to be determined very carefully. Therefore the BTGVFT approach is superior to the LEP2 b-tagger in this case. For the analyses presented in this work, the total b-tag efficiency is required to be as high as possible while the error on the efficiency is not important (as long as it doesn't spoil the choice of the b-tagger with highest efficiency). The efficiencies obtained from the simulation have been verified from identified $Z^0 \to b\bar{b}$ events using the double tagging method described in [93]. The observed deviations bring about a relative error on the efficiency of the LEP2 b-tagger of 2-5%, depending on the impurity-efficiency working point [94]. For the reconstruction of excited B mesons no hemisphere correlations have to be considered and the non-b background has to be determined with a precision of only about 10%. Thus the LEP2 b-tagger is the best tool available for this work. Events selected with the LEP2 b-tagger are shown in Appendix A.

Chapter 6

Selection and Reconstruction of B Mesons

B mesons are reconstructed using an extended version of a method developed in earlier OPAL analyses [95, 56]. The ultimate goal is the reconstruction of the B meson four-momentum. Since the reconstructed B mesons are used to form excited B meson states such as B^*, B_J^* and $B^{(*)\prime}$, the B reconstruction is tuned to minimise the uncertainties on the B direction and energy, while maintaining a high reconstruction efficiency.

For the reconstruction of b hadrons, the primary event vertex is reconstructed using the charged tracks in the event constrained to the average position and effective spread of the e^+e^- collision point. Charged tracks and electromagnetic calorimeter clusters with no associated track are combined into jets using a cone algorithm [96] with a cone half-angle of 0.65 rad and a minimum jet energy of 5.0 GeV [1]. The two most energetic jets of each event are assumed to contain the b hadrons and the energy and direction of each of the two b hadron candidates is reconstructed. In each hemisphere defined by the jet axis, a weight is assigned to each track and each cluster, where the weight corresponds to the probability that any one track or cluster is a product of the b hadron decay. The b hadron is reconstructed by summing the weighted momenta of the tracks and clusters. The reconstruction algorithm works for all b hadron species and is 100% efficient. Since the major part of this work aims at the reconstruction of $B_{u,d}$ mesons which make up about 80% of the b hadron sample, b hadron candidates are referred to as B mesons in the following. Details of the reconstruction method are provided below. More technical information can be found in [97].

6.1 Calculation of track weights

Two different types of weights are assigned to each charged track:

[1] The cone jet finder provides the best b hadron energy and direction resolution compared to other jet finders.

- $\omega_{\rm vtx}$, calculated from the impact parameter significances of the track with respect to both the primary and secondary vertices;

- $\omega_{\rm NN}$, the output of a neural network based on kinematics and track impact parameters with respect to the primary vertex.

The calculation of $\omega_{\rm vtx}$ requires the existence of a secondary vertex, whereas $\omega_{\rm NN}$ does not and is therefore available for all tracks.

Each jet is searched for secondary vertices using a vertexing algorithm similar to that described in [56], making use of the tracking information in both the $r-\phi$ and $r-z$ planes if available. If a secondary vertex is found, the primary vertex is re-fitted excluding the tracks assigned to the secondary vertex. Secondary vertex candidates are accepted and called 'good' secondary vertices if they contain at least three tracks and have a decay length > 0.2 mm. If there is more than one good secondary vertex attached to a jet, the vertex with the largest number of significant[2] tracks is taken. If there is a tie, the secondary vertex with the larger separation significance with respect to the primary vertex is taken. If a good secondary vertex is determined, a weight is calculated for each track in the hemisphere of the jet using the impact parameter significance of the track with respect to both the primary and secondary vertices. This weight is given by

$$\omega_{\rm vtx} = \frac{R(b/\eta)}{R(b/\eta) + R(d/\sigma)} \,, \tag{6.1}$$

where b and η are the impact parameter and its error with respect to the secondary vertex, and d and σ are the same quantities with respect to the primary vertex. R is a symmetric function describing the impact parameter significance distribution with respect to a fitted vertex. The $\omega_{\rm vtx}$ distribution for tracks of hemispheres with a good secondary vertex is shown in Figure 6.1a and compared with the corresponding Monte Carlo distribution. The weight $\omega_{\rm vtx}$ shows a weak correlation with the momentum of the track.

For each track, the weight $\omega_{\rm NN}$ is calculated using an artificial neural network [98] trained to discriminate b hadron decay products from fragmentation tracks in a jet. The neural network was trained using as inputs the scaled track momentum $x_p = p/E_{\rm beam}$, the track rapidity relative to the estimated B direction, the impact parameters of the track with respect to the primary vertex in the $r-\phi$ and $r-z$ planes and the corresponding errors on the impact parameters [93]. As a preliminary estimate, the jet axis is taken as the estimated B direction. The $\omega_{\rm NN}$ distribution is shown in Figure 6.1b. If a good secondary vertex exists, the track weight $\omega_{\rm NN}$ is combined with the vertex weight $\omega_{\rm vtx}$ using the prescription

$$\omega_{\rm tr} = \frac{\omega_{\rm NN} \cdot \omega_{\rm vtx}}{(1-\omega_{\rm NN}) \cdot (1-\omega_{\rm vtx}) + \omega_{\rm NN} \cdot \omega_{\rm vtx}} \,. \tag{6.2}$$

[2] A track is called significant, if its impact parameter significance with respect to the primary vertex is larger than 2.5.

The weight ω_{tr} in Equation 6.2 comes close to a true probability and provides a separation power as good as the probability obtained from the combination of ω_{NN} and ω_{vtx} under the assumption that the two weights are uncorrelated and uniformly distributed. In the case where there is no good secondary vertex in the jet, the total track weight ω_{tr} is simply given by $\omega_{\mathrm{tr}} = \omega_{\mathrm{NN}}$. The combined weight ω_{tr} for tracks of all hemispheres is shown in Figure 6.1c.

6.2 Calculation of cluster weights

Weights ω_{ecl} and ω_{hcl} are assigned to each electromagnetic and hadronic cluster in the hemisphere of the B meson based on their rapidity with respect to the estimated B direction. The weight is taken from the B meson decay product purity, obtained from a parameterisation of the corresponding Monte Carlo as a function of the cluster energy. Clusters associated with a charged track have the estimated energy of the track subtracted.

6.3 Calculation of B direction

The B momentum is calculated iteratively by a weighted sum of all tracks and clusters in the hemisphere:

$$\vec{p} = \sum_{i=1}^{N_{\mathrm{track}}} \omega_{\mathrm{tr},i} \cdot \vec{p}_i + \sum_{i=1}^{N_{\mathrm{ecal}}} \omega_{\mathrm{ecl},i} \cdot \vec{p}_i + \sum_{i=1}^{N_{\mathrm{hcal}}} \omega_{\mathrm{hcl},i} \cdot \vec{p}_i \tag{6.3}$$

where N_{track}, N_{ecal} and N_{hcal} denote the number of tracks, number of electromagnetic clusters and number of hadronic clusters, respectively. The rapidity calculation, for both tracks and clusters, is performed relative to an estimate of the B meson direction. The initial input for this axis is the jet direction calculated using tracks and unassociated electromagnetic clusters. The weights are then recalculated with the rapidity determined using the new B direction estimate.

If a good secondary vertex exists in a jet, the axis defined by the primary and secondary vertices yields additional direction information besides the B direction estimate obtained from the weighted momentum sum of tracks and clusters. To make optimal use of the two direction estimators available for a B candidate, the uncertainty of each direction estimator has to be calculated. The covariance matrices of the primary and secondary vertices determine the error on the B flight direction. The error on the momentum sum is estimated by removing each term in turn from the sum in Equation 6.3, calculating the change in the B direction caused by this omission and adding up in quadrature the corresponding error contributions from each track and cluster. The final estimate of the B direction is obtained by taking the error-weighted sum of the B direction calculated with the momentum sum method and the B direction obtained from the primary and secondary vertex positions. The direction information in the $r - z$ plane of the

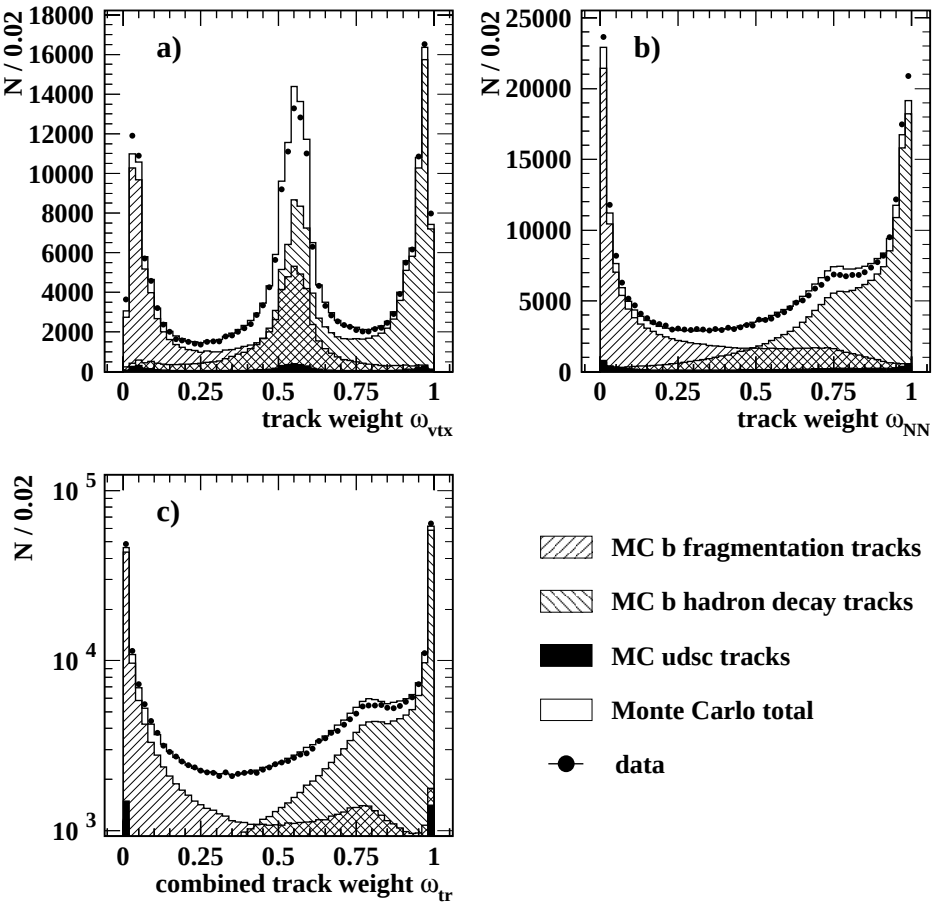

Figure 6.1: *a) The track weight* ω_{vtx} *for all tracks in hemispheres with a good secondary vertex. The peaks near 0 and 1 correspond to tracks created by* b *fragmentation and* b *hadron decay tracks, respectively. The peak near 0.5 is produced by tracks which are not unambiguously assigned to the primary or the secondary vertex, as in the case of tracks matching both the primary and secondary vertex or matching no vertex at all. b) The track weight* ω_{NN} *for tracks of all hemispheres (with or without a good secondary vertex). The separation power of* ω_{NN} *is superior to the separation power of* ω_{vtx}*. c) The combined track weight* ω_{tr} *calculated from* ω_{vtx} *and* ω_{NN} *for tracks of all hemispheres. Note that* ω_{tr} *is shown on a logarithmic scale.*

secondary vertex is only used if the vertex is built with tracks that give rise to at least four hits in the z-layers of the silicon microvertex detector (the maximum number of these hits per track is two).

The error $\Delta\alpha$ on the weighted sum of both B direction estimators described in the previous paragraph is a measure for the quality of the B direction[3]. To improve the resolution on the B direction, which in turn dominates the Bπ mass resolution, a cut on $\Delta\alpha$ is imposed. Since the main goal of this analysis is a separation of some of the B_J^* states by reconstructing different B_J^* decay channels rather than obtaining a very good Bπ mass resolution, the cut $\Delta\alpha < 0.035$ is rather loose. This cut removes the 20% of the B candidates with the poorest direction resolution, mainly those with no associated good secondary vertex.

6.4 Calculation of B energy

The B meson energy is calculated in analogy to the B momentum in Equation 6.3, where $\vec{p}_i$ is replaced by $E_i = \sqrt{\vec{p}_i^{\,2} + m_i^2}$ with $m_i = m_{\pi^\pm}$ for tracks and $m_i = 0$ for clusters. The weights are calculated using the B direction as determined in the previous section. The resolution on the total energy of the B candidate can be significantly improved by constraining the total centre-of-mass energy, E_{CM}, to twice the LEP beam energy. Assuming a two-body decay of the Z^0, one obtains

$$E_{\mathrm{B}} = \frac{E_{\mathrm{CM}}^2 - M_{\mathrm{recoil}}^2 + M_{\mathrm{B}}^2}{2E_{\mathrm{CM}}} \,, \tag{6.4}$$

where the mass of the b hadron is set to the B meson mass $M_{\mathrm{B}} = 5.279$ GeV/c^2 and M_{recoil} denotes the mass recoiling against the B meson. The recoil mass and the recoil energy E_{recoil} are calculated by summing over all tracks and clusters[4] of the event weighted by $(1 - \omega_i)$ and assuming the particle masses used in the calculation of E_i. To account for the amount of undetected energy mainly due to the presence of neutrinos, the recoil mass is scaled by the ratio of the expected energy in the recoil to the energy actually measured:

$$M_{\mathrm{recoil,new}} = M_{\mathrm{recoil,old}} \cdot \frac{E_{\mathrm{CM}} - E_{\mathrm{B}}}{E_{\mathrm{recoil}}} \tag{6.5}$$

where E_{B} is taken from Equation 6.4. The new recoil mass value $M_{\mathrm{recoil,new}}$ obtained from Equation 6.5 is substituted into Equation 6.4 and the calculation of E_{B} is iterated. After two iterations the uncertainty on the B meson energy is minimised. A minimum B energy of 15 GeV is required to further improve the energy resolution removing only a few percent of the selected B candidates.

[3] In the case where no good secondary vertex exists, $\Delta\alpha$ is simply given by the uncertainty on the momentum sum.

[4] Tracks and clusters not contained in the hemisphere of the B meson candidate have weights $\omega_i = 0$. ω_i denotes the weight $\omega_{\mathrm{tr},i}$, $\omega_{\mathrm{ecl},i}$ and $\omega_{\mathrm{hcl},i}$ for tracks, electromagnetic clusters and hadronic clusters, respectively.

The distribution of the difference between the reconstructed and generated ϕ angle of simulated B mesons can be described by a fit to two Gaussians. The standard deviation of the narrower Gaussian is 14.2 mrad and 88% of the entries lie within 3σ. The corresponding quantities describing the θ resolution are $\sigma = 15.0$ mrad and 89%, respectively. The narrower Gaussian from a two Gaussian fit to the difference between the reconstructed and generated B meson energy has $\sigma = 2.3$ GeV, and 86% of the entries are contained within 3σ. The corresponding Monte Carlo resolution histograms are shown in Figure 6.2. The asymmetry in the B energy resolution is a direct consequence of the applied beam constraint and the fact that the B meson carries most of the energy of a jet.

The complete B meson selection applied to the full data sample results in 574 288 tagged jets with a b purity of about 96%, as estimated from Monte Carlo. About 75% of the selected jets contain a good secondary vertex.

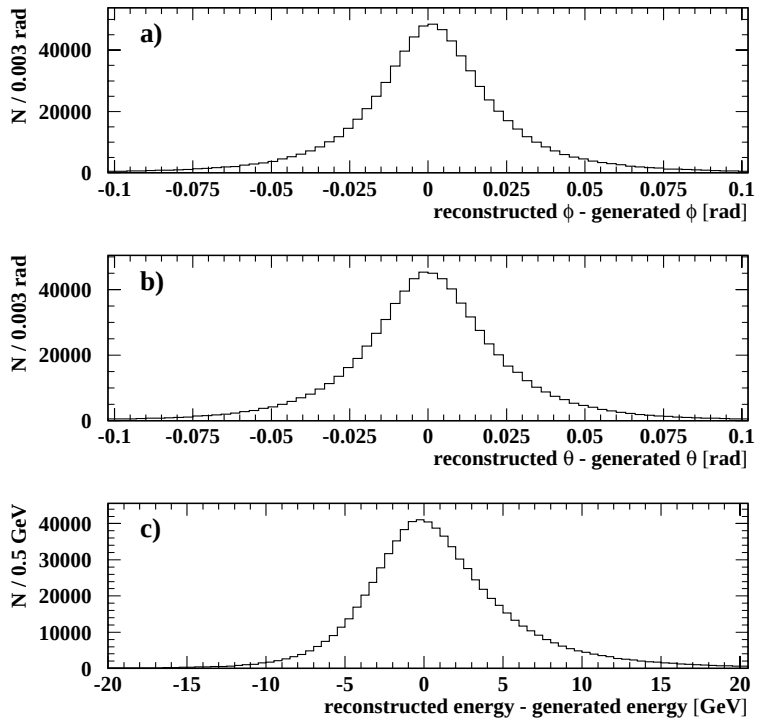

Figure 6.2: *Angular and energy resolution of inclusively reconstructed* B *mesons obtained from Monte Carlo. a) The difference of the reconstructed and the generated ϕ angle of the* B *meson direction. b) The difference of the reconstructed and the generated θ angle of the* B *meson direction. c) The difference of the reconstructed and the generated* B *meson energy.*

Chapter 7

Analysis of B* Mesons

In this chapter the reconstruction of the vector meson partners of the B ground states is presented. The focus of this work on B^* mesons[1] is twofold: 1. the development of a high statistics B^* tag for the analysis of B_J^* mesons decaying into B^* and B; 2. the investigation of an improved B^* measurement and the feasibility study of a separate B_s^* measurement with OPAL data.

To reconstruct B^* mesons, both the B meson and the photon have to be identified. In this chapter two methods of tagging the photon are developed. To efficiently select photons from B^* decays, it is important to have a detailed knowledge of their properties. The photon produced in the decay $B^* \to B\gamma$ has an energy of about 46 MeV in the rest frame of the B^*. The mean energy of the photon in the laboratory frame is approximately 350 MeV, with a maximum energy below 800 MeV. Due to the kinematics of the process, these photons are produced predominantly in the core of the jet. The high particle density in this region gives rise to a high background level when identifying the photon. Since a high B^* reconstruction efficiency is crucial for the main part of this analysis, photons are reconstructed in two ways: from energy deposits in the electromagnetic calorimeter and from converted photons in the tracking volume. The conversion probability within the OPAL tracking system for photons coming from the decay $B^* \to B\gamma$ is approximately 8%.

Section 7.1 describes a new conversion finder developed for photons with energies below 1 GeV. Section 7.2 summarises the detection of photons in the electromagnetic calorimeter in the same energy range. The reconstruction of B^* mesons is presented in Section 7.3. Section 7.4 describes the construction of a B^* probability attached to each B meson. The feasibility of new B^* and B_s^* measurements with OPAL data is discussed in Section 7.5.

[1] If not stated otherwise, B^* denotes B^{*0}, $B^{*\pm}$ and B_s^* mesons.

7.1 Reconstruction of photon conversions

The reconstruction of converted photons used in this analysis is optimised for the low energy region. The selection algorithm is partially based on quantities that have been used in earlier analyses [99, 100, 101, 102] but tuned to obtain high efficiency rather than very good angular and momentum resolution. Given the low energy carried by these photons, calorimetry information is ignored and only tracking information is used for the reconstruction of converted photons. The most important applications for this conversion finder are $B^* \to B\gamma$, $\Sigma^0 \to \Lambda\gamma$ and $\Sigma_b^{(*)} \to \Lambda_b\gamma$ decays[2].

Tracks with a total momentum p below 1.0 GeV/c, opposite charge and a measured dE/dx within three standard deviations of the expected value for electrons are combined into pairs. For each pair, the track with the greater scalar momentum is required to have a transverse momentum $p_t > 50$ MeV/c with respect to the beam axis and at least 20 hits out of a possible 159 per jet chamber sector. For the track with lower momentum a minimum p_t of 20 MeV/c is required. The asymmetric selection cuts for the two tracks in a pair guarantee at least one well measured track and reflect the fact that the electron and the positron of a converted photon tend to have different momenta in the laboratory frame. To suppress random track combinations, the distance of closest approach between the two tracks of a pair in the $r-\phi$ plane has to be smaller than 1.0 cm with an opening angle between the tracks at their point of closest approach smaller than 1.0 rad.

In order to make optimal use of all the available information, the following physical quantities of each conversion track pair candidate are fed into a neural network:

- the distance of closest approach between the two tracks in the $r-\phi$ plane;
- the radial distance with respect to the z axis of the first and last measured hit in the inner tracking chambers for each track;
- the radial distance with respect to the z axis of the common vertex[3] of both tracks obtained from a fit in the $r-\phi$ plane;
- the impact parameter with respect to the primary vertex in the $r-\phi$ plane of the reconstructed photon;
- the invariant mass of the track pair assuming both tracks to be electrons;
- the transverse momentum relative to the z axis of the lower momentum track.

[2] The $\Sigma_b^{(*)}$ decays radiatively if $M(\Sigma_b^{(*)}) < M(\Lambda_b) + M(\pi)$.

[3] The z position of this vertex is fitted independently and the reconstructed photon vector is constrained to the z coordinate of the primary vertex to improve the accuracy of the θ determination.

The resulting neural network output is shown in Figure 7.1 with the Monte Carlo normalised to the same number of hadronic Z^0 decays as observed in the data. The separation power of the neural network is high. A comparison with the simulation shows that the Monte Carlo background of random track combinations is overestimated. In the region of the $\gamma \to e^+e^-$ signal, the agreement between data and Monte Carlo is good. Figure 7.2 shows the radial distance of the vertex position of conversions after a tight cut on the neural network output. The observed structure at low radii demonstrates the different material densities due to the technical design of the inner tracking system. A few subtleties of the conversion finder are worthy of mention:

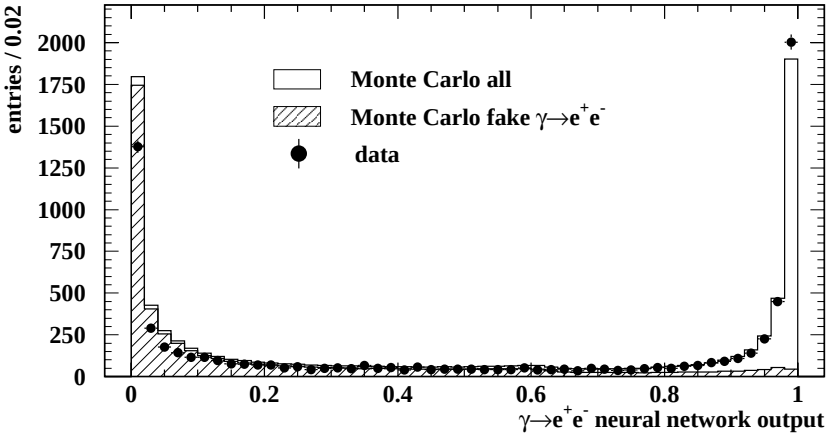

Figure 7.1: *Output distribution of the neural network conversion finder. The Monte Carlo distribution (open histogram) is normalised to the same number of* $Z^0 \to q\overline{q}$ *decays observed in data (dots with error bars). The fraction of fake conversions is slightly overestimated in the simulation (hatched histogram).*

- Since the selection criteria for the low momentum track are very loose, the conversion finder is a hybrid of a double and a single arm conversion finder.
- All combinations of electron track candidates of the same event are ordered according to the neural network output. The pair with the highest neural network output is considered as the best conversion pair candidate and removed from the list of track pairs. From the remaining list, again the track pair with the highest output is selected as the second best conversion pair candidate. This procedure is iterated until no more track pairs are left in the event. This method provides an optimisation of the reconstruction efficiency and reduces the fraction of wrong track pair combinations.

- The conversion finder does not rely on any particle identification except for the loose $\mathrm{d}E/\mathrm{d}x$ requirements. Calorimeter information is not used at all. Several studies indicated that the use of variables which are not based on tracking information does not improve the conversion tagging performance for low energetic photons. This is of particular interest since most of the problems concerning systematic uncertainties [103] can be avoided by discarding detailed $\mathrm{d}E/\mathrm{d}x$ and calorimeter information.

- The minimal transverse momentum of 50 MeV/c (20 MeV/c) for the high (low) momentum track of a conversion candidate allows a curling of the electron candidate track within the tracking system. A nice example of an event with two electron track helices produced by a converted photon is presented in Figure A.4 in Appendix A. Note that in this example the conversion finder automatically picks up the correct track pair from the abundant number of combinations.

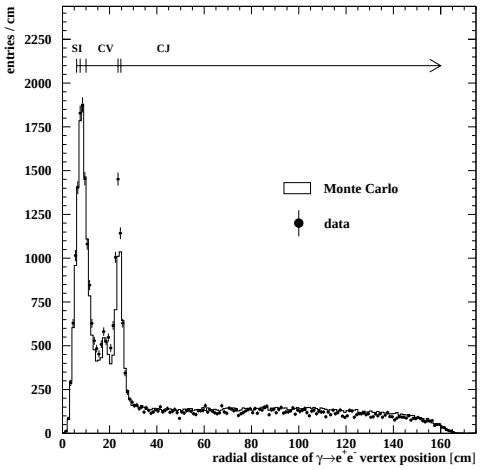

Figure 7.2: *Distribution of the radial vertex position of conversions. The spikes at low radii reflect the large material density of the silicon detector, the outer beam pipe, CV and CJ.*

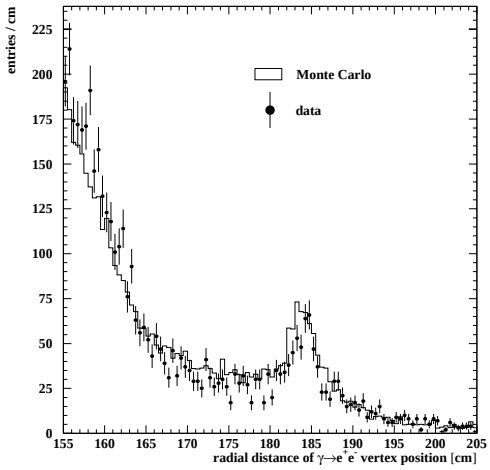

Figure 7.3: *Close-up view of the distribution of the radial vertex position of conversions near the outer CJ shell. The peak around 185 cm is explained in the text.*

- The conversion finder is an all-round tagger in the low energy regime. Even conversions emerging from π^0 produced in nuclear interactions of hadrons with the material of the tracking system and back-scattered into the jet chamber are reconstructed. The corresponding signal is shown in Figure 7.3 and quite well described by the simulation. Example event displays are given in Figures A.5 and A.6. Such candidates can be removed by the requirement

of a high neural network output. The impact parameter with respect to the primary vertex in the $r - \phi$ plane of the reconstructed photon treats such conversions as background events. Therefore, the peak of Figure 7.3 is not visible in Figure 7.2 as the distribution of the latter is shown after a cut on the neural network output has been applied.

In the following the special selection requirements for conversions from $B^* \to B\gamma$ decays are discussed. All conversion candidates with a neural net output greater than 0.7 and a photon energy below 1.5 GeV are called 'good' conversion candidates for a given B meson candidate if the opening angle between the reconstructed B momentum vector and the reconstructed photon momentum vector is smaller than 90°. At this stage, an average of 0.82 good conversion candi-

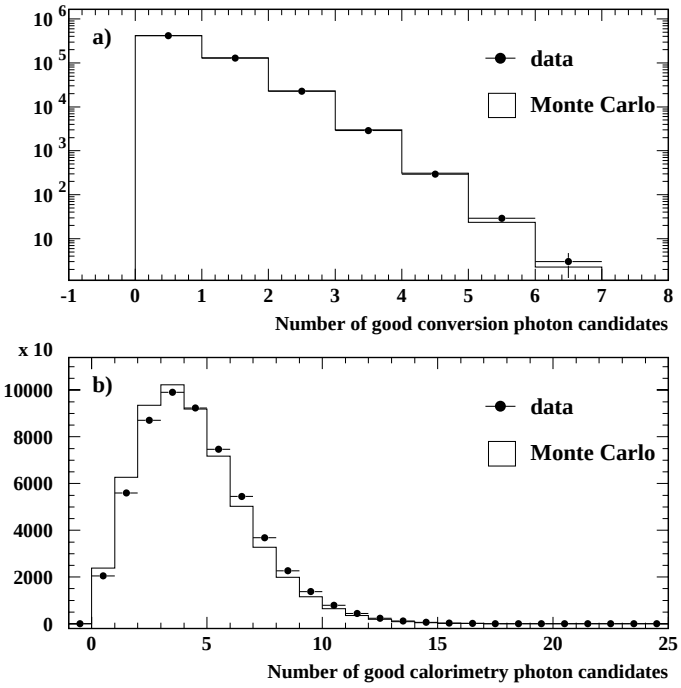

Figure 7.4: *a) The number of good conversion photon candidates per* B *candidate observed in data and Monte Carlo. b) The number of good calorimeter photon candidates per* B *candidate observed in data and Monte Carlo. For the analysis, the Monte Carlo distribution of the latter is reweighted to the data distribution.*

dates are selected per B candidate in both data and Monte Carlo. The candidate multiplicity distributions are shown in Figure 7.4a. The total efficiency to detect photons from the decay $B^* \to B\gamma$ with the conversion algorithm is estimated from simulation to be $(2.70 \pm 0.01_{\text{stat}})\%$. The efficiency is rather independent of the photon energy from 1.0 GeV down to 200 MeV where it rapidly drops to zero due

to track selection requirements. The amount of fake conversions in the selected sample is estimated from Monte Carlo simulation to be $(11.75 \pm 0.04_{\mathrm{stat}})\%$.

Fits to the difference between the reconstructed and generated photon energy in Monte Carlo are made using the sum of two Gaussians, both constrained to the same mean value. The narrower Gaussian has a standard deviation of 5 MeV at energies of 200 MeV up to 13 MeV at energies of 750 MeV and about 70% of the entries are contained within 3σ. Similar fits to the ϕ and θ resolutions give values of 3.4 mrad (70%) and 5.4 mrad (61%), respectively.

7.2 Reconstruction of photons in the electromagnetic calorimeter

Photons are also detected as showers in the barrel region of the electromagnetic calorimeter. The location and energy of these showers are obtained from a fit to the energy deposits in the individual lead glass blocks not associated with any charged track. The whole reconstruction method has been shown to work in the dense environment of hadronic jets down to photon energies as low as 150 MeV. The details of the reconstruction are described in [104].

Showers in the electromagnetic calorimeter are accepted as photon candidates if they have an energy in the range 200 MeV to 850 MeV and a photon probability $P_\gamma > 0.20$, where P_γ is the output of a simplified neural network [104]. If the opening angle between such a shower and a reconstructed B candidate is less than 90°, this shower is considered a 'good' photon candidate for the corresponding B candidate. On average, there are 4.59 (4.38) good calorimeter photon candidates per B candidate selected in the data (Monte Carlo) sample. To correct for the observed discrepancy, the Monte Carlo is reweighted bin-by-bin to the data distribution shown in Figure 7.4b. The efficiency to detect a photon from the decay $\mathrm{B}^* \to \mathrm{B}\gamma$ in the electromagnetic calorimeter is estimated to be $(14.52 \pm 0.03_{\mathrm{stat}})\%$ using Monte Carlo simulated events. The fraction of fake photons arising from charged tracks and neutral hadrons in the sample ranges from 32% at photon energies of 850 MeV up to 43% at photon energies of 200 MeV. If compared with the selected conversion sample, the selection of $\mathrm{B}^* \to \mathrm{B}\gamma$ photons in the electromagnetic calorimeter has a much higher efficiency but lower purity.

As with the converted photons, the energy resolution has been determined from Monte Carlo simulation using a double Gaussian fit. The narrower Gaussian has a width of 20 MeV at photon energies of 250 MeV and increases up to 86 MeV at energies of 800 MeV, and about 75% of the entries are contained within 3σ. Similar fits to the ϕ and θ resolutions give values of 3.6 mrad (65%) and 3.6 mrad (72%), respectively. In contrast to the conversion sample, photons reconstructed in the electromagnetic calorimeter have much higher energy uncertainties, but the θ resolution in particular is better.

7.3 Reconstruction of B* → Bγ decays

Each reconstructed B meson candidate is combined with all good conversion and calorimeter candidates to reconstruct B* candidates. The invariant mass of a Bγ combination is defined as

$$M_{\mathrm{B}\gamma} = \sqrt{M_{\mathrm{B}}^2 + 2E_{\mathrm{B}}E_{\gamma} - 2p_{\mathrm{B}}p_{\gamma}\cos\alpha} \quad , \tag{7.1}$$

where M_{B} is 5.279 GeV/c^2 and α is the measured angle between the B meson and the photon candidate. A good approximation of Formula 7.1 is $M_{\mathrm{B}\gamma} = E_{\gamma}\gamma_{\mathrm{B}}(1 - \beta_{\mathrm{B}}\cos\alpha)$, where γ_{B} and β_{B} are the Lorentz factors of the B meson. The mass difference $\Delta M = M_{\mathrm{B}\gamma} - M_{\mathrm{B}}$ between the B* candidate and the B is calculated by simply subtracting the nominal B mass of $M_{\mathrm{B}} = 5.279$ GeV/c^2 from $M_{\mathrm{B}\gamma}$.

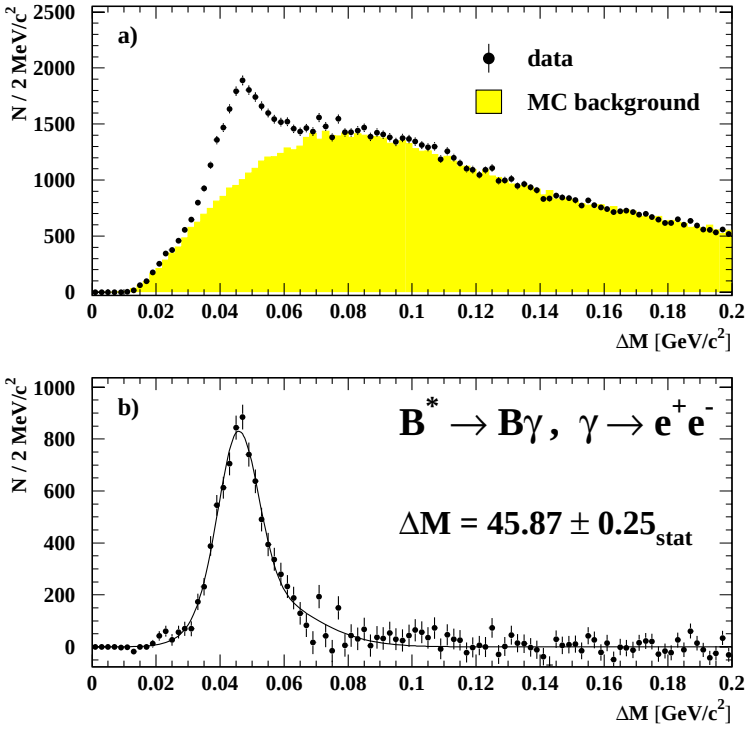

Figure 7.5: *a) The $\Delta M = M_{\mathrm{B}\gamma} - M_{\mathrm{B}}$ mass distribution of the conversion photon sample. The background is estimated from Monte Carlo simulation and normalised to the data distribution in the sideband region* 0.09 GeV/$c^2 < \Delta M <$ 0.20 GeV/c^2. *b) The corresponding background subtracted signal. The fit function used for the signal is described in the text.*

The mass difference distributions of the conversion sample observed in the data and the corresponding Monte Carlo background are shown in Figure 7.5a. The

background is normalised to the data in the sideband region 0.09 GeV/c^2 < ΔM < 0.20 GeV/c^2. The background subtracted signal of Figure 7.5b is fitted to the sum of two Gaussians fixed to the same mean, where one of the Gaussians is allowed to have asymmetric width. The observed asymmetry of the mass resolution of the conversion sample is well simulated in the Monte Carlo and is due to the very loose track requirements of the lower momentum track of the conversion pair. A mass difference of $\Delta M = (45.87 \pm 0.25_{\mathrm{stat}})$ MeV/c^2 is obtained from the fit to the data, where the error is statistical only. This result agrees well with the current world average value of (45.78 ± 0.35) MeV/c^2 [26].

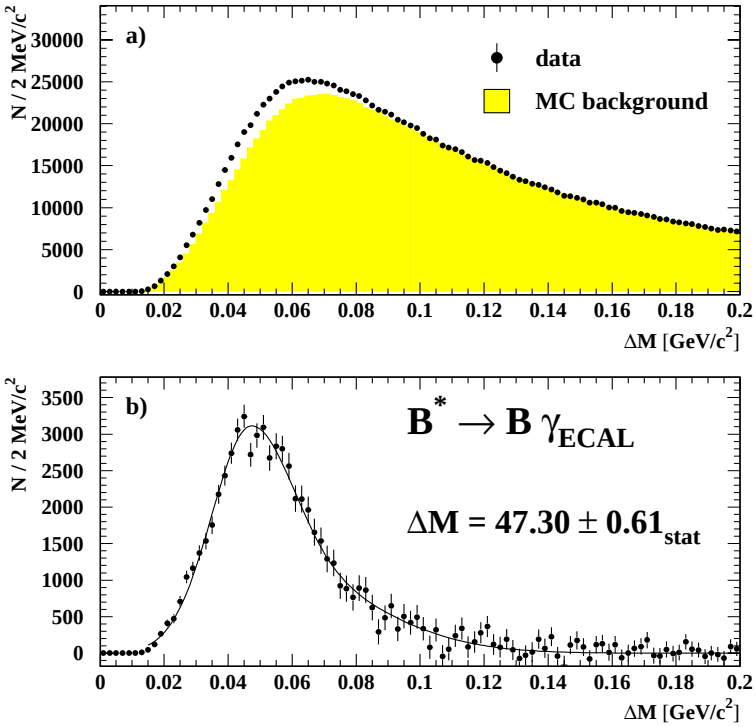

Figure 7.6: *a) The $\Delta M = M_{\mathrm{B}\gamma} - M_{\mathrm{B}}$ mass distribution of photons reconstructed in the electromagnetic calorimeter. The background is estimated from the Monte Carlo simulation and normalised to the data distribution in the sideband region* 0.10 GeV/c^2 < ΔM < 0.20 GeV/c^2. *Although the resolution is poor compared to the conversion photon sample, an excess of entries in the data distribution around* 46 MeV/c^2 *is clearly visible. b) The corresponding background subtracted signal. The fit function is described in the text.*

The ΔM distribution using calorimeter photons is shown in Figure 7.6a. The background is taken from Monte Carlo simulation and normalised to the data in the sideband region 0.10 GeV/c^2 < ΔM < 0.20 GeV/c^2. The same fit function

as for the photon conversion sample is used to obtain the mass difference ΔM from the background subtracted signal distribution in Figure 7.6b. A value of $(47.30 \pm 0.61_{\mathrm{stat}})$ MeV/c^2 is obtained from this fit, which is consistent within two sigma with the result from the fit to the conversion signal.

For the B* sample reconstructed with photon conversions, the mass resolution is dominated by the uncertainty on the reconstructed B direction. For the calorimeter photon sample, the B* mass resolution suffers in addition from the energy resolution of the calorimeter. Due to the high background of fake photons and the moderate energy resolution at low photon energies, the signal-to-background ratio is rather poor for calorimeter photons. Therefore, uncertainties in the B* reconstruction using these photons are dominated by systematic errors on the background shape and energy calibration. All systematic uncertainties arising from the B* reconstruction will be discussed in Chapter 11.

7.4 The B* weight $\mathcal{W}(\mathrm{B}^*)$

To select samples enhanced and depleted in B* mesons, a B* weight is assigned to each B candidate. This weight combines information from both conversion and calorimeter photon candidates and represents the probability that a B candidate is the true daughter of a B* meson. Only the best conversion and best calorimeter candidate assigned to any one B candidate are considered in the calculation of this weight, where the best candidate is defined as that which gives $\Delta M = M_{\mathrm{B}\gamma} - M_{\mathrm{B}}$ closest to the world average of 45.78 MeV/c^2 [26].

The weight is constructed by parametrising the purity of the mass difference distribution in several variables in Monte Carlo data. For calorimeter photon candidates, this parametrisation is performed as a function of the photon probability, P_γ (see Section 7.2), and the total number of good calorimeter candidates found per B candidate. For each B candidate, a single weight is calculated by taking the simple mean of the weight resulting from each of the above parametrisations.

Similarly, for conversion photon candidates, the parametrisation is performed in ΔM as a function of the total number of conversion candidates, and a weight is extracted as for the calorimeter candidates. The two weights obtained from conversion and calorimeter photons are combined by taking their mean.

The resulting weight $\mathcal{W}(\mathrm{B}^*)$ is shown in Figure 7.7a for Monte Carlo and data, and the contributions from jets containing a B* and jets containing no B* as seen in the simulation are shown. The primary features of the $\mathcal{W}(\mathrm{B}^*)$ distribution are:

- a peak at $\mathcal{W}(\mathrm{B}^*) = 0.625$, corresponding to B candidates with no associated good conversion or calorimeter photon candidate;

- a peak at $\mathcal{W}(\mathrm{B}^*) = 0.632$, containing B candidates with no good conversion candidate and a best calorimeter candidate having a Bγ mass far away from the nominal B* mass;

- a peak around $\mathcal{W}(\mathrm{B}^*) = 0.656$, containing B candidates with the best calorimeter candidate close to the nominal B^* mass;
- a peak at $\mathcal{W}(\mathrm{B}^*) = 0.715$, containing B candidates with the best calorimeter candidate being close to the nominal B^* mass and having a high photon probability P_γ;
- the tail towards high B^* probabilities is made up by best conversion candidates very close to the nominal B^* mass.

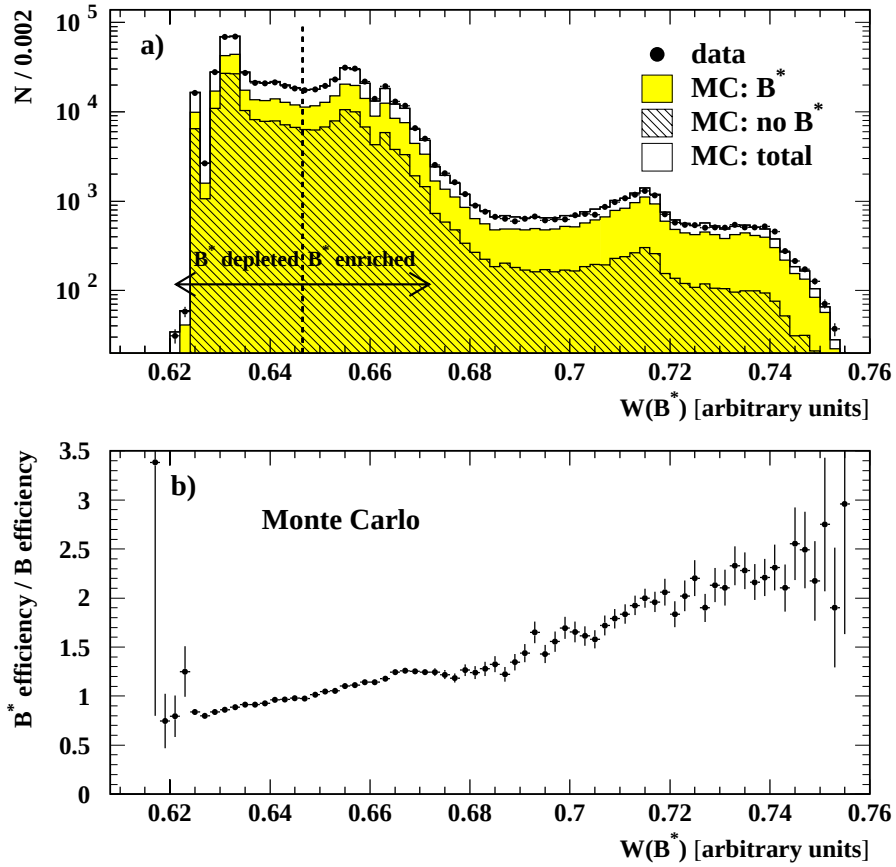

Figure 7.7: *a) The* $\mathcal{W}(\mathrm{B}^*)$ *distribution for data with the corresponding Monte Carlo histograms indicating the number of* B *candidates with a* B^* *parent and no* B^* *parent. The dotted line gives the boundary between the* B^**-enriched and* B^**-depleted samples. b) The ratio of the efficiency to reconstruct a* B *meson with a* B^* *parent over the efficiency to reconstruct a* B *meson without a* B^* *parent versus the weight* $\mathcal{W}(\mathrm{B}^*)$ *calculated from simulated data.*

The assignment of the specific photon candidate samples to the peaks and to the tail of the $\mathcal{W}(\mathrm{B}^*)$ distribution is based on Monte Carlo information. Figure 7.7b shows the ratio $\varepsilon(\mathrm{B}^*)/\varepsilon(\mathrm{B})$ versus $\mathcal{W}(\mathrm{B}^*)$. $\varepsilon(\mathrm{B}^*)$ refers to the efficiency to select a B meson from a true $\mathrm{B}^* \to \mathrm{B}\gamma$ decay and $\varepsilon(\mathrm{B})$ is the efficiency to select a B meson which has not come from a B^*. In general, the Monte Carlo simulation of $\mathcal{W}(\mathrm{B}^*)$ describes the data adequately. A comparison of the Monte Carlo and data distributions yields a χ^2 per degree of freedom of 2. A cut on $\mathcal{W}(\mathrm{B}^*)$ allows to produce samples of B candidates with different B^* fractions. Further details and systematic studies concerning $\mathcal{W}(\mathrm{B}^*)$ are given in Chapter 11.

7.5 Outlook

The main goal of the presented B^* analysis is a high statistics selection to improve the B^*/B separation power in B_J^* decays. The implications on B_J^* decays will be discussed later. Due to the high background and the poor mass resolution the B^* analysis using the calorimeter photon sample cannot be used for a competitive B^* measurement. The B^* analysis with converted photons on the other hand has a factor of 3-5 higher efficiency compared to other LEP measurements [105, 106, 54, 107] while the background level and the mass resolution is comparable.

7.5.1 Comparison with other B* analyses

The statistical error on the mass splitting of ± 0.25 MeV/c^2 obtained from the fit to the $\mathrm{B}\gamma$ mass distribution of the conversion sample is smaller than the world average total error of ± 0.35 MeV/c^2. Yet the measurement is expected to be dominated by systematic uncertainties like the published OPAL analysis [105]. The dominating systematic uncertainty of the mass splitting measurement in [105] is the error on the photon energy calibration. The latter was obtained from a data / Monte Carlo comparison of reconstructed π^0 which in turn is limited by statistics. Therefore, also the systematic error on the mass splitting could be improved with the higher statistics given in this analysis. For the production rate the dominant error comes from uncertainties in the shape of the helicity angular distribution. No improvement is expected here in comparison with the published OPAL result. The uncertainties of the helicity distribution measurement may be reduced slightly with higher statistics. Further studies are needed here to shed light on this part of the analysis. In summary, a full B^* analysis performed with the presented reconstruction methods is expected to be competitive in the production rate measurement and the measurement of the helicity angle. The analysis has the potential for the world's most accurate measurement of the B^*/B mass splitting to date.

7.5.2 Comments on B_s^*

A measurement of the B_s^*/B_s mass splitting is a fastidious task. The problem lies in the fact that the background from non-strange B mesons is high for all production mechanisms and the hyperfine splitting is roughly the same for strange and non-strange mesons. The only B_s^* measurement to date was performed at the $\Upsilon(5S)$. The B_s^* signal was separated from the $B_{u,d}^*$ background using the different shape of the corresponding photon energy spectra: $M_{B_s^*} - M_{B_s} = (47.0 \pm 2.6)$ MeV/c^2 [108]. In another analysis of B^* production in Z^0 decays an upper limit on the difference of the strange and non-strange hyperfine splittings of 6 MeV/c^2 is quoted [54]. A similar result could be obtained with the B^* reconstruction presented in this work by tuning the selection on a good mass resolution.

A direct B_s^* measurement requires the reconstruction of specific B_s decay channels. Earlier OPAL measurements of the B_s lifetime exploited the $B_s \to D_s^- \ell^+ \nu_\ell X$ and $B_s \to D_s^- X$ decay channels with fully reconstructed $D_s^- \to \phi\pi, K_S^0 K, K^* K, KK$. In those analyses, 172 ± 28 $B_s \to D_s^- \ell^+ \nu_\ell X$ and 519 ± 136 $B_s \to D_s^- X$ candidates have been found with a $B_{u,d}$ decay background of about 30 and 200 ± 40 respectively. Assuming a vector meson production fraction of 0.75 and a total photon reconstruction efficiency of 2.7%, B_s^* signals of 4 ± 1 and 11 ± 3 are obtained. Even ignoring the background from $B_{u,d}^*$ decays, both signal estimates are not encouraging at all. The other LEP experiments have B_s samples of comparable statistics. Although the B_s statistics will be much higher at future experiments such as LHCb and HERA-B it is unclear whether the reconstruction performance of low energetic photons will allow a direct B_s^* measurement.

Chapter 8

Reconstruction of Orbitally-Excited B Mesons

This chapter examines the reconstruction of orbitally-excited B mesons, B_J^*. By analogy with the B^* analysis, the four-momenta of the decay products of the excited state are reconstructed and its invariant mass is calculated. However, the B_J^* reconstruction comprises several experimental difficulties which are not present in the $B^* \to B\gamma$ analysis:

- According to Sections 2.4.4 and 2.6 one expects four different B_J^* states with different masses and widths. All B_J^* states do most likely overlap in mass[1].
- There are at least two dominant decay modes: $B_J^* \to B^*\pi$ and $B_J^* \to B\pi$.
- The B_J^* production rate is approximately a factor of three smaller compared to the B^* production rate [109].
- The Q-value of the B_J^* decay is much larger compared to the B^* decay.
- The combinatorial background is large. As a consequence, the signal to background ratio is moderate.
- The modelling of the Monte Carlo background, especially the background arising from fragmentation, is not well understood.

The facts listed above define the strategy of this B_J^* analysis. The focus is on a high statistics B_J^* reconstruction and a new method developed to determine the different background sources and their uncertainties directly from data. The next step of the B_J^* analysis is a separation of $B_J^* \to B^*\pi^\pm$ decays from $B_J^* \to B\pi^\pm$ decays and will be presented in Chapter 9. Section 8.1 contains the selection of pion candidates. In Section 8.2 the reconstructed $B\pi$ mass spectrum is described.

[1] This theoretical prediction is strongly supported by a low statistics B_J^* analysis with a very good $B\pi$ mass resolution of $2 - 5$ MeV/c^2 [58].

A fit to this mass spectrum is presented in Section 8.3 and Section 8.4 gives a comparison with other B_J^* measurements.

I start with the basics of the B_J^* selection. All B_J^* candidates, even those expected to decay into $B^*\pi^\pm$, are reconstructed using the measured 4-momenta of the B meson and the pion. B candidates are selected and reconstructed as described in Chapter 6 and combined with charged pion candidates. Pions produced in the decay of a B_J^* will be referred to as 'signal pions'. Since the B_J^* decays strongly, signal pions are expected to be associated to the primary event vertex rather than to a possible secondary vertex. In comparison with other pions created in the fragmentation process, signal pions are expected to have a large longitudinal momentum p_l with respect to the jet axis. These are the basic characteristics used to separate signal pions from B decay products and from fragmentation tracks. A significant number of non-resonant fragmentation pions are expected to be produced near a B meson. The kinematics of these pions is similar to the signal pions, giving rise to a combinatorial background in the invariant mass of $B\pi$ candidates. This background is further enhanced by the inability to unambiguously associate all B decay tracks with the secondary vertex (see e.g. Figure 6.1).

8.1 Pion selection

The signal pion selection for this analysis makes use of techniques employed in [56] and [58]. All charged tracks that are well measured according to a standard track selection [110] are considered as possible signal pion candidates if they belong to the same jet as the B candidate. Additionally, the following selection cuts are applied in the given order:

- The measured ionisation energy loss $\mathrm{d}E/\mathrm{d}x$ has to be consistent with the expected value for pions within 2.6 standard deviations, if $\mathrm{d}E/\mathrm{d}x$ information is available for this track.

- To suppress B decay tracks, the track weight ω_{NN} describing the probability of coming from a B decay (see Section 6.1) has to be smaller than 0.9.

- The B decay track rejection is improved by the requirement $\omega_{\mathrm{NN2}} < 0.7$, where ω_{NN2} is a neural net output defined for jets containing a secondary vertex. $\omega_{\mathrm{NN2}} < 0.7$ is designed to distinguish between tracks from fragmentation and B decays. The inputs for ω_{NN2} are similar to the inputs for ω_{NN}, but also the impact parameter significances in the $x-y$ and the z plane with respect to the secondary vertex are used.

- From all tracks that pass the previous selection criteria, only the one with the highest longitudinal momentum with respect to the jet axis, p_l^{max}, is kept for each B candidate.

- A reduction of B decay track background in the $p_l^{\max}$ sample is obtained by the requirements $\omega_{\mathrm{NN}} < 0.80$ and $\omega_{\mathrm{NN2}} < 0.50$ [2].
- Fragmentation tracks in the $p_l^{\max}$ sample are removed with the requirement $\omega_{\mathrm{NN}} > 0.20$. Since ω_{NN} is designed to achieve optimal separation of b hadron decay tracks from fragmentation tracks using tracking information *and* kinematics, the Monte Carlo indicates a fairly flat ω_{NN} distribution for signal pions. On the contrary, fragmentation tracks peak at zero.
- A momentum of $p > 1.0$ GeV/c is required for signal pion candidates. In the simulation, the momentum distribution of signal pions has a mean value of 2.9 GeV/c with an RMS of 1.3 GeV/c before the cut is applied. The B_J^* mass spectrum for single pion transitions is not influenced by the momentum requirement.

8.2 B$\pi^{\pm}$ mass spectrum

The signal pion candidate passing the selection cuts described in Section 8.1 is combined with the corresponding B candidate to form a B_J^* candidate. The invariant mass is calculated using Equation 7.1 as for the B^* mass, where the photon is replaced by a pion and the appropriate pion mass term is added. The cuts of the signal pion selection have been chosen to obtain an acceptable signal-to-background ratio at high signal efficiency. The order of the non-commuting selection requirements using ω_{NN}, ω_{NN2} and $p_l^{\max}$ aims to maximise the difference between the shape of the signal and background contributions to the $M_{\mathrm{B}\pi}$ distribution.

Due to the intrinsic widths of the B_J^* states and the limited detector resolution, only a single peak is seen in the $M_{\mathrm{B}\pi}$ spectrum of Figure 8.1a on top of the combinatorial background. According to the simulation, the $M_{\mathrm{B}\pi}$ resolution can be described by the sum of a narrow Gaussian and an asymmetric Gaussian both constrained to the same mean value (see Figure 8.2). The mass resolution depends linearly on $M_{\mathrm{B}\pi}$. In the B_J^* signal region around 5.7 GeV/c^2 the standard deviation of the narrow Gaussian is $\sigma = 33$ MeV/c^2, and 85% of the resolution function entries are contained within 3σ. The reliability of the simulated B meson energy and direction resolution which dominate the Bπ mass resolution is proven by a well simulated shape and peak position of the B^* signal using the conversion photon sample (see Chapter 7).

The Monte Carlo combinatorial background is checked against data using different test samples strongly enhanced in each of the following physics background sources: 1. fake B_J^* candidates from light and charm quark events; 2. fake B_J^* arising from true b hadrons combined with a pion from the weak decay of the b hadron itself; 3. fake B_J^* formed by combining true b hadrons with fragmentation

[2] If no secondary vertex is present in the jet, the cut $\omega_{\mathrm{NN}} < 0.50$ instead of $\omega_{\mathrm{NN2}} < 0.50$ is applied.

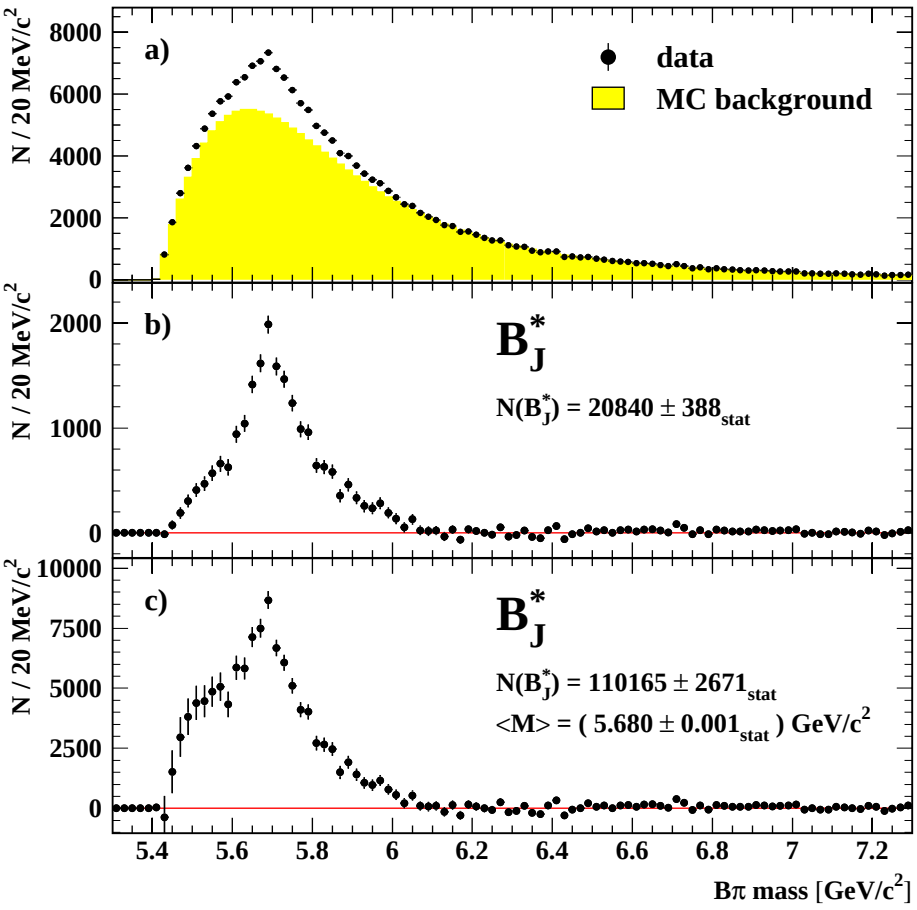

Figure 8.1: *a) The* $B\pi^{\pm}$ *mass distribution for data. The shaded histogram indicates a fit to the corrected Monte Carlo background using a reweighting method described in Section 11.1.3. The function used for the fit is described in the text. b) The Monte Carlo background-subtracted signal. c) The efficiency-corrected* B_J^* *signal. The observed structure of the* B_J^* *signal suggests a superposition of several different states. The mass dependent efficiency correction has a strong impact on the signal shape at low* $B\pi$ *mass values.*

tracks which have not come from a B_J^* resonance. The simulation indicates that each test sample is strongly enhanced in the background source under study and that the B_J^* signal is suppressed by about a factor of eight compared to the original B_J^* signal selection. The $B\pi$ mass distributions of the data background samples are compared with the corresponding Monte Carlo mass distributions (see also Section 11.1.3). In the case of a significant deviation, the simulated background is reweighted to the data. The Monte Carlo background distribution so obtained is fitted using a threshold function of the form $C_1 \cdot \sqrt{x-(m_B+m_\pi)} \cdot (\Phi(\frac{x-C_2}{C_3}))^{C_4}$, where Φ is the Landau density function[3]. This background function gives a good empirical fit with only four free parameters C_i. The fitted Monte Carlo background is normalised in the sideband region 6.04 GeV/c^2 $< M_{B\pi} <$ 7.04 GeV/c^2 and subtracted from the data distribution. The obtained B_J^* signal is shown in Figure 8.1b.

The reconstruction efficiency for B_J^* depends on the reconstructed mass $M_{B\pi}$. Monte Carlo studies indicate that the efficiency stays constant at high $M_{B\pi}$ values down to $M_{B\pi} = 5.7$ GeV/c^2. Below 5.7 GeV/c^2, the reconstruction efficiency becomes smaller as $M_{B\pi}$ decreases, mainly due to the $p_l^{\max}$ requirement. At the $B\pi$ mass threshold, the signal efficiency is close to zero. The B_J^* distribution corrected for efficiency is shown in Figure 8.1c.

The mean mass, shape and yield of the observed B_J^* signal is in agreement with other measurements [56, 58, 57, 59]. The structure of the $B\pi^{\pm}$ mass spectrum is too broad to stem from a single resonance and leaves room for interpretation. The peak is expected to contain two broad and two narrow B_J^* states and due to the photon which is not taken into account in the case of the decay $B_J^* \to B^*\pi$, part of the true mass spectrum is shifted to lower mass values by 46 MeV/c^2. The peak also includes a small fraction of B_{sJ}^* due to the misidentification of kaons as pions. In addition, the peak may contain contributions from $B_J^* \to B^{(*)}\pi\pi$ giving rise to satellite peaks in the region 5.4 GeV/c^2 $< M_{B\pi} <$ 5.6 GeV/c^2, since the second pion is not included in the invariant mass calculation. If broad B_J^* states have masses close to the $B\pi$ threshold, they have an asymmetric signal shape due to phase space suppression. Also contributions from radially-excited B mesons in the decay channels $B^{(*)\prime} \to B^{(*)}\pi$ and $B^{(*)\prime} \to B^{(*)}\pi\pi$ may contribute, although the production rate of $B^{(*)\prime}$ is assumed to be small compared to the B_J^* production rate according to [28] and [27, 111]. Since there are several ambiguities, e.g. due to $B_J^* \to B^{(*)}\pi\pi$, $B^{(*)\prime}$ decays and uncertainties in the combinatorial background, further details of the signal composition can only be obtained by making additional, model dependent assumptions.

8.3 Fit to the $B\pi^{\pm}$ mass spectrum

A least squares fit is performed to the background subtracted and acceptance corrected $B\pi$ mass spectrum shown in Figure 8.1c. Several assumptions are made

[3] $\Phi(\lambda) = \frac{1}{2\pi i}\int_{c-i\infty}^{c+i\infty} e^{\lambda s + \ln s} ds$

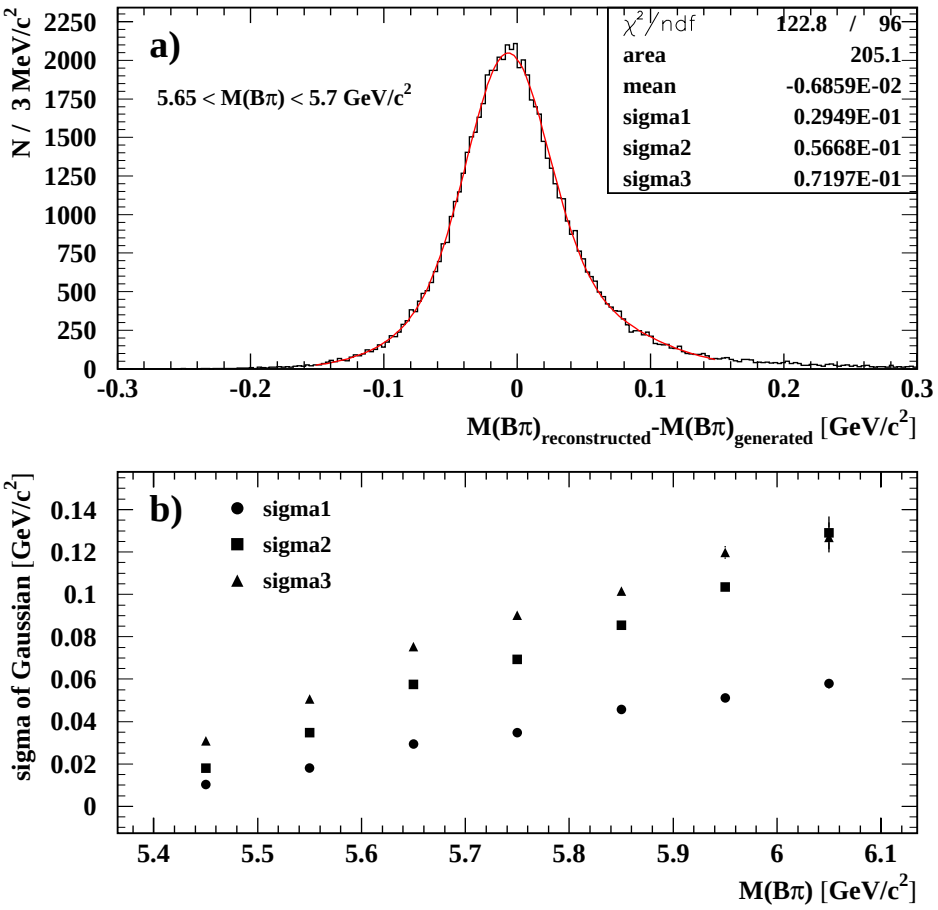

Figure 8.2: *a) Monte Carlo* $M_{\mathrm{B}\pi}$ *resolution of* B_J^* *decaying to* $\mathrm{B}^{(*)}\pi^{\pm}$ *in the mass region* $5.65\ \mathrm{GeV}/c^2 < M(\mathrm{B}\pi) < 5.70\ \mathrm{GeV}/c^2$. *The fit function is the sum of two Gaussians both constrained to the same mean value.* sigma1 *is the standard deviation of the narrow Gaussian and* sigma2 *(*sigma3*) corresponds to the left (right) standard deviation of the asymmetric broad Gaussian. b) The linear dependence of the width of the resolution function on* $M_{\mathrm{B}\pi}$ *is shown for each sigma in the* B_J^* *signal region.*

state	J_j^P	fit constraints			allowed decay modes
		production rate	mass	width	
B_0^*	$0^+_{1/2}$	f(b $\to B_0^*$)	free	free	$B\pi$, $B^*\pi\pi$, $B\pi\pi$
B_1	$1^+_{1/2}$	f(b $\to B_0^*$)	$M(B_0^*)$ + 20 MeV/c^2	1.25 $\cdot$, (B_0^*)	$B^*\pi$, $B^*\pi\pi$, $B\pi\pi$
B_1	$1^+_{3/2}$	f(b $\to B_1(\frac{3}{2})$)	free	free	$B^*\pi$, $B^*\pi\pi$, $B\pi\pi$
B_2^*	$2^+_{3/2}$	f(b $\to B_1(\frac{3}{2})$)	$M(B_1(\frac{3}{2}))$+12 MeV/c^2	1.00 $\cdot$, ($B_1(\frac{3}{2})$)	$B^*\pi$, $B\pi$, $B^*\pi\pi$, $B\pi\pi$

Table 8.1: *Constraints on production rates, masses and widths used in the fit to the total* $B\pi$ *mass spectrum.*

on the nature of the observed signal:

- The signal excess stems from B_J^* decays. Contributions from B_{sJ}^* decays, $B^{(*)\prime} \to B^{(*)}\pi$ and $B^{(*)\prime} \to B^{(*)}\pi\pi$ do not exceed a few percent [56, 27, 60, 28] and are therefore not implemented in the fit but considered as sources of systematic uncertainty. Any other excited state eventually contributing to the signal peak is ignored since there is no experimental evidence for such states and theoretical predictions give negligible production rates.

- The heavy quark limit $m_Q \to \infty$ holds to describe the four B_J^* states. Therefore, according to spin-parity conservation, one expects five different mass peaks from single pion transitions as listed in the first paragraph of Section 2.6 and shown in Figure 2.6. Furthermore, the physical B_1 states are $B_1(1/2)$ and $B_1(3/2)$ and thus no mixing occurs.

- Partners of the same doublet are assumed to have similar properties. The constraints on masses, widths and production rates used in the fit are presented in Table 8.1. The mass splitting between the narrow states can be calculated using the corresponding mass splitting of the D_J^* which has been measured [26]. The mass splitting between the broad states is expected to be of about the same size. Also the order of magnitude of the widths of the narrow and broad B_J^* states can be estimated from experimental D_J^* results [26, 112].

- Only the decay modes listed in Table 8.1 are taken into account. I explicitly allow the decay via two pions to B^* and B for all B_J^* states. For each B_J^* state, I set $BR(B_J^* \to B^*\pi\pi) = BR(B_J^* \to B\pi\pi)$ and I assume the same branching ratio $BR(B_J^* \to B^{(*)}\pi\pi)$ for all B_J^* states[4]. In a set of systematic studies, I also analyse fit results under the assumption $BR(B_J^* \to B^*\pi\pi) = 0$. For the B_2^*, I set $BR(B_2^* \to B^*\pi) = BR(B_2^* \to B\pi)$.

[4]The fit is rather insensitive to these requirements.

- The fraction of narrow states $f_{narrow} := (f(b \to B_1(3/2)) + f(b \to B_2^*))/f(b \to B_J^*)$ is fixed to 0.6. This number is the average of 1/2, 2/3 and 2/3 corresponding to production rates of narrow B_J^* according to state counting, total spin counting and light quark spin counting, respectively. To justify this constraint, the fit is also performed with f_{narrow} as an additional free parameter.

- The mass splitting between B and B^* is fixed to the current world average [26].

- Each of the five single pion decay modes is represented by a Breit-Wigner function convoluted with the $M_{B\pi}$ dependent resolution function explained in Section 8.2 and shown in Figure 8.2. To take into account the phase space suppression at threshold, asymmetric Breit-Wigner functions with the threshold factor [113]

$$\sqrt{\left(1 - \frac{M_B^2}{M^2} - \frac{M_\pi^2}{M^2}\right)^2 - 4 \cdot \frac{M_B^2 M_\pi^2}{M^4}}$$

  are used instead of the symmetric Breit-Wigner functions for the broad states. Since different theoretical models predict a different shape for resonances near threshold, also symmetric Breit-Wigner functions truncated at the $B\pi$-threshold are used to evaluate systematic uncertainties in the shape of the functions used in the fit.

- For the double pion transitions, the signal shape including the detector resolution is taken from simulated $B_J^* \to B^{(*)}\pi\pi$ decays. Simple Gaussians truncated at threshold give a good description of the simulated satellite peaks. The mean of the Gaussian depends linearly on the mass difference between B_J^* and B ground state. The width of the Gaussian is also a function of this mass splitting and depends on the width of the B_J^* state. The functions to parameterise the mean and width of the Gaussians are taken from the simulation. No attempt is made to implement different signal shapes for decays where the two pions form an intermediate resonance or for cascade transitions from high mass B_J^* states via low mass B_J^* states to the ground states B^* and B [5].

With the assumptions and constraints listed above, the following free fit parameters remain: the number of B_J^* signal entries, $M(B_1(3/2))$, , $(B_1(3/2))$, $M(B_0^*)$, , (B_0^*) and $BR(B_J^* \to B^{(*)}\pi\pi)$. A fit [114] is performed to the simulated B_J^* signal using the full Monte Carlo statistics. All fit results lie within 1σ of the Monte Carlo input value. The same fit applied to the mass spectrum of Figure 8.1c

[5] Strong decays within the B_J^* multiplet are allowed if the mass splitting within the multiplet or some of the widths are larger than the pion mass.

yields the following fit results (numbers with a ($\star$) should be taken with great care because of large systematic uncertainties):

$$\begin{aligned}
M(\mathrm{B}_1(3/2)) &= (\,5.733 \pm 0.004\,)\ \mathrm{GeV}/c^2 \\
,\,(\mathrm{B}_1(3/2)) &= (\,15\,^{+\,10}_{-\,9}\,)\ \mathrm{MeV}/c^2 \\
M(\mathrm{B}_0^*) &= (\,5.843\,^{+\,0.012}_{-\,0.014}\,)\ \mathrm{GeV}/c^2 \qquad (\star) \\
,\,(\mathrm{B}_0^*) &= (\,140\,^{+\,31}_{-\,25}\,)\ \mathrm{MeV}/c^2 \qquad (\star) \\
\mathrm{BR}(\mathrm{B}_J^* \to \mathrm{B}^{(*)}\pi\pi) &= 0.248\,^{+\,0.025}_{-\,0.027} \qquad (\star)
\end{aligned}$$

The fit range of this fit is $5.40 - 6.10$ GeV/c^2 with a bin width of 20 MeV/c^2. The probability of the fit is 33% and the fit result is shown in Figure 8.3. The $\mathrm{BR}(\mathrm{B}_J^* \to \mathrm{B}^{(*)}\pi\pi)$ number is the fraction of the total number of signal entries contributing to the $\mathrm{B}^*\pi\pi$ and $\mathrm{B}\pi\pi$ final states multiplied by a factor of 0.75 to account for the increased pion detection efficiency in the case of $\mathrm{B}_J^* \to \mathrm{B}^{(*)}\pi^+\pi^-$ decays. The same fit has been repeated with $\mathrm{f_{narrow}}$ as an additional free parameter. The fit results are in good agreement with the results presented above and I measure $\mathrm{f_{narrow}} = 0.76\,^{+\,0.11}_{-\,0.24}$. This number is in agreement with 0.6 used in the original fit. The additional parameter $\mathrm{f_{narrow}}$ causes a serious increase of the correlations between several fit parameters.

An important issue is the robustness of the presented fit results. Extensive systematic studies have been performed to test the stability of the fit. As will be discussed in Chapter 11, systematic uncertainties are determined to be much larger than the corresponding statistical uncertainties in the region of small $\mathrm{B}\pi$ masses. This results in a marginal significance for the existence of $\mathrm{B}_J^* \to \mathrm{B}^{(*)}\pi\pi$ transitions. Therefore, the same fit has been repeated with fixed $\mathrm{B}_J^* \to \mathrm{B}^{(*)}\pi\pi = 0$ and the observed fit probabilities vary in the range 0-2%, depending on the functional form implemented for the broad states. This low fit probability indicates the existence of an additional contribution to the $\mathrm{B}\pi$ mass spectrum besides the $\mathrm{B}_J^* \to \mathrm{B}^{(*)}\pi$ decays. Unfortunately, if $\mathrm{B}_J^* \to \mathrm{B}^{(*)}\pi\pi = 0$ is assumed, the mass and width of the broad state is not stable and depends on the implemented asymmetric Breit-Wigner function. Besides the fit results presented above, also a $\mathrm{B}_1(1/2)$ mass around 5.6 GeV/c^2 is a fit solution for a specific threshold function. Since there is no single definite theoretical prediction for the analytical description of the threshold behaviour this ambiguity cannot be resolved with the given data. The mass and widths of $\mathrm{B}_1(3/2)$ is not affected by the described problems. Conservatively, I only quote the mass and the width of the $\mathrm{B}_1(3/2)$ as robust fit results.

Additional systematic errors arising from the fit constraints and the signal pion selection, especially the uncertainties assigned to the combinatorial background in the $\mathrm{B}\pi^{\pm}$ mass spectrum and to the selection efficiency, will be discussed in detail in Chapter 11.

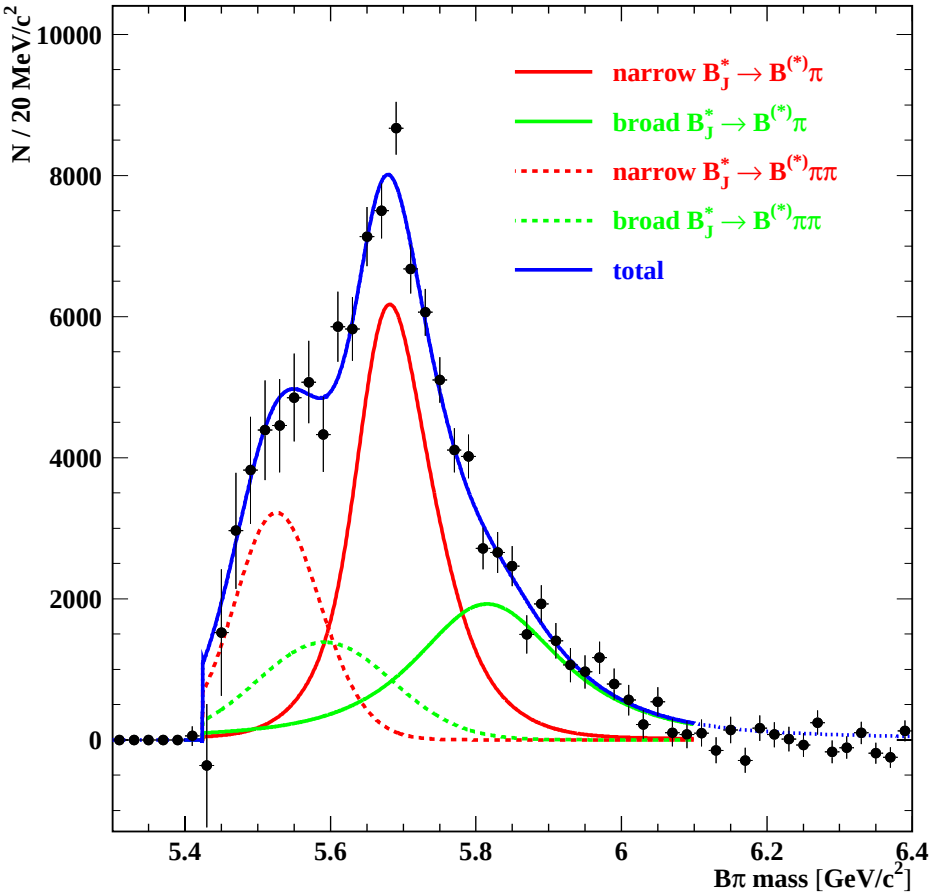

Figure 8.3: *The fit to the total* $B\pi^{\pm}$ *mass distribution. Narrow states dominate the centre of the mass peak. Broad states give contributions to high mass values, whereas the shoulder at low* $B\pi$ *masses is due to* $B_J^* \to B^{(*)}\pi\pi$ *decays with only one reconstructed pion. The fraction of* $B^{(*)}\pi\pi$ *decays of the total* B_J^* *signal has to be multiplied by a factor of 0.75 to correct for double counting in the* $B^{(*)}\pi^+\pi^-$ *final state.*

experiment	method	B_J^* statistics	background	$m_{B\pi}$ resolution
OPAL [56]	incl.+vertex charge	1738 ± 121	charge+MC	$\approx 35\,\mathrm{MeV}/c^2$
DELPHI [57]	inclusive	2157 ± 120	Monte Carlo	$\approx 40\,\mathrm{MeV}/c^2$ ($\star$)
ALEPH [59]	inclusive	1944 ± 108	Monte Carlo	$\approx 40\,\mathrm{MeV}/c^2$
ALEPH [58]	excl., B charge	41 ± 10	charge (data)	$2 - 5\,\mathrm{MeV}/c^2$
L3 [28]	inclusive	2770 ± 394	Monte Carlo	$10 - 80\,\mathrm{MeV}/c^2$ ($\star$)
CDF [115]	semi-excl., B charge	762 ± 163 ($\star$)	charge+MC	$\approx 45\,\mathrm{MeV}/c^2$ ($\star$)
this work [117]	inclusive	$20\,840 \pm 388$	data+MC	$20 - 50\,\mathrm{MeV}/c^2$

Table 8.2: *Comparison of different* B_J^* *measurements. The reconstruction method, determination of the combinatorial background, number of* B_J^* *signal entries and the* $B\pi$ *mass resolution is listed. Numbers with a* ($\star$) *sign are not quoted in the corresponding publications but inferred indirectly by the available information.*

8.4 Comparison with other measurements

Orbitally-excited B mesons have been observed for the first time in 1995 by OPAL and DELPHI [56, 57]. Other LEP experiments followed [58, 59, 28] and also CDF has presented a B_J^* signal recently [115, 116]. All analyses are based on a reconstruction of the $B\pi$ final state using different techniques. The range of methods covers fully reconstructed B mesons with good resolution but poor statistics, semi-inclusive to totally inclusive methods which exploit properties common to all b hadron decay modes. The latter provide high statistics but a moderate direction and energy resolution. An important issue is the determination of the combinatorial background. Whereas some analyses (e.g. [28]) rely totally on the Monte Carlo modelling, a determination of the charge of the B meson [56, 58] allows to define samples of unlike-sign ($B^+\pi^-$) and like-sign ($B^+\pi^+$) combinations[6]. These samples can be used to obtain the background shape for the main background source directly from data. For inclusive methods, systematic uncertainties in the combinatorial background dominate the uncertainties of the B_J^* signal. In this work I present a method which allows the determination of systematic uncertainties of different background sources while maintaining high statistics (see Chapter 11).

As shown in Table 8.2, with this analysis very high statistics is achieved while the $M_{B\pi}$ mass resolution and the signal to background ratio is similar to other analyses using an inclusive B reconstruction. To obtain the true shape of the B_J^* signal, the mass distribution has been corrected for the $M_{B\pi}$ acceptance (see Figure 8.1). So far the $M_{B\pi}$ dependence of the reconstruction efficiency has been ignored by all B_J^* analyses except [115]. Nevertheless, all analyses observe a broad signal structure which cannot be explained by a single resonance. Even analysis [58] with its excellent mass resolution does not resolve any B_J^* substructure. As mentioned at the beginning of this chapter this is in agreement with the expectation.

[6] Charge conjugate processes are implied.

All experiments observe a similar B_J^* production rate. My average of all measurements not including this analysis is $f(\bar{b} \to B_J^*) = 0.25 \pm 0.03$. The production rate observed in this analysis is consistent with the calculated average and using the method presented in Chapter 11 a relative systematic uncertainty of almost 25% is obtained. The previous OPAL result [56] has a total error of about 20% and is therefore superior concerning the determination of the production rate.

A B_J^* mass is extracted from the signal peak by all experiments. Most experiments calculate the average B_J^* mass. Some correct for the mass shift due to decays to B^*, others do not. Most experiments do not correct the B_J^* signal shape for the mass dependent acceptance. Several experiments ([58, 115, 28]) fit a spectrum of B_J^* states to the signal in the context of Heavy Quark Symmetry implementing different constraints and free fit parameters. The average B_J^* mass of the efficiency corrected signal distribution extracted from Figure 8.1c is $5.680 \pm 0.004_{\text{stat}} \pm 0.012_{\text{sys}}$ where the systematic error is the systematic error originally addressed to $M(B_1(3/2))$ (see Chapter11). Ignoring the details of how the different results are obtained, the quoted B_J^* masses are compared in Figure 8.4.

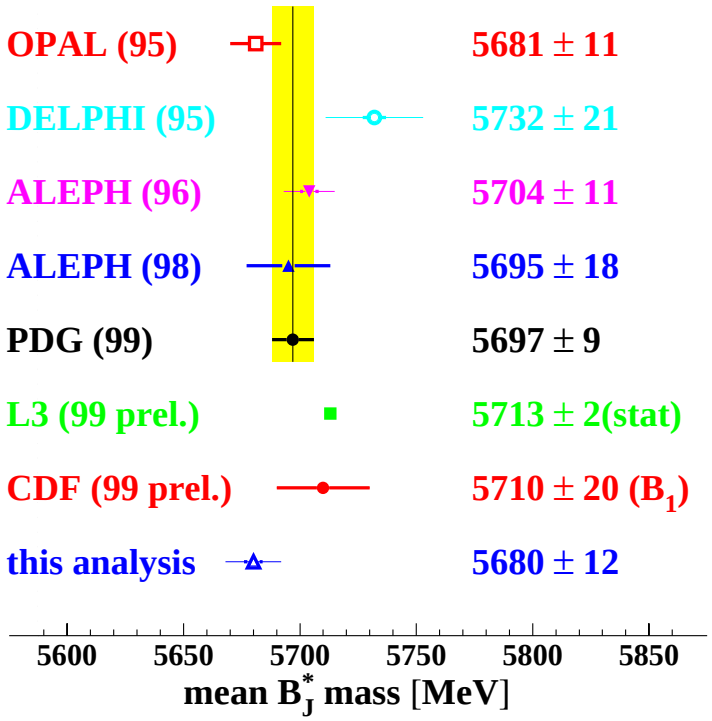

Figure 8.4: *Different* B_J^* *mass measurements. The comparison should be treated with care since different methods and corrections have been applied (or not applied) to achieve the different results.*

The parameters obtained from the fit to the $B\pi$ mass spectrum shown in Figure 8.3 can be compared with a similar fit presented in [28]. In [28], several corrections which are applied in this analysis have not been considered. For example, the background is simply taken from Monte Carlo and no cross check with data or any additional correction of the simulated background is performed. Furthermore, the drop of efficiency at low $B\pi$ mass values is not taken into account. This is expected to cause a major change in the B_J^* signal shape at low mass values due to the $p_l^{\max}$ requirement used in [28]. The problem of the correct threshold function is not addressed. The results presented in [28] differ from the results shown in Section 8.3. The masses of the narrow B_J^* states agree within 2σ of the quoted errors, while masses of the broad B_J^* states clearly disagree. Instead of high mass broad B_J^* states, an additional $B^{(*)\prime} \to B^{(*)}\pi$ signal is assumed near $M_{B\pi} \approx 5.9$ in [28] to improve the fit probability. The structure observed at low masses is assigned to broad B_J^* states while $BR(B_J^* \to B^{(*)}\pi\pi) = 0$ is assumed.

I conclude that results for broad B_J^* from a fit to the $M_{B\pi}$ distribution as presented in [28] and Section 8.3 should be taken with great care. The limited statistics and moderate mass resolution, uncertainties in the background modelling and a not precisely known number and fraction of additional decay modes of excited B states possibly contributing to the B_J^* signal make it hard to extract reliable numbers. Results from other experiments are desired. A different approach to reveal more information about the nature of the B_J^* signal is presented in the following chapter.

Chapter 9

B_J^* Transitions to B^* and to B

In this chapter, the B^* analysis presented in Chapter 7 and the B_J^* analysis of Chapter 8 are combined. For the first time, the reconstruction of B^* mesons is used to gain insight into the composition of the B_J^* multiplet. A high statistics B^* selection and the implementation of the B^* weight $\mathcal{W}(B^*)$ are important prerequisites for the success of this work. The total B_J^* sample is divided into two samples, one enriched and one depleted in the decay $B_J^* \to B^*\pi(\pi)$, by applying a cut on $\mathcal{W}(B^*)$, as indicated in Figure 7.7a. These two B_J^* samples allow a model independent measurement of $BR(B_J^* \to B^*\pi(\pi))$, where no distinction between decays to $B^*\pi$ and $B^*\pi\pi$ is possible[1]. A fit similar to the one presented in Section 8.3 but with $BR(B_J^* \to B^*\pi)$ as an additional free fit parameter is performed: the $BR(B_J^* \to B^*\pi)$ is not fixed to the HQET prediction, but considered as one of the fit parameters. The branching ratio $BR(B_J^* \to B^*\pi)$ does not include the $B^*\pi\pi$ final state by definition of the fit parameters since the sensitivity of the fit to di-pion transitions of the B_J^* is negligible.

9.1 Model independent $BR(B_J^* \to B^*\pi(\pi))$ measurement

The branching ratio of orbitally-excited B mesons decaying into $B^*\pi(\pi)$ is obtained by counting the number of signal entries of the B_J^* samples enriched or depleted in the decay $B_J^* \to B^*\pi^\pm(\pi)$. The cut value on $\mathcal{W}(B^*)$ is chosen to minimise uncertainties of the measurement. The statistical error on $BR(B_J^* \to B^*\pi(\pi))$ is minimal if both subsamples are of the same size. Systematic uncertainties in the $B\pi^\pm$ background have minimal impact on $BR(B_J^* \to B^*\pi(\pi))$ if the signal-to-background ratio is the same for the $B\pi^\pm$ mass distributions of the B^*-enriched and the B^*-depleted sample. The optimal cut on $\mathcal{W}(B^*)$ is 0.648, fulfilling the minimal systematic error requirement and coming as close as possible to the minimum statistical error requirement (see Figure 7.7).

[1] Contributions from other decays $B_J^* \to B^*\pi X$ ($X \neq 1\pi$) are expected to be negligible.

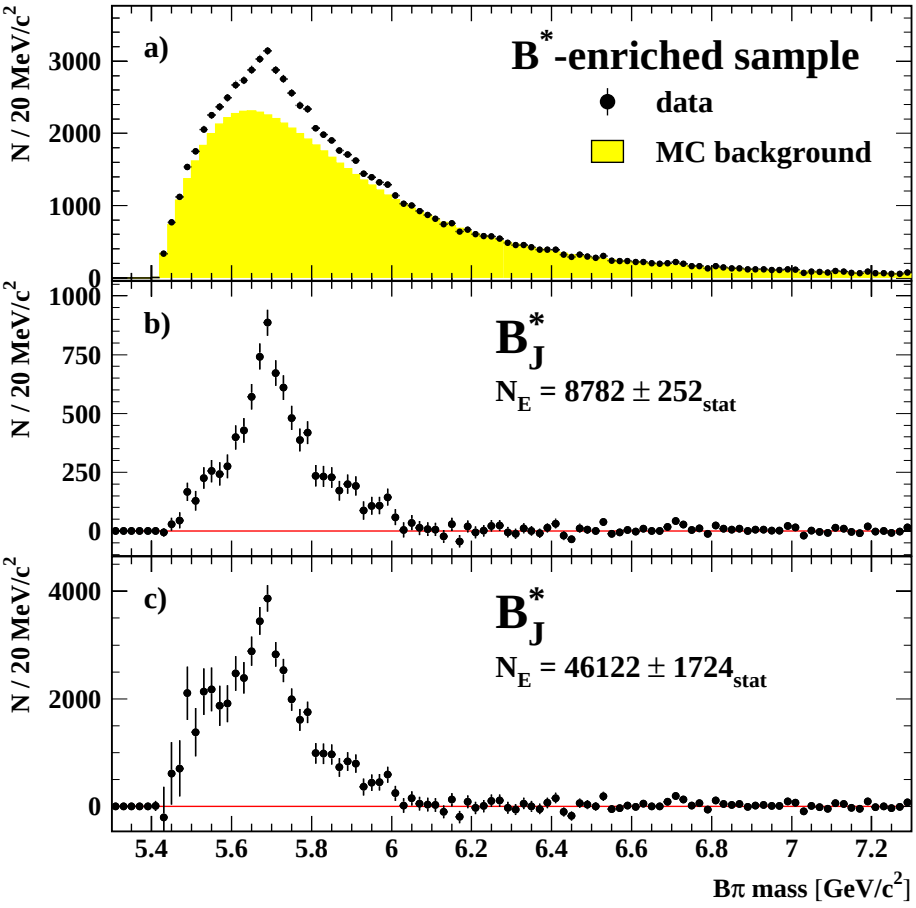

Figure 9.1: *a) The* $B\pi^{\pm}$ *mass distribution of the sample enriched in the decay* $B^*_J \to B^*\pi^{\pm}(\pi)$ *in data. The shaded histogram indicates a fit to the corrected Monte Carlo background using a reweighting method described in Sections 11.1.3 and 11.2.2. b) The signal distribution after background subtraction. c) The efficiency-corrected signal.*

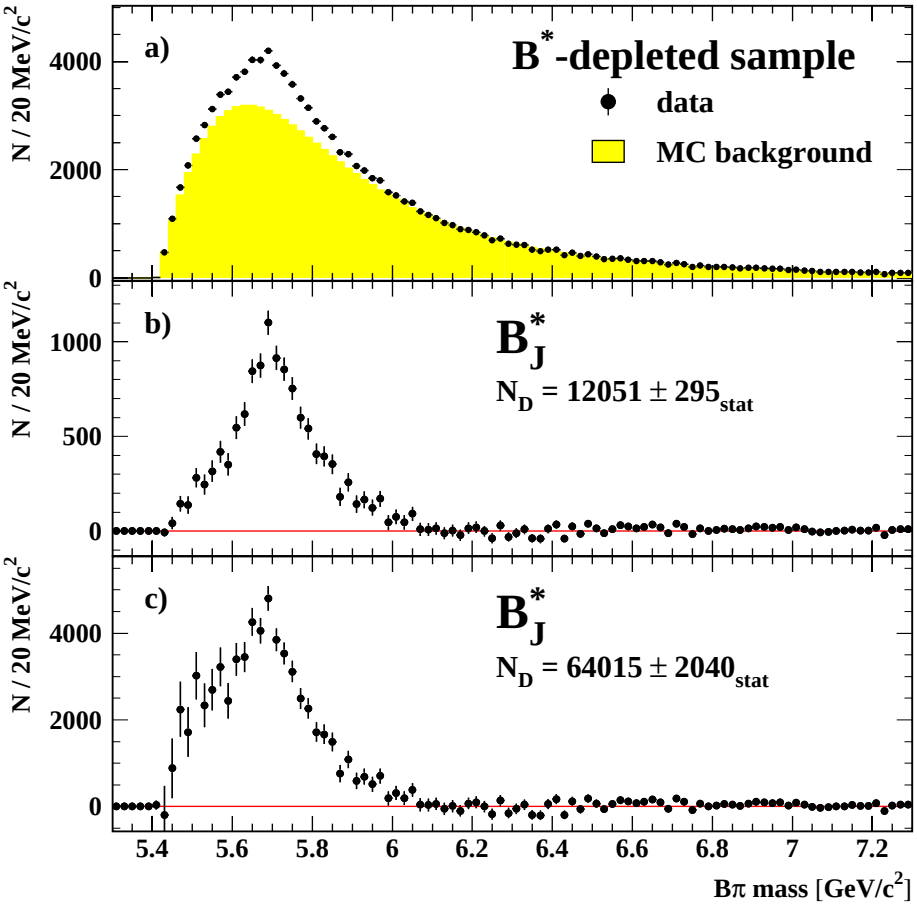

Figure 9.2: *a) The* $B\pi^{\pm}$ *mass distribution of the sample depleted in the decay* $B_J^* \to B^*\pi^{\pm}(\pi)$ *in data. The shaded histogram indicates a fit to the corrected Monte Carlo background using a reweighting method described in Sections 11.1.3 and 11.2.2. b) The signal distribution after background subtraction. c) The efficiency-corrected signal.*

The B^* enrichment and depletion method can be evaluated by the different selection efficiencies for the transitions $B^*_J \to B^*\pi^\pm$ and $B^*_J \to B\pi^\pm$ in the B^*-enriched and B^*-depleted samples. With the definitions

- $\varepsilon^*_{\rm E}$: $B^*_J \to B^*\pi$ efficiency of B^*-enriched sample;
- $\varepsilon^*_{\rm D}$: $B^*_J \to B^*\pi$ efficiency of B^*-depleted sample;
- $\varepsilon_{\rm E}$: $B^*_J \to B\pi$ efficiency of B^*-enriched sample;
- $\varepsilon_{\rm D}$: $B^*_J \to B\pi$ efficiency of B^*-depleted sample;
- efficiency ratios : $e_0 = \varepsilon_{\rm D}/\varepsilon^*_{\rm E}$; $e = \varepsilon_{\rm E}/\varepsilon_{\rm D}$; $e^* = \varepsilon^*_{\rm D}/\varepsilon^*_{\rm E}$,

I calculate from Monte Carlo the efficiency values presented in Table 9.1. The numbers reflect the cut on $\mathcal{W}(B^*)$ and thus the quality of the B^* enrichment versus the B^* depletion. Only the efficiency ratios given in the right column of Table 9.1 (but not the absolute efficiencies) are needed for the determination of BR($B^*_J \to B^*\pi(\pi)$), cancelling partially some systematic errors. For the

efficiency		efficiency ratio	
$\varepsilon^*_{\rm E}$	0.05084 ± 0.00023	e_0	1.566 ± 0.010
$\varepsilon^*_{\rm D}$	0.06680 ± 0.00026	e	0.578 ± 0.005
$\varepsilon_{\rm E}$	0.04601 ± 0.00030	e^*	1.314 ± 0.008
$\varepsilon_{\rm D}$	0.07962 ± 0.00039		

Table 9.1: *Efficiencies for the reconstruction of* B^*_J *decaying to* $B^*\pi$ *and to* $B\pi$. *The numbers are calculated with respect to the total number of* B^*_J *passing the* B *selection in the Monte Carlo. Therefore, the numbers reflect the effect of the cut on* $\mathcal{W}(B^*)$ *and the charged pion selection. A factor of 2/3, derived from isospin symmetry, is included in each of the efficiency values to account for decays of* B^*_J *mesons through neutral pions. The errors are of statistical origin only.*

BR($B^*_J \to B^*\pi(\pi)$) measurement, the invariant $B\pi^\pm$ mass distributions of the B^*-enriched and the B^*-depleted sample are used. Both mass distributions are independent subsamples of the distribution shown in Figure 8.1, but contain different compositions of $B^*_J \to B^*\pi^\pm(\pi)$ and $B^*_J \to B\pi^\pm(\pi)$ decays. Figures 9.1 and 9.2 show the $B\pi^\pm$ mass distributions for the B^*-enriched and the B^*-depleted sample, respectively. The Monte Carlo background distributions of both samples are corrected using the procedure described in Section 8.2 and Chapter 11. The same fit procedure for the background of the total B^*_J sample is adopted as in Section 8.3. The fitted background functions are normalised in the sideband region 6.04 GeV/c^2 < $M_{B\pi}$ < 7.04 GeV/c^2 and subtracted from the corresponding data distributions. From the resulting signal peaks of Figures 9.1b and 9.2b, BR($B^*_J \to B^*\pi(\pi)$) is obtained using the following ansatz:

$$N_E \;=\; N^* \cdot \varepsilon^*_{\rm E} + N \cdot \varepsilon_{\rm E} \qquad (9.1)$$

$$N_D = N^* \cdot \varepsilon_{\mathrm{D}}^* + N \cdot \varepsilon_{\mathrm{D}} \tag{9.2}$$

$$\mathrm{BR}(\mathrm{B}_J^* \to \mathrm{B}^*\pi) = \frac{N^*}{N^* + N}\,, \tag{9.3}$$

where N^* denotes the number of true B_J^* transitions to B^* and N denotes the number of true B_J^* transitions to B. With the efficiency ratios defined as above, the following formula is obtained:

$$\mathrm{BR}(\mathrm{B}_J^* \to \mathrm{B}^*\pi(\pi)) = e_0 \cdot \frac{N_{\mathrm{E}} - e \cdot N_{\mathrm{D}}}{(e_0 - e^*) \cdot N_{\mathrm{E}} + (1 - e \cdot e_0) \cdot N_{\mathrm{D}}}\quad, \tag{9.4}$$

where N_{E} (N_{D}) denotes the number of B_J^* signal entries of the B^*-enriched (B^*-depleted) sample. In the data, $N_{\mathrm{E}} = (8782 \pm 252_{\mathrm{stat}})$ and $N_{\mathrm{D}} = (12051 \pm 295_{\mathrm{stat}})$ B_J^* candidates are observed in the $M_{\mathrm{B}\pi}$ signal window $(5.3 - 6.1)$ GeV/c^2. Using the numbers for the efficiency ratios e_0, e and e^* presented in Table 9.1, the value $\mathrm{BR}(\mathrm{B}_J^* \to \mathrm{B}^*\pi(\pi)) = 0.85$ is obtained.

The statistical errors on N_{E} and N_{D} result in a total error on the branching ratio of ± 0.13. Beside this error, statistical uncertainties due to the sideband normalisation have been taken into account. Since the samples are mutually exclusive, the statistical errors of the sideband normalisation of both samples are independent. The contributions of the B^*-enriched and the B^*-depleted sample sideband normalisation to the statistical error on $\mathrm{BR}(\mathrm{B}_J^* \to \mathrm{B}^*\pi(\pi))$ are $^{+0.17}_{-0.18}$ and ± 0.15, respectively. Adding all quoted errors in quadrature, the branching ratio of orbitally-excited B mesons decaying into B^* is measured to be

$$\mathrm{BR}(\mathrm{B}_J^* \to \mathrm{B}^*\pi(\pi)) = 0.85\,^{+0.26}_{-0.27}\,,$$

where the error is the statistical error only. This branching ratio includes all decays of the type $\mathrm{B}_J^* \to \mathrm{B}^{(*)}\pi\mathrm{X}$, as no cut against additional B_J^* decay products is applied. Besides $\mathrm{B}_J^* \to \mathrm{B}^{(*)}\pi$ and $\mathrm{B}_J^* \to \mathrm{B}^{(*)}\pi\pi$, no other decay modes are expected to contribute significantly to the BR [2]. Consequently, the notation $\mathrm{BR}(\mathrm{B}_J^* \to \mathrm{B}^*\pi(\pi))$ is chosen.

I further investigate the composition of the reconstructed B_J^* sample according to the decays $\mathrm{B}_J^* \to \mathrm{B}^*\pi^\pm(\pi)$ and $\mathrm{B}_J^* \to \mathrm{B}\pi^\pm(\pi)$. By subtracting from the $\mathrm{B}\pi$ mass distribution of the B^*-enriched sample the corresponding distribution of the B^*-depleted sample multiplied by a scale factor, a $\mathrm{B}\pi^\pm$ mass distribution containing $\mathrm{B}_J^* \to \mathrm{B}^*\pi^\pm(\pi)$ transitions only is obtained. The scale factor is the ratio of the $\mathrm{B}_J^* \to \mathrm{B}\pi^\pm$ efficiencies of both samples, $e = \varepsilon_{\mathrm{E}}/\varepsilon_{\mathrm{D}}$. In a similar way, a mass distribution with $\mathrm{B}_J^* \to \mathrm{B}^*\pi^\pm(\pi)$ decays subtracted off is obtained. The corresponding efficiency-corrected $\mathrm{B}\pi^\pm$ mass distributions for pure $\mathrm{B}_J^* \to \mathrm{B}^*\pi^\pm(\pi)$ and pure $\mathrm{B}_J^* \to \mathrm{B}\pi^\pm(\pi)$ transitions are shown in Figure 9.3.

A significant excess of entries is seen in the pure $\mathrm{B}_J^* \to \mathrm{B}^*\pi^\pm(\pi)$ distribution at masses around 5.7 GeV/c^2 with tails down to 5.5 GeV/c^2 and up to

[2] According to the fit results of Section 8.3, also transitions via three pions are kinematically allowed. Due to the small phase space available, these transitions can be ignored.

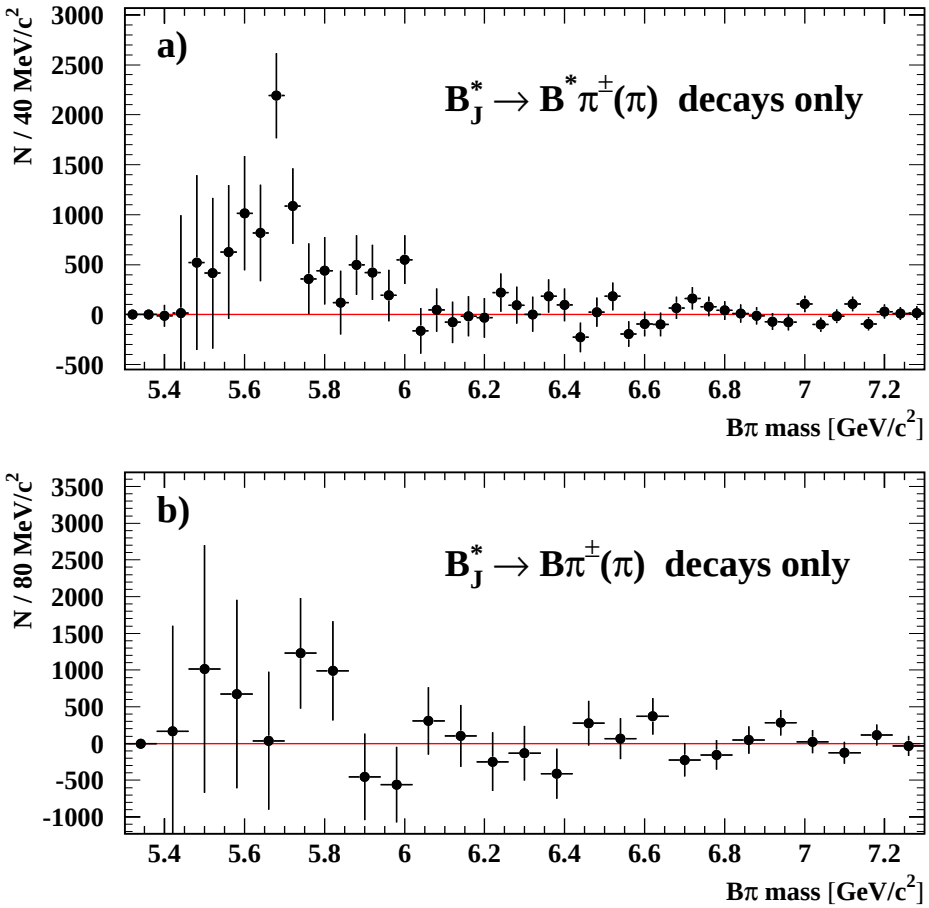

Figure 9.3: *a) The efficiency-corrected* $B\pi^{\pm}$ *mass distribution of* $B^*_J \to B^*\pi^{\pm}(\pi)$ *transitions seen in data. A clear peak is visible at* 5.7 GeV/c^2. *The structure is unlikely to stem from a single state. b) The efficiency-corrected* $B\pi^{\pm}$ *mass distribution of* $B^*_J \to B\pi^{\pm}(\pi)$ *transitions seen in data. A* 2.2σ *excess is observed around* 5.8 GeV/c^2.

6.0 GeV/c^2. The narrow peak in the $B_J^* \to B^*\pi^\pm(\pi)$ distribution is most likely due to $B_1(3/2) \to B^*\pi^\pm$ and $B_2^* \to B^*\pi^\pm$ decays. To obtain the true mass values of the $B^*\pi$ states, the entries have to be shifted to higher masses by 46 MeV/c^2.

In the pure $B_J^* \to B\pi^\pm(\pi)$ mass distribution, a small excess is observed in the region up to 5.85 GeV/c^2. This excess can be assigned to the decays $B_2^* \to B\pi^\pm$ and $B_0^* \to B\pi^\pm$. Since the statistical significance of the excess in the $B_J^* \to B\pi^\pm(\pi)$ mass distribution is small, no further conclusion is drawn from Figure 9.3b.

9.2 Simultaneous fit to the $B\pi^\pm$ mass spectra

The result of the fit to the total $B\pi^\pm$ mass spectrum shown in Figure 8.3 and the signal observed in the decay mode $B_J^* \to B^*\pi^\pm(\pi)$ suggest that a fit to the $B\pi^\pm$ mass spectra of the two samples enriched and depleted in the decay $B_J^* \to B^*\pi^\pm(\pi)$ could yield more informations on the structure of the B_J^* multiplet. A simultaneous fit to the mass spectra of Figures 9.1c and 9.2c is performed employing the same mass constraints and fit parameters as for the fit presented in Section 8.3, but with $BR(B_J^* \to B^*\pi)$ as an additional free parameter. The different reconstruction efficiencies for $B_J^* \to B^*\pi^\pm$ and $B_J^* \to B\pi^\pm$ decays of the B*-enriched and B*-depleted signals are taken from Monte Carlo (see Table 9.1). As the specific peaks that make up the total B_J^* signal have different size in the B*-enriched and B*-depleted mass spectra, different enhancements or depletions are expected for specific regions of the $B\pi^\pm$ mass spectra according to the assumptions on the nature of the B_J^* signal. Thus the simultaneous fit provides a non-trivial consistency check of the fit results presented in Section 8.3, the $BR(B_J^* \to B^*\pi(\pi))$ result of Subsection 9.1 and the constraints used in the fit.

The introduction of $BR(B_J^* \to B^*\pi)$ as an additional fit parameter causes a significant complication of the fit. Note that the $BR(B_J^* \to B^*\pi(\pi))$ result of Subsection 9.1 includes transitions of narrow B_J^* and broad B_J^* via emission of one or two pions. The branching fraction to the B* state might be different for narrow and broad states and also different for $B^*\pi$ and $B^*\pi\pi$ final states. Whereas the result obtained from formula (9.4) is the average of the natural composition of the four different decay modes, four different parameters have to be considered for this fit: $BR(B^*_{J\,\mathrm{narrow}} \to B^*\pi)$, $BR(B^*_{J\,\mathrm{broad}} \to B^*\pi)$, $BR(B^*_{J\,\mathrm{narrow}} \to B^*\pi\pi)$ and $BR(B^*_{J\,\mathrm{broad}} \to B^*\pi\pi)$. Monte Carlo studies indicate that the sensitivity of the fit to $BR(B^*_{J\,\mathrm{narrow}} \to B^*\pi\pi)$ and $BR(B^*_{J\,\mathrm{broad}} \to B^*\pi\pi)$ is negligible since shape and position of the corresponding peaks in the $B\pi^\pm$ mass spectra are almost the same for the $B^*\pi\pi$ and $B\pi\pi$ final states. The sensitivity to $BR(B^*_{J\,\mathrm{broad}} \to B^*\pi)$ is also smaller than the corresponding sensitivity to $BR(B^*_{J\,\mathrm{narrow}} \to B^*\pi)$ since a larger width but comparable intra-doublet mass splitting of the B_J^* states makes a separation of the decay modes to $B^*\pi$ and $B\pi$ difficult. To reduce the number of fit parameters and to keep the correlations between the fit parameters small, $BR(B^*_{J\,\mathrm{narrow}} \to B^*\pi\pi)/(BR(B^*_{J\,\mathrm{narrow}} \to B^*\pi\pi) + BR(B^*_{J\,\mathrm{narrow}} \to B\pi\pi))$ and $BR(B^*_{J\,\mathrm{broad}} \to B^*\pi\pi)/(BR(B^*_{J\,\mathrm{broad}} \to B^*\pi\pi)+BR(B^*_{J\,\mathrm{broad}} \to B\pi\pi))$ are fixed

to 0.5 in the fit. Furthermore, I require $BR(B^*_{J\,\mathrm{narrow}} \to B^*\pi) = \frac{3}{2} \cdot BR(B^*_{J\,\mathrm{broad}} \to B^*\pi)$ and the fit parameter $BR(B^*_J \to B^*\pi)$ is the weighted mean of both numbers according to the production rates of broad and narrow B^*_J. The factor $\frac{3}{2}$ is based on the assumption of the same production rates for states within the same doublet and $BR(B^*_2 \to B^*\pi)/(BR(B^*_2 \to B^*\pi) + BR(B^*_2 \to B\pi)) = 0.5$.

fit constraint	value
$\frac{BR(B^*_{J_{\mathrm{narrow}}} \to B^*\pi\pi)}{(BR(B^*_{J_{\mathrm{narrow}}} \to B^*\pi\pi) + BR(B^*_{J_{\mathrm{narrow}}} \to B\pi\pi))}$	$\frac{1}{2}$
$\frac{BR(B^*_{J_{\mathrm{broad}}} \to B^*\pi\pi)}{(BR(B^*_{J_{\mathrm{broad}}} \to B^*\pi\pi) + BR(B^*_{J_{\mathrm{broad}}} \to B\pi\pi))}$	$\frac{1}{2}$
$\frac{BR(B^*_{J_{\mathrm{narrow}}} \to B^*\pi)}{BR(B^*_{J_{\mathrm{broad}}} \to B^*\pi)}$	$\frac{3}{2}$

Table 9.2: *Additional fit constraints used in the simultaneous fit .*

With the constraints discussed in the previous paragraph (see also Tables 8.1) and 9.2) and the free parameters: sum of the number of entries of the B^*-enriched and the B^*-depleted signal, $M(B_1(3/2))$, , $(B_1(3/2))$, $M(B^*_0)$, , (B^*_0), $BR(B^*_J \to B^{(*)}\pi\pi)$ and $BR(B^*_J \to B^*\pi)$ I fit the $B\pi^{\pm}$ mass spectra of Figures 9.1c and 9.2c simultaneously. The least squares fit is performed in the $B\pi$ mass region of $5.40 - 6.10$ GeV/c^2 with a bin width of 20 MeV/c^2. The fit results are

$$
\begin{aligned}
M(B_1(3/2)) &= (\,5.738\,^{+\,0.005}_{-\,0.006}\,)\ \mathrm{GeV}/c^2 \\
,\,(B_1(3/2)) &= (\,18\,^{+\,15}_{-\,13}\,)\ \mathrm{MeV}/c^2 \\
M(B^*_0) &= (\,5.839\,^{+\,0.013}_{-\,0.014}\,)\ \mathrm{GeV}/c^2 \qquad (\star) \\
,\,(B^*_0) &= (\,129\,^{+\,27}_{-\,23}\,)\ \mathrm{MeV}/c^2 \qquad (\star) \\
BR(B^*_J \to B^{(*)}\pi\pi) &= 0.245\,^{+\,0.027}_{-\,0.028} \qquad (\star) \\
BR(B^*_J \to B^*\pi) &= 0.74\,^{+\,0.12}_{-\,0.10}
\end{aligned}
$$

where the errors are statistical errors only. The fit has a probability of 65% and the result is presented in Figures 9.4 and 9.5. The numbers agree with the fit results of the fit to the total B^*_J signal and the model independent $BR(B^*_J \to B^*\pi(\pi))$ measurement.

Note that the statistical error of the $BR(B^*_J \to B^*\pi(\pi))$ measurement presented in Subsection 9.1 includes the errors arising from the sideband normalisation. The statistical errors of the fit results on the other hand do not include the sideband normalisation errors. The latter will be discussed in Chapter 11. The $BR(B^*_J \to B^*\pi)$ result of the fit does not include decays to B^* via double pion emission. As done for the fit result of Subsection 8.3 the $BR(B^*_J \to B^{(*)}\pi\pi)$ result is corrected for double counting of the $B^{(*)}\pi^+\pi^-$ final state. In Table 9.3 the correlations between all fit parameters are shown. Numbers with a $(\star)$ should be

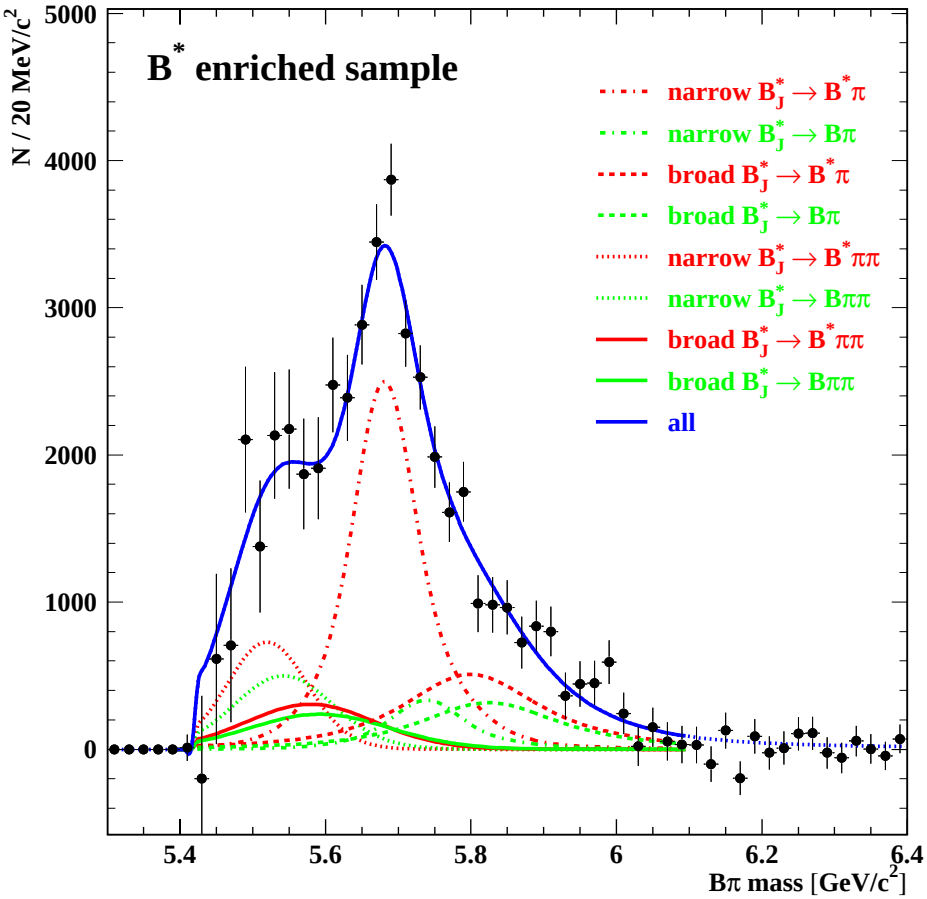

Figure 9.4: *Simultaneous fit to the* $B\pi$ *mass distributions of the* B_J^* *samples enriched or depleted in* $B_J^* \to B^*\pi^{\pm}(\pi)$ *decays (see also Figure 9.5). The fit results of the decays of the broad and narrow* B_J^* *for transitions via one and two pions are presented separately.*

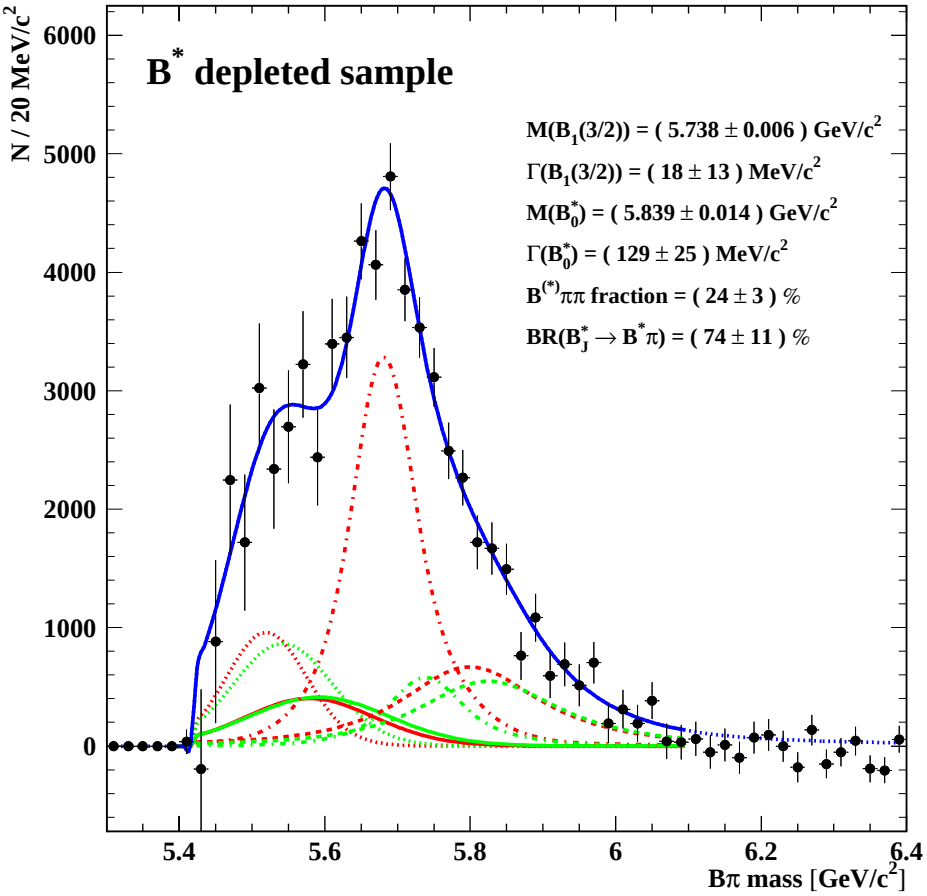

Figure 9.5: *Simultaneous fit to the* Bπ *mass distribution of the* B^*_J *samples enriched or depleted in* $B^*_J \to B^*\pi^\pm(\pi)$ *decays (see also Figure 9.4). The fit results of the decays of the broad and narrow* B^*_J *for transitions via one and two pions are presented separately. In comparison to the fit in Figure 9.4 the fraction of decays to* B^* *is clearly reduced.*

taken with great care because of large systematic errors. The fit shows features very similar to the fit described in Section 8.3. Systematic uncertainties of the fit results are discussed in detail in Section 11.3.

parameter	$N(\mathrm{B}_J^*)$	$M(\mathrm{B}_1)$	, (B_1)	$M(\mathrm{B}_0^*)$	, (B_0^*)	BR(B_J^* $\to \mathrm{B}^{(*)}\pi\pi$)	BR(B_J^* $\to \mathrm{B}^*\pi$)
$N(\mathrm{B}_J^*)$	1.000	0.078	0.349	-0.108	0.418	-0.088	0.114
$M(\mathrm{B}_1(3/2))$	0.078	1.000	0.394	0.028	-0.032	0.067	0.731
, $(\mathrm{B}_1(3/2))$	0.349	0.394	1.000	-0.675	0.355	-0.764	0.791
$M(\mathrm{B}_0^*)$	-0.108	0.028	-0.675	1.000	-0.313	0.741	-0.380
, (B_0^*)	0.418	-0.032	0.355	-0.313	1.000	-0.473	-0.036
BR($\mathrm{B}_J^* \to \mathrm{B}^{(*)}\pi\pi$)	-0.088	0.067	-0.764	0.741	-0.473	1.000	-0.437
BR($\mathrm{B}_J^* \to \mathrm{B}^*\pi$)	0.114	0.731	0.791	-0.380	-0.036	-0.437	1.000

Table 9.3: *Correlations of all free parameters in the simultaneous fit to the data mass spectra of the* B*-*enriched and* B*-*depleted samples.*

Chapter 10

Analysis of the $B\pi^+\pi^-$ Final State

This chapter summarises a search for radially-excited B mesons by reconstructing the $B\pi^+\pi^-$ invariant mass. The main work of this search was carried out by the author of [61] and the analysis details can be found in [61]. This analysis was triggered by a similar preliminary analysis [27, 60] and by the claim for experimental evidence of radially-excited D^* mesons [118] which is not confirmed by other experiments [119, 120, 121].

The goal of this analysis is twofold: first, the search for $B^{(*)\prime} \to B^{(*)}\pi^+\pi^-$ decays. Second, a confirmation of $B_J^* \to B^{(*)}\pi^+\pi^-$ decays. According to the fit results of Sections 8.3 and 9.2, the branching ratio $BR(B_J^* \to B^{(*)}\pi\pi)$ might be quite large.

Inclusively reconstructed B mesons are combined with two charged pions to form $B^{(*)\prime}$ or B_J^* mesons. Due to the large combinatorial background the selection criteria for the pion candidates have to be more stringent with respect to those used in Section 8.1 for the B_J^* reconstruction. After a selection of $Z^0 \to b\overline{b}$ events, B mesons are reconstructed as described in Chapter 6. In each jet containing a B meson candidate, a secondary vertex with a total decay length $L > 0.2$ mm is required.

10.1 $\pi^+\pi^-$ selection

All charged tracks that are well measured according to a standard track selection [110] are considered as possible signal pion candidates if they belong to the same jet as the B candidate. Additionally, the following selection cuts are applied for each pion track:

- The measured ionisation energy loss dE/dx has to be consistent with the expected value for pions, if dE/dx information is available for this track.

- To suppress B decay tracks, the track weight ω_{NN} as described in Section 6.1 has to be smaller than 0.95.

- A minimum track momentum of 0.25 GeV/c^2 is required.

- The opening angle between the jet axis and the pion track has to be smaller than 10°. According to the simulation, this rather loose cut reduces the number of fragmentation pions by a factor of four.

The described (pre-)selection of charged pions is not sufficient to achieve an acceptable signal-to-noise ratio. Therefore, more sophisticated selection criteria are applied by exploiting properties of the di-pion sub-system:

- The two pion tracks are required to have opposite charge.

- For each pair of pion tracks the fit to a common vertex is required to converge. The distance of the di-pion vertex with respect to the primary and to the secondary vertex is calculated.

  - The distance of the di-pion vertex with respect to the primary vertex is required to be smaller than 0.18 mm since the decays of $B^{(*)\prime}$ and B^*_J are strong decays.
  - The distance of the di-pion vertex with respect to the secondary vertex has to exceed 0.30 mm.

  The cut values on the distances of the vertices are chosen to optimise the simulated $B^{(*)\prime}$ signal significance assuming a $B^{(*)\prime}$ production rate of about 5%. Simulation studies indicate that the $B^{(*)\prime}$ selection is not improved by cutting on the decay length significances instead of the total decay length of the vertices.

- The sum of the energies of the B meson and the two pion tracks has to be smaller than 47 GeV (assuming the nominal B and $\pi^\pm$ mass).

- The rapidity y of the di-pion system has to be larger than 2.3 and only jets with a maximum of two di-pion candidates with $y > 2.3$ are considered. This selection criterion has already been used in [27, 60]. The cut value is adjusted to optimise the (Monte Carlo) significance for a $B^{(*)\prime}$ production rate of about 5%.

The efficiency of this $B^{(*)\prime}/B^*_J$ selection varies from 5.0% to 5.3%, depending on the reconstructed invariant mass. The mass resolution is good enough to resolve e.g. two narrow states (, $\simeq$ 25 MeV/c^2) of masses $M(B^*_2) = 5.74$ GeV/c^2 and $M(B') = 5.88$ GeV/c^2.

10.2 $B\pi^+\pi^-$ mass spectrum

The shape of the $B\pi^+\pi^-$ combinatorial background is determined from a data sample of same charge di-pion candidates $B\pi^+\pi^+$. The $B\pi^+\pi^+$ sample composition is slightly different from the $B\pi^+\pi^-$ background because of resonant states like ρ, η, η', ϕ, ω, f_0, ... decaying into $\pi^+\pi^-$(X) only. Also Bose-Einstein correlations have an impact on the shape of the like-sign di-pion sample at low masses. Therefore the $B\pi^+\pi^+$ mass distribution has to be slightly corrected to account for the different background shapes of the like-sign and unlike-sign samples. The correction factor is taken from Monte Carlo and applied bin-by-bin to the $B\pi^+\pi^+$ mass distribution. The corrected $B\pi^+\pi^+$ mass distribution is normalised in the sideband region $6.05 - 7.05$ GeV/c^2 and subtracted from the $B\pi^+\pi^-$ mass distribution. The result is the signal distribution shown in Figure 10.1. The signal is consistent

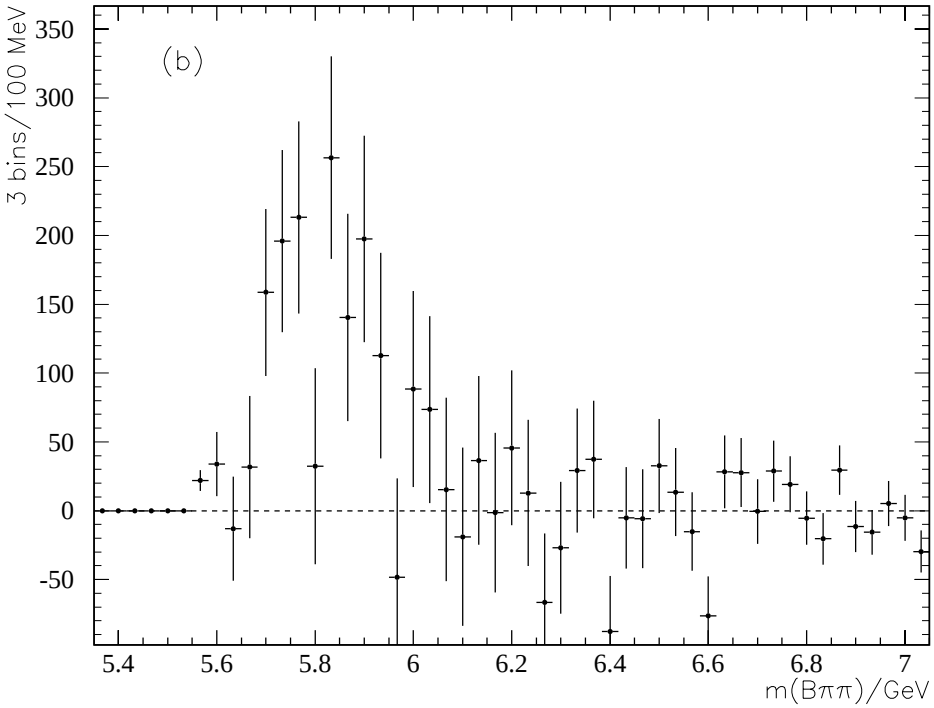

Figure 10.1: *The mass distribution of the background subtracted* $B\pi^+\pi^-$ *signal. A* 3σ *excess is observed in the region of* $5.70 - 5.95$ GeV/c^2. *The signal is interpreted to stem from* $B_J^* \to B^{(*)}\pi\pi$ *and* $B^{(*)\prime} \to B^{(*)}\pi\pi$ *decays. The figure is taken from [61].*

with a superposition of a narrow $B_J^* \to B^{(*)}\pi\pi$ peak at $M(B_J^*) \simeq 5.74$ GeV/c^2 and a broader $B^{(*)\prime} \to B^{(*)}\pi\pi$ peak at $M(B^{(*)\prime}) \simeq 5.85$ GeV/c^2. The dominant contributions to the systematic error on the combinatorial background are uncertainties in the production rates of light meson production, the size of Bose-Einstein correlations and the statistical error due to the sideband normalisation. With the selection efficiency taken from Monte Carlo, a product branching ratio of [61]

$$f(\bar{b} \to B^{(*)\prime}, B_J^*) \cdot BR(B^{(*)\prime}, B_J^* \to B^{(*)}\pi^+\pi^-) = 0.0350 \pm 0.0070 \pm 0.0095 \quad (10.1)$$

is measured where the first error is statistical and the second systematic. The presented number represents the sum of the production rates of $f(\bar{b} \to B')$, $f(\bar{b} \to B^{*\prime})$ and $f(\bar{b} \to B_J^*)$ times the corresponding branching ratios into $B^{(*)}\pi^+\pi^-$. As the observed excess of entries in the $B\pi^+\pi^-$ spectrum is a 3σ effect, the existence of any $B^{(*)\prime}, B_J^* \to B^{(*)}\pi^+\pi^-$ can be questioned and therefore also an upper limit of

$$f(\bar{b} \to B^{(*)\prime}, B_J^*) \cdot BR(B^{(*)\prime}, B_J^* \to B^{(*)}\pi^+\pi^-) < 0.0545 \quad \text{at } 95\% \text{ C.L.} \quad (10.2)$$

is calculated including the statistical and systematic uncertainties.

10.3 Theoretical expectation and other measurements

The masses of B' and $B^{*\prime}$ have been calculated within various models. In [25] for example, $M(B') = 5.883$ GeV/c^2 and $M(B^{*\prime}) = 5.898$ GeV/c^2 is predicted. Single pion and di-pion transitions of the radial excitations to the ground states B and B* are expected to be dominant. The widths of the radially-excited states are expected to be at least 50 MeV/c^2 [1]. The fraction of di-pion transitions contributing to the total width of a B_J^* state is expected to be of the order of several percent, depending on the exact mass of the B_J^* state.

So far there is no rigourous experimental proof for the existence of a $B^{(*)\prime}$ state. Also the decay mode $B_J^* \to B^{(*)}\pi\pi$ is not established yet. A preliminary DELPHI result [27, 60] is so far not confirmed by DELPHI or any other experiment. Also the interpretation of the observed double peak structure in the $B\pi^+\pi^-$ mass spectrum [27, 60] does not give a picture consistent with other B_J^* measurements and theoretical expectations.

The recent 3σ evidence for $B^{(*)\prime} \to B^{(*)}\pi$ claimed by L3 [28] should be taken with great care due to the insufficient treatment of the systematic uncertainties in this analysis.

The OPAL data favour the existence of $B_J^* \to B^{(*)}\pi\pi$ decays according to the observed $B\pi$ and $B\pi\pi$ mass spectra. Including systematic uncertainties (see Chapter 11), the observed B_J^* masses and product branching ratios $f(\bar{b} \to B_J^*) \cdot BR(B_J^* \to B^{(*)}\pi^+\pi^-)$ obtained from the fit to the total $B\pi$ mass spectrum presented in Section 8.3 and from the $B\pi\pi$ mass spectrum are in agreement. Due to the large systematic uncertainties of the former and the rather poor significance of the latter,

[1] To date no reliable calculation of the widths seems to be available.

no rigourous conclusions can be drawn from OPAL data concerning $B^*_J \to B^{(*)}\pi\pi$ decays. The existence of $B^{(*)\prime} \to B^{(*)}\pi\pi$ is supported by OPAL data. Again, the errors are too large to claim a clear $B^{(*)\prime}$ evidence. Because of the rather large errors, the observed $B\pi^+\pi^-$ mass spectrum is consistent with the DELPHI $B\pi^+\pi^-$ signal [27, 60].

In summary, the experimental status of $B^{(*)\prime}$ and $B^*_J \to B^{(*)}\pi\pi$ is rather unclear. The reconstruction of the $B\pi\pi$ final state is quite challenging, the observed results have marginal significance and/or are unconfirmed. The only reliable information that can be extracted from the available experimental data reduces to the statement that the production rate of radially-excited B mesons, B' and $B^{*\prime}$, is small, most likely below 10% per b quark. It is rather unlikely, that the experimental results on $B^{(*)\prime}$ will improve in the next years.

Chapter 11

Systematic Uncertainties

The dominant sources of systematic errors on the measurements presented in Chapters 8, 9 and 10 arise from the $B\pi^{\pm}(\pi^{\mp})$ background, from the reconstruction efficiencies and in the case of the fits also from the implemented fit constraints. In the following subsections, the determination of the systematic uncertainties are presented separately for the fit results of the total B^*_J signal, for the model independent $BR(B^*_J \to B^*\pi(\pi))$ measurement and for the results obtained from the simultaneous fit to the mass spectra with different B^* content. Finally, the systematic uncertainties of the $B^{(*)\prime}$ analysis are listed in Section 11.4.

11.1 Uncertainties of the fit to the total $B\pi^{\pm}$ mass spectrum

All sources of systematic errors are varied in turn within the estimated uncertainty range and the fit presented in Section 8.3 is repeated. If not stated otherwise, the observed deviation with respect to the original fit is taken as a systematic error for each fit parameter. The total systematic error on each fit parameter is the quadratic sum of all individual error contributions. All systematic uncertainties taken into account are listed in Table 11.1. The following paragraphs contain the details of the different error sources.

11.1.1 Variation of fit constraints

The fit constraints are varied according to the present knowledge of D^*_J properties [26] and theoretical considerations [43, 44, 25, 45, 52, 53]:

- The relative production rates $f(b \to B^*_0) : f(b \to B_1(1/2)) : f(b \to B_1(3/2)) : f(b \to B^*_2)$ were fixed to $2 : 2 : 3 : 3$ in the fit, thus assuming the same production rates for partners of the same doublet and a fraction of narrow B^*_J of 0.6. The production rate ratio $f(b \to B_1(3/2))/(f(b \to B_1(3/2)) + f(b \to B^*_2))$ is varied in the range 0.375-0.600, $f(b \to B^*_0)/(f(b \to B^*_0) +$

f(b $\rightarrow$ $B_1(1/2)$) in the range 0.250-0.600 and f_{narrow} in the range 0.5-0.75. These variations cover the different naive production rate estimates of state counting (1:1:1:1) to total spin counting (1:3:3:5).

- Whereas the mass splitting between the $j_q = 1/2$ and $j_q = 3/2$ doublets was free in the fit, the mass splittings within the doublets were fixed. I allow a variation of $M(B_2^*) - M(B_1(3/2)) = (5 - 20)$ MeV/c^2 and $M(B_1(1/2)) - M(B_0^*) = (0 - 50)$ MeV/c^2.

- The ratio of the widths of partners of the same doublet was fixed to , (B_2^*)/ , $(B_1(3/2))$ = 1.25 and , $(B_1(1/2))$/, (B_0^*) = 1.00. I allow a variation of 1.00 – 1.40 for both ratios.

- The constraint $BR(B_2^* \rightarrow B^*\pi) = BR(B_2^* \rightarrow B\pi)$ was used. I allow a variation of $BR(B_2^* \rightarrow B^*\pi)/(BR(B_2^* \rightarrow B^*\pi) + BR(B_2^* \rightarrow B\pi)) = 0.3 - 0.7$ to evaluate the systematic error. Mainly the mass and the width of the narrow states are affected by this variation.

11.1.2 Reconstruction efficiencies

The B_J^* reconstruction efficiency is a function of the reconstructed $B\pi$ mass and the angular distribution of the π. The efficiency is taken from the Monte Carlo and possible problems with its simulation have to be taken into account:

- The signal pion selection cuts have been varied. Whereas the Monte Carlo simulation describes the reconstruction efficiency well at high $B\pi$ masses, this statement can not be proven for low $B\pi$ masses. Since there is also a systematic uncertainty in the determination of the combinatorial background at low masses, the source of a possible mismodelling cannot be assigned unambiguously to one of the two error sources. As a cross check, the fit to the B_J^* signal is performed without an acceptance correction of the mass spectrum as shown in Figure 8.1b. Although the fit result has a low fit probability, I assign half of the total deviations of the fit parameters observed with respect to the original fit as systematic errors. This mainly affects $BR(B_J^* \rightarrow B^{(*)}\pi\pi)$.

- In a B_J^* decay, the helicity angle θ^* is the angle between the signal pion momentum measured in the B_J^* rest frame and the momentum of the B_J^* in the lab frame. The B_0^* and the $B_1(1/2)$ can only decay via S-wave transitions and therefore the corresponding distributions of helicity angle are flat. The angular distributions of the ($B_1(3/2)$, B_2^*) doublet have not yet been measured. Thus each of the B_J^* states has been generated with a flat $\cos\theta^*$ distribution in the simulation. As the signal pion selection acceptance

source	$\Delta M(\mathrm{B}_1(\frac{3}{2}))$ [GeV/c^2]	Δ, $(\mathrm{B}_1(\frac{3}{2}))$ [MeV/c^2]	$\Delta M(\mathrm{B}_0^*)$ [GeV/c^2]	Δ, (B_0^*) [MeV/c^2]	$\Delta\mathrm{BR}(\mathrm{B}_J^* \to \mathrm{B}^{(*)}\pi\pi)$
prod. rate $\mathrm{B}_1(3/2)$ vs. B_2^*	$^{+0.0013}_{-0.0040}$	$^{+0.8}_{-0.9}$	$^{+0.0006}_{-0.0005}$	$+1.$	-0.009
prod. rate B_0^* vs. $\mathrm{B}_1(1/2)$	-0.0001	± 0.0	$+0.0069$	$+1.$	$+0.003$
$\mathrm{f}_{\mathrm{narrow}}$	$^{+0.0002}_{-0.0001}$	$^{+9.4}_{-14.3}$	$^{+0.0130}_{-0.0154}$	$^{+8.}_{-12.}$	$^{+0.020}_{-0.017}$
$M(\mathrm{B}_2^*) - M(\mathrm{B}_1(3/2))$	$^{+0.0025}_{-0.0026}$	$^{+3.9}_{-5.6}$	$^{+0.0044}_{-0.0030}$	$-1.$	$^{+0.011}_{-0.007}$
$M(\mathrm{B}_1(1/2)) - M(\mathrm{B}_0^*)$	± 0.0004	± 0.1	$^{+0.0105}_{-0.0161}$	$^{+2.}_{-6.}$	$^{+0.005}_{-0.007}$
, (B_2^*)/, $(\mathrm{B}_1(3/2))$	$^{+0.0003}_{-0.0005}$	$^{+1.7}_{-0.9}$	± 0.0002	$\pm 1.$	-0.001
, $(\mathrm{B}_1(1/2))$/, (B_0^*)	$+0.0003$	$+0.5$	-0.0020	$-19.$	-0.002
$\mathrm{BR}(\mathrm{B}_2^* \to \mathrm{B}^*\pi/\mathrm{B}\pi)$	$^{+0.0038}_{-0.0047}$	$^{+6.8}_{-4.3}$	$^{+0.0027}_{-0.0048}$	$-1.$	$^{+0.002}_{-0.009}$
efficiency $f(M(\mathrm{B}\pi))$	± 0.0025	± 7.1	± 0.0027	$\pm 10.$	± 0.088
efficiency $f(\cos\theta^*)$	$^{+0.0003}_{-0.0001}$	$^{+9.5}_{-9.9}$	$^{+0.0131}_{-0.0127}$	$^{+9.}_{-12.}$	$^{+0.014}_{-0.017}$
udsc bg modelling	± 0.0002	± 0.7	± 0.0018	$\pm 3.$	± 0.003
b fragm. bg modelling	± 0.0011	± 6.1	± 0.0107	$\pm 31.$	± 0.007
B decay bg modelling	± 0.0011	± 16.1	± 0.0092	$\pm 28.$	± 0.010
udsc bg fraction	± 0.0001	± 0.4	$^{+0.0008}_{-0.0007}$	$\pm 1.$	± 0.002
b fragm. bg fraction	$^{+0.0004}_{-0.0010}$	$^{+3.0}_{-1.9}$	$^{+0.0053}_{-0.0077}$	$^{+11.}_{-8.}$	$^{+0.040}_{-0.059}$
B decay bg fraction	$^{+0.0006}_{-0.0009}$	$^{+1.4}_{-1.1}$	$^{+0.0076}_{-0.0073}$	$\pm 6.$	$^{+0.050}_{-0.051}$
Peterson fragmentation	$^{+0.0010}_{-0.0012}$	$^{+17.0}_{-14.0}$	$^{+0.0049}_{-0.0061}$	$^{+37.}_{-30.}$	$^{+0.046}_{-0.061}$
sideband normalisation	± 0.0002	± 3.0	$^{+0.0047}_{-0.0049}$	$\pm 7.$	$^{+0.004}_{-0.005}$
sideband range variation	$^{+0.0001}_{-0.0002}$	$^{+2.0}_{-4.9}$	$^{+0.0027}_{-0.0064}$	$^{+5.}_{-12.}$	$^{+0.002}_{-0.005}$
background fit function	± 0.0015	± 1.8	± 0.0047	$\pm 2.$	± 0.004
B_{sJ}^* contamination	± 0.0013	$^{+1.2}_{-1.1}$	$^{+0.0032}_{-0.0036}$	$\pm 5.$	-0.001
$\mathrm{B}^{(*)\prime}$ contamination	$^{+0.0075}_{-0.0064}$	-14.3	$^{+0.0163}_{-0.0047}$	$-25.$	-0.035
variation of bin width	$^{+0.0003}_{-0.0013}$	$^{+5.1}_{-0.1}$	$^{+0.0054}_{-0.0356}$	$^{+6.}_{-29.}$	$^{+0.018}_{-0.069}$
variation of fit range	$+0.0001$	$^{+2.4}_{-2.1}$	$^{+0.0008}_{-0.0007}$	$^{+11.}_{-9.}$	± 0.007
total	± 0.010	$^{+31.}_{-34.}$	$^{+0.035}_{-0.049}$	$^{+62.}_{-73.}$	$^{+0.124}_{-0.157}$

Table 11.1: *Systematic errors on the fit parameters of the fit to the total* B_J^* *signal described in Section 8.3. The numbers for* $\Delta\mathrm{BR}(\mathrm{B}_J^* \to \mathrm{B}^{(*)}\pi\pi)$ *have to be multiplied by 0.75 to account for double counting (see also Section 8.3). The total systematic error of of each fit parameter is the quadratic sum of the individual errors.*

depends on $\cos\theta^*$, the B_J^* efficiency is sensitive to the shape of $\cos\theta^*$. According to [122] the $B_1(3/2)$ and the B_2^* are expected to have the same $\cos\theta^*$ distribution for any initial b polarisation:

$$\frac{1}{,}\frac{\mathrm{d},}{\mathrm{d}\cos\theta^*}(B_1(3/2), B_2^* \to B, B^*\pi) = \frac{1}{4}\left(1 + 3\cos^2\theta^* - 6w_{3/2}(\cos^2\theta^* - \frac{1}{3})\right) \tag{11.1}$$

where $w_{3/2}$ is the probability that fragmentation leads to a state with the maximum helicity value of 3/2 for the light degrees of freedom. The value of $w_{3/2}$ is not predicted by theory. Therefore, the Monte Carlo $\cos\theta^*$ distributions of $B_1(3/2)$ and B_2^* have been reweighted to cover the whole range $w_{3/2} = 0 - 1$.

11.1.3 Background related uncertainties

A proper understanding of the combinatorial $B\pi$ background is an important task for any B_J^* analysis. While some measurements determine the shape of the background using like-sign combinations of charged B mesons and pions [58, 56], others rely heavily [59, 57] or completely [28] on Monte Carlo predictions. In the case of the former, the results suffer from low statistics while the later has to cope with the problem of evaluating the size of systematic uncertainties. In order to maintain high statistics and to allow a serious test of the Monte Carlo background, a new method is used for this analysis. For the determination of the systematic errors on the fit parameters, the simulated $B\pi$ background is varied using the methods described below. For each variation, the Monte Carlo background is normalised and subtracted from the data and the obtained B_J^* signal distribution is fitted.

- Data test samples are developed in which individual background sources are substantially enhanced to allow detailed studies of the $B\pi^{\pm}$ combinatorial background. The background is divided into three different classes: tracks combined with mistagged B candidates in light and charm quark events (udsc flavour), b hadron decay tracks combined with true b hadrons (b hadron decay) and b fragmentation tracks combined with true b hadrons (b fragmentation). Since the quality of the Monte Carlo background modelling may be different for different kinematical regions, the selection criteria of each test sample are chosen to cover a large fraction of the kinematical region of the signal pion selection. Furthermore, a purity of at least 90% for the background source under study and a B_J^* signal fraction smaller than 1.5% is demanded. These requirements are achieved by inverting cuts of the original B_J^* selection. For each test sample, the $B\pi^{\pm}$ invariant mass distribution observed in data is compared with the corresponding Monte Carlo distribution normalised to the same number of selected B candidates. Since the light and charm quark sample described above does not have the same charm quark content as the non-b background of the B_J^* signal selection,

an additional cross check is performed. Charm events are tagged using reconstructed D^{*+} candidates in five different decay channels, as described in [123]. This results in a sample with the same composition of light flavour and charm flavour as in the B^*_J signal selection and less than 10% b flavour. The observed Monte Carlo deviation in the $B\pi^{\pm}$ mass spectrum of this D^{*+} sample is consistent with the deviation seen in the first test sample. Due to the low statistics of the D^{*+} sample only the sample described first is used. The mass distributions and their bin-by-bin ratios data/Monte Carlo are shown in Figure 11.1. The different ratios are fitted with simple polynomials. The latter are used to correct the shape of the original Monte Carlo $B\pi^{\pm}$ mass distributions for each background source separately. The systematic uncertainty on each background source is given by the difference between the corrected and the uncorrected shape of the $B\pi^{\pm}$ mass distribution. To evaluate the systematic uncertainties on the fit results, the three background sources are varied in turn according to the procedure explained above.

- The composition of the $B\pi^{\pm}$ background, as seen in Monte Carlo after the corrections have been applied, is varied. The fraction of each of the three background sources described earlier is varied by $\pm 20\%$.

- The Peterson fragmentation parameter ϵ_b has been varied in the range $0.0028 - 0.0057$ to cover uncertainties in the average fraction of the beam energy carried by the weakly decaying b hadron, $\langle x_E \rangle$, and in the shape of the fragmentation function. This variation causes a change in the $B\pi^{\pm}$ background shape.

- The charged particle multiplicity of weakly decaying b hadrons is considered as a source of systematic uncertainty on the $B\pi^{\pm}$ background. The average charged multiplicity including K^0 and Λ decay products is varied in the range $5.375 - 5.865$ in the simulation (see [124, 125, 126]). The observed effect on the $B\pi^{\pm}$ background shape results in a negligible change of the fit results.

- The Monte Carlo background is normalised to the data in the upper sideband region of the $B\pi$ mass spectrum. Due to the limited data statistics, a relative error of about 0.6% on the normalisation factor has to be taken into account. The size of the background is thus varied by $\pm 0.6\%$ in total.

- The range of the sideband used for the background normalisation is varied by ± 100 MeV/c^2 on each side and the observed deviations are added in quadrature.

- To evaluate the uncertainty due to the function used to fit the Monte Carlo background, I directly subtract the corrected Monte Carlo background histogram of the $B\pi$ mass distribution from the corresponding data histogram.

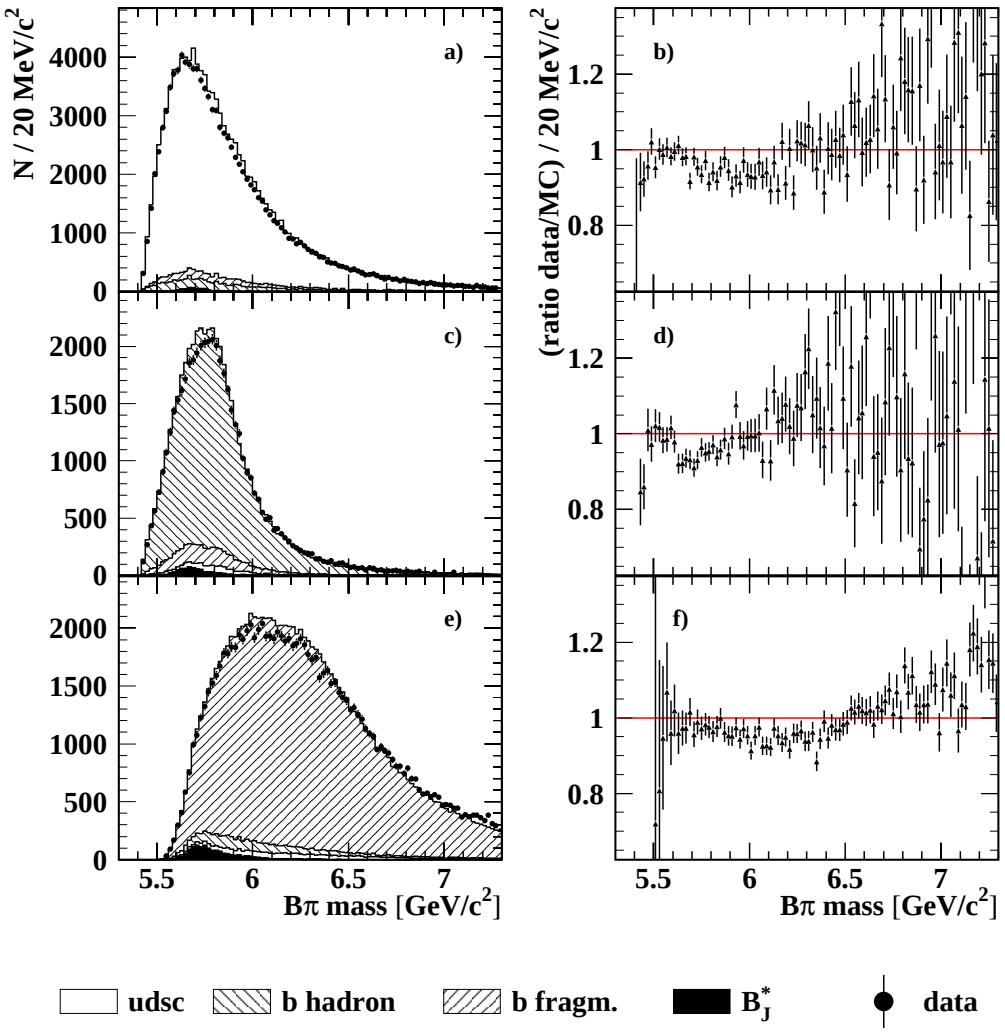

Figure 11.1: *The* Bπ± *mass distributions of data and Monte Carlo for each of the three test samples (left side) and the corresponding bin-by-bin ratio of the mass distributions (right side). a)+b) Light and charm quark sample, c)+d)* b *hadron decay sample, e)+f)* b *fragmentation sample.*

11.1.4 Contamination of the B_J^* signal and other uncertainties

I take into account possible contributions to the B_J^* signal from other excited states and vary the bin width and the fit range.

- Reflections from B_{sJ}^* decays influence the fit results since a small fraction of kaons are misidentified as pions. As calculated from Monte Carlo, the amount of B_{sJ}^* seen in the B_J^* peaks is less than 4% for a B_{sJ}^* production rate consistent with [56]. Since the pion mass has been assumed to calculate the invariant mass, these misidentified $BK^{\pm}$ combinations produce a broad peak around $M_{B\pi} = 5.6$ GeV/c^2. The B_{sJ}^* production rate is varied by $\pm 50\%$ which covers the experimental error [56] and the fit of the B_J^* signal is repeated.

- Contributions from radial excitations of B mesons decaying to $B^{(*)}\pi$ or $B^{(*)}\pi\pi$ may be contained in the B_J^* signal peak. There is some experimental evidence for $B^{(*)\prime} \to B^{(*)}\pi\pi$ transitions [27, 60]. Two Monte Carlo sets of radially-excited B mesons are generated in the decay channels $B' \to B\pi^+\pi^-$ and $B^{*\prime} \to B^*\pi^+\pi^-$. The states are produced with masses $M(B') = 5.883$ GeV/c^2 and $M(B^{*\prime}) = 5.898$ GeV/c^2 according to the theoretical expectation [25] and in agreement with [27, 60]. The radial excitations are generated with widths of value zero, which is strongly supported by the experimental result[27, 60]. According to the Monte Carlo, these $B^{(*)\prime} \to B^{(*)}\pi\pi$ decays cause a peak at 5.6 GeV/c^2 in the $B\pi^{\pm}$ mass distribution. With the total B' production rate observed in [27, 60], the B_J^* peak of Figure 8.1 does not contain more than 3% $B^{(*)\prime} \to B^{(*)}\pi\pi$ transitions. The calculated $B^{(*)\prime}$ contamination is subtracted from the $B\pi$ mass spectrum and the fit to the modified B_J^* signal is repeated. Also evidence for $B^{(*)}\pi$ decays has been claimed recently [28]. Although there is no evidence for such a state in OPAL data, I implement the measured production rate, mass and width of the observed state and refit the signal. The total change of the fit parameters is taken as a systematic error. The inclusion of $B^{(*)\prime}$ in the fit has a considerable effect on the masses and widths of the different B_J^* states.

- The whole analysis is repeated using bin widths of 16 and 25 MeV/c^2 instead of 20 MeV/c^2.

- The range of the fit region is changed by ± 80 MeV/c^2 on both sides.

11.1.5 The rôle of $BR(B_J^* \to B^{(*)}\pi\pi)$ in the fit

Extensive systematic studies have been performed to test the stability of the fit results. According to the numbers presented in Table 11.1, the systematic error on $BR(B_J^* \to B^{(*)}\pi\pi)$ is large, mainly due to the uncertainties in selection efficiency and background near the $B\pi$ threshold. Consequently, the existence of $B_J^* \to$

$B^{(*)}\pi\pi$ can be questioned and the fit is repeated with $BR(B_J^* \to B^{(*)}\pi\pi) = 0$. To further test the robustness of the fit, the functional form of the broad B_J^* states at $B\pi$ threshold - which is not precisely known - has been varied assuming different theoretical approaches. It turns out that the fit probability for any fit with $BR(B_J^* \to B^{(*)}\pi\pi)$ fixed to zero is always below 2% (to be compared with a fit probability of 33% of the original fit). Depending on the functional form of the broad B_J^* states, the mass of the B_0^* lies below or above the $B_1(3/2)$ mass for $BR(B_J^* \to B^{(*)}\pi\pi) = 0$. Because of this ambiguity, the widths and the mass of the B_0^* as well as $BR(B_J^* \to B^{(*)}\pi\pi)$ are not quoted as robust fit results. The mass and the widths of the $B_1(3/2)$ stays stable for all fits. In comparison to other measurements, especially [107], this is a rather conservative treatment of the fit. Other experiments are expected to have very similar problems in determining B_J^* properties from a fit to a single $B\pi$ mass peak.

11.2 Uncertainties of the BR($B_J^* \to B^* \pi(\pi)$) measurement

The main sources of systematic error on $BR(B_J^* \to B^*\pi(\pi))$ are uncertainties in the efficiency ratios, uncertainties in the modelling of the combinatorial $B\pi^{\pm}$ background and systematic errors on the sideband normalisation of the B^*-enriched and B^*-depleted samples. Each contribution to the total error on $BR(B_J^* \to B^*\pi(\pi))$ is listed in Table 11.2 and discussed in the following subsections.

11.2.1 Reconstruction efficiency

For the determination of $BR(B_J^* \to B^*\pi(\pi))$, the Monte Carlo simulation is used to calculate the efficiency ratios e, e^* and e_0. The systematic errors on these ratios are dominated by uncertainties in the photon reconstruction. The simulation is checked against data using known properties of B^* and π^0. The latter are formed by a pairwise combination of two good conversion candidates or one good conversion and one good calorimeter candidate assigned to the same B candidate.

- In both the calorimeter and conversion samples the positions of both the B^* signal peak and the π^0 peak in the data are duplicated within the statistical errors by the Monte Carlo simulation. The simulated shape of the peaks agrees well with the shape observed in data. The contribution to the branching fraction measurement arising from statistical uncertainties on the fits to the B^* signal peak, and on the difference between the reconstructed and generated B^* mass in the simulation are quantified by adjusting the mass to the current world average [26] and systematically shifting it to higher and lower values. For the conversion sample, a shift of ± 1.0 MeV/c^2 in the B^* peak position is made, but since the cut on $\mathcal{W}(B^*)$ is such that all conversion

candidates with a $M_{\mathrm{B}\gamma}$ mass in the M_{B^*} region are selected, the resulting effect on $\mathrm{BR}(\mathrm{B}_J^* \to \mathrm{B}^*\pi(\pi))$ is negligible. For the calorimeter photon sample a shift of ± 2.0 MeV/c^2 in the B^* peak position is made.

- The number of B^* and π^0 candidates found in the corresponding mass peaks of the conversion sample has been compared with the corresponding results from the Monte Carlo simulation. The observed yields agree within the statistical error of 5%. The production rates of B^* and π^0 have been measured with a relative precision of 5.3% and 2.9% [26], respectively, and the corresponding JETSET rates are in agreement with these measurements. To account for the quoted uncertainties, the calculation of efficiency ratios is repeated on Monte Carlo with the reconstruction efficiency of conversion photons in the decay $\mathrm{B}^* \to \mathrm{B}\gamma$ changed by $\pm 10\%$.

  After the subtraction of the Monte Carlo background, the yield of B^* candidates in the calorimeter sample is greater in data than in the Monte Carlo sample. The efficiency for calorimeter photons from B^* or the Monte Carlo background in the B^* signal region is underestimated. Since the source of the discrepancy cannot be assigned unambiguously, the Monte Carlo efficiency for calorimeter photons of the decay $\mathrm{B}^* \to \mathrm{B}\gamma$ is varied by a factor of 0.9 to 1.15, the lower value being consistent with the corresponding uncertainty assigned in the conversion sample and the factor 1.15 covering the observed B^* yield in data.

- The number of good calorimeter photon candidates (Figure 7.4b) is not modelled well in the simulation. Therefore, the Monte Carlo distribution is reweighted to the corresponding data distribution. The reweighting clearly improves the general agreement between data and Monte Carlo and has an impact on the efficiency rations e, e^* and e_0. The central value of $\mathrm{BR}(\mathrm{B}_J^* \to \mathrm{B}^*\pi(\pi))$ changes by -0.059 due to the reweighting. To quantify the uncertainty in the reweighting procedure I take half of the total change of the central value as the error on $\mathrm{BR}(\mathrm{B}_J^* \to \mathrm{B}^*\pi(\pi))$.

- As described in Subsection 11.1.2, the unknown $\cos\theta^*$ distributions of B_2^* and $\mathrm{B}_1(3/2)$ produce uncertainties in the reconstruction efficiencies. The Monte Carlo $\cos\theta^*$ distributions of $\mathrm{B}_1(3/2)$ and B_2^* have been reweighted to cover the whole range $w_{3/2} = 0 - 1$.

- The mass dependent efficiency correction of the B_J^* signal of both the B^*-enriched and B^*-depleted samples produces a deviation in $\mathrm{BR}(\mathrm{B}_J^* \to \mathrm{B}^*\pi(\pi))$ (see also Subsection 11.1.2). To account for any mismodelling in the simulated mass dependence of the efficiency, half of this deviation is taken as the systematic error.

- The limited Monte Carlo statistics cause uncertainties in the calculated efficiency ratios.

source	range	$\Delta(\mathrm{BR}(B_J^* \to B^*\pi(\pi)))$
reconstructed B^* mass (ECAL)	± 2 MeV/c^2	$+0.007\ -0.005$
B^* efficiency ($\gamma \to e^+e^-$) variation	$[0.90, 1.10]$	$+0.019\ -0.018$
B^* efficiency (ECAL) variation	$[0.90, 1.15]$	$+0.036\ -0.047$
reweighting of $N_{\gamma_{\mathrm{ECAL}}}$		± 0.030
$\cos\theta^*$ dependency	$w_{3/2} \in [0, 1]$	$+0.040\ -0.034$
$M_{B\pi}$ dependence of B_J^* efficiency		± 0.018
statistical error on efficiency ratios	$\approx 1\%$	± 0.018
udsc tracks background modelling	corr. on/off	± 0.002
B decay tracks background modelling	corr. on/off	± 0.017
b fragmentation tracks background modelling	corr. on/off	± 0.005
relative composition of background sources	$\pm 20\%$	$+0.027\ -0.037$
sideband range variation	± 100 MeV/c^2	$+0.076\ -0.057$
track parameter resolution variation	$\pm 10\%$	< 0.010
variation of cuts on $\mathcal{W}(B^*)$		$+0.030\ -0.043$
B_{sJ}^* reflections		$+0.006\ -0.026$
$B^{(*)\prime}$ reflections		$+0.000\ -0.017$
total		± 0.12

Table 11.2: *Systematic errors of the* $\mathrm{BR}(B_J^* \to B^*\pi(\pi))$ *measurement. Detailed information for each uncertainty is given in the text, as well as a discussion of uncertainties which are negligible and thus excluded from this table.*

11.2.2 Combinatorial $B\pi^\pm$ background

Uncertainties in the shape of the simulated background have an impact on the number of signal candidates N_{E} and N_{D}. Since the combinatorial backgrounds in both the B^*-enriched and the B^*-depleted samples are affected by systematic shifts in a similar way, the measurement is expected to be rather robust against possible uncertainties in the Monte Carlo background simulation. The cut value for $\mathcal{W}(B^*)$ is chosen to minimise the resulting error on $\mathrm{BR}(B_J^* \to B^*\pi(\pi))$ (see Chapter 9).

- For the determination of the background shape, the same method as presented in Subsection 11.1.3 is used. All test samples and background corrections described are obtained using the full B_J^* sample but applied to the background distributions of the B^*-enriched and B^*-depleted sample, since it is assumed that the B^* selection does not affect a possible mismodelling of the Monte Carlo $B\pi^\pm$ background. The systematic uncertainty on each background source is given by the difference between the corrected and the uncorrected shape of the $B\pi^\pm$ mass distribution.

- The composition of the $B\pi^\pm$ background, as seen in Monte Carlo after the corrections have been applied, is varied for each source. The fraction of each of the three background sources described earlier is varied by $\pm 20\%$.

- The Peterson fragmentation parameter ϵ_b has been varied as described in Subsection 11.1.3. The effect on $BR(B_J^* \to B^*\pi(\pi))$ is smaller than 0.002.

- The charged particle multiplicity of weakly decaying b hadrons is considered as a source of systematic uncertainty as described in Subsection 11.1.3. The observed effect on th $B\pi^\pm$ background shape results in an error on $BR(B_J^* \to B^*\pi(\pi))$ smaller than 0.002.

11.2.3 Other sources of systematic uncertainties and consistency checks

The following systematic studies have been performed in addition to the studies described in Subsections 11.2.1 and 11.2.2.

- The range of the sideband used for the background normalisation is varied by ± 100 MeV/c^2 on each side for both the B*-enriched and B*-depleted sample. The quadratic sum of the differences observed in the number of signal entries gives the corresponding error.

- To account for any uncertainties arising from a wrongly simulated tracking resolution, the reconstructed track parameters are smeared by $\pm 10\%$ in the Monte Carlo.

- The cuts of the signal pion selection have been varied. No systematic deviations are observed.

- The cut on $\mathcal{W}(B^*)$ has been varied. Only cuts producing samples with high statistics and with the ratio of signal-to-background ratios in the $B\pi$ mass spectra of the B*-enriched and B*-depleted samples being close to 1 have been considered. The observed deviations in $BR(B_J^* \to B^*\pi(\pi))$ do not exceed $^{+0.030}_{-0.043}$ which is taken as the systematic error due to the cut on $\mathcal{W}(B^*)$.

- The amount of B_{sJ}^* seen in the B_J^* peaks is less than 4% for a B_{sJ}^* production rate consistent with [56]. The branching ratio $BR(B_{sJ}^* \to B^*K)$ is varied from 0.2 to 1.0 in the simulation to evaluate the corresponding error.

- Contributions from higher orbital or radial excitations of B mesons decaying to $B^{(*)}\pi$ or $B^{(*)}\pi\pi$ may be contained in the signal peaks of the B*-enriched and the B*-depleted samples. A special set of simulated $B^{(*)\prime}$ decays is used to evaluate systematic uncertainties on $BR(B_J^* \to B^*\pi(\pi))$ (see Subsection 11.1.4). Although the production rates for B′ and B*′ are expected to be rather similar, the fraction of B*′ of both radial excitations is varied from 0.3 to 0.7.

- The whole analysis is repeated using conversion photons only and calorimeter photons only. The obtained branching ratio results and the $B_J^* \to B^*\pi^\pm(\pi)$

and $B^*_J \to B\pi^{\pm}(\pi)$ mass distributions are in agreement with each other and with the total sample.

- Different cuts on $\mathcal{B}_{\text{event}}$ are applied and the whole analysis is repeated, resulting in a change of the b purity from 92% to 98%. No systematic deviation of $BR(B^*_J \to B^*\pi(\pi))$ is observed.

- A neural network has been trained to replace the weight $\mathcal{W}(B^*)$ obtained from the Monte Carlo purity parameterisation. The neural network output is strongly correlated with the weight $\mathcal{W}(B^*)$ but does not improve the B^*/B separation.

11.3 Uncertainties of the simultaneous fit

Almost all sources of systematic error contributing to the results of the simultaneous fit to the $B\pi$ mass spectra of Figures 9.4 and 9.5 have already been listed in Subsections 11.1 and 11.2. Therefore I mention only error contributions not discussed earlier and methods of error determination that differ from the methods used before. A full list of systematic errors for the fit results is given in Table 11.3.

- The fit constraints for the simultaneous fit have been varied in the same ranges as for the fit to the total $B\pi$ mass distribution (see Subsection 11.1.1). In addition to these fit constraints, two additional assumptions related to $BR(B^*_J \to B^*\pi)$ were made in the simultaneous fit. The ratio $BR(B^*_J \to B^*\pi\pi)/(BR(B^*_J \to B^*\pi\pi) + BR(B^*_J \to B\pi\pi))$, which was fixed to 0.5, is varied in the range 0.3-0.7. No significant deviation in the fit parameters is observed, since the position and shape of the peaks corresponding to the two final states are very similar. Also $BR(B^*_{J\,\text{broad}} \to B^*\pi)$ was fixed to $\frac{2}{3} \cdot BR(B^*_{J\,\text{narrow}} \to B^*\pi)$. As a systematic study, this constraint is changed to $BR(B^*_{J\,\text{broad}} \to B^*\pi) = BR(B^*_{J\,\text{narrow}} \to B^*\pi)$ and the corresponding deviations of the fit parameters are taken as systematic errors.

- The uncertainties due to the limited data statistics in the upper sideband regions of the B^*-enriched and B^*-depleted samples produce quite large error contributions on $BR(B^*_J \to B^*\pi)$. For the fit results, these error contributions are treated as systematic errors and have to be compared with the corresponding errors obtained for the model independent $BR(B^*_J \to B^*\pi)$ measurement. For the latter, the error contributions from the sidebands are substantially larger due to the different method of the measurement (see Formula 9.4) and the missing constraints.

- The same ambiguity as described in Section 11.1.5 holds for the simultaneous fit if $BR(B^*_J \to B^{(*)}\pi\pi)$ is set to zero. The implications are the same and therefore the width and the mass of B^*_0 cannot be determined from the fit.

source	ΔBR(B_J^* $\to B^*\pi$)	$\Delta M(B_1(\frac{3}{2}))$ [GeV/c^2]	Δ, ($B_1(\frac{3}{2})$) [MeV/c^2]	$\Delta M(B_0^*)$ [GeV/c^2]	Δ, (B_0^*) [MeV/c^2]	ΔBR(B_J^* $\to B^{(*)}\pi\pi$)
prod. rate $B_1(\frac{3}{2})$ vs. B_2^*	± 0.012	$^{+0.0015}_{-0.0021}$	± 1.2	$^{+0.0000}_{-0.0022}$	$\pm 1.$	$^{+0.003}_{-0.006}$
prod. rate B_0^* vs. $B(\frac{1}{2})$	$^{+0.004}_{-0.003}$	$^{+0.0001}_{-0.0002}$	± 0.0	$^{+0.0060}_{-0.0054}$	$^{+1.}_{-2.}$	$^{+0.003}_{-0.002}$
f_{narrow}	$^{+0.049}_{-0.028}$	$^{+0.0001}_{-0.0002}$	$^{+7.9}_{-8.9}$	$^{+0.0144}_{-0.0199}$	$\pm 12.$	$^{+0.001}_{-0.008}$
$M(B_2^*) - M(B_1(3/2))$	$^{+0.003}_{-0.002}$	± 0.0024	$^{+2.4}_{-3.2}$	$^{+0.0017}_{-0.0010}$	$\pm 2.$	$^{+0.003}_{-0.002}$
$M(B_1(1/2)) - M(B_0^*)$	± 0.001	± 0.0001	$^{+0.0}_{-0.2}$	$^{+0.0119}_{-0.0200}$	$^{+5.}_{-6.}$	$^{+0.007}_{-0.012}$
, (B_2^*)/, $(B_1(3/2))$	$^{+0.014}_{-0.009}$	$^{+0.0008}_{-0.0013}$	$^{+4.1}_{-1.9}$	$^{+0.0001}_{-0.0029}$	$^{+2.}_{-0.}$	$^{+0.007}_{-0.016}$
, $(B_1(1/2))$/, (B_0^*)	$+0.001$	$+0.0004$	$+0.5$	-0.0030	$-20.$	-0.004
BR($B_2^* \to B^*\pi/B\pi$)	$^{+0.013}_{-0.008}$	$^{+0.0012}_{-0.0004}$	$^{+2.4}_{-1.2}$	$^{+0.0043}_{-0.0075}$	$^{+3.}_{-2.}$	$^{+0.012}_{-0.017}$
BR($B^*_{J\,\mathrm{broad}} \to B^*\pi$)	$+0.059$	-0.0015	-4.8	$+0.0097$	$+1.$	$+0.011$
efficiency $f(M(B\pi))$	± 0.039	± 0.0018	± 4.3	-0.0050	$\pm 1.$	± 0.109
efficiency $f(\cos\theta^*)$	$^{+0.002}_{-0.001}$	$^{+0.0001}_{-0.0002}$	$^{+4.1}_{-5.0}$	$^{+0.0077}_{-0.0103}$	$^{+6.}_{-7.}$	$^{+0.002}_{-0.004}$
udsc bg modelling	± 0.005	± 0.0000	± 0.4	± 0.0019	$\pm 3.$	± 0.002
b fragm. bg modelling	± 0.025	± 0.0002	± 4.7	± 0.0104	$\pm 33.$	± 0.007
B decay bg modelling	± 0.016	± 0.0012	± 13.4	± 0.0111	$\pm 25.$	± 0.002
udsc bg fraction	± 0.023	$^{+0.0001}_{-0.0000}$	± 0.5	± 0.0007	$\pm 0.$	± 0.002
b fragm. bg fraction	$^{+0.030}_{-0.028}$	$^{+0.0003}_{-0.0004}$	$^{+5.7}_{-4.4}$	$^{+0.0060}_{-0.0084}$	$^{+10.}_{-8.}$	$^{+0.042}_{-0.061}$
B decay bg fraction	$^{+0.037}_{-0.044}$	$^{+0.0001}_{-0.0008}$	$^{+4.7}_{-5.0}$	$^{+0.0089}_{-0.0082}$	$^{+4.}_{-6.}$	± 0.054
Paterson fragmentation	$^{+0.034}_{-0.059}$	$^{+0.0010}_{-0.0008}$	$^{+22.3}_{-16.4}$	$^{+0.0044}_{-0.0047}$	$^{+35.}_{-27.}$	$^{+0.046}_{-0.065}$
sideband norm. B^*-enr.	$^{+0.125}_{-0.071}$	$^{+0.0041}_{-0.0032}$	$^{+15.0}_{-9.3}$	$^{+0.0013}_{-0.0020}$	$^{+3.}_{-6.}$	$^{+0.017}_{-0.010}$
sideband norm. B^*-dep.	$^{+0.116}_{-0.067}$	$^{+0.0031}_{-0.0025}$	$^{+9.6}_{-4.5}$	$^{+0.0075}_{-0.0081}$	$^{+4.}_{-9.}$	$^{+0.014}_{-0.022}$
sideb. range variation	$^{+0.032}_{-0.030}$	$^{+0.0012}_{-0.0011}$	$^{+3.9}_{-5.2}$	$^{+0.0037}_{-0.0064}$	$^{+5.}_{-13.}$	$^{+0.005}_{-0.007}$
B^*_{sJ} contamination	± 0.021	$^{+0.0002}_{-0.0004}$	± 2.7	$^{+0.0042}_{-0.0043}$	$\pm 4.$	$^{+0.004}_{-0.005}$
$B^{(*)\prime}$ contamination	$^{+0.026}_{-0.028}$	$^{+0.0003}_{-0.0002}$	$^{+3.5}_{-3.7}$	$^{+0.0055}_{-0.0044}$	$^{+4.}_{-5.}$	± 0.003
background fit function	± 0.023	± 0.0025	± 0.6	± 0.0055	$\pm 6.$	± 0.005
variation of bin width	$^{+0.009}_{-0.005}$	$^{+0.0010}_{-0.0008}$	$^{+5.0}_{-3.5}$	$^{+0.0044}_{-0.0076}$	$^{+5.}_{-16.}$	$^{+0.017}_{-0.033}$
variation of fit range	± 0.002	$^{+0.0001}_{-0.0000}$	$^{+2.0}_{-1.7}$	$^{+0.0009}_{-0.0006}$	$^{+11.}_{-10.}$	$^{+0.010}_{-0.006}$
stat. error on e, e_0, e^*	$^{+0.003}_{-0.009}$	$^{+0.0003}_{-0.0000}$	$^{+0.2}_{-0.8}$	$^{+0.0005}_{-0.0010}$	$\pm 1.$	$^{+0.000}_{-0.001}$
B^* eff. ($\gamma \to e^+e^-$)	$^{+0.003}_{-0.008}$	$^{+0.0003}_{-0.0000}$	$^{+0.3}_{-0.8}$	$^{+0.0005}_{-0.0011}$	$\pm 1.$	$^{+0.000}_{-0.001}$
B^* efficiency (ECAL)	$^{+0.013}_{-0.023}$	$^{+0.0007}_{-0.0005}$	$^{+1.3}_{-2.3}$	$^{+0.0004}_{-0.0016}$	$+1.$	± 0.003
rec. B^* mass (ECAL)	± 0.002	± 0.0002	$^{+0.3}_{-0.2}$	± 0.0008	$\pm 1.$	± 0.000
reweighting of $N_{\gamma_{ECAL}}$	± 0.036	$+0.0021$	$+7.4$	-0.0025	$-2.$	-0.021
total	$^{+0.214}_{-0.156}$	± 0.007	$^{+36.}_{-29.}$	$^{+0.034}_{-0.041}$	$^{+60.}_{-63.}$	$^{+0.143}_{-0.161}$

Table 11.3: *Systematic errors on the fit parameters of the simultaneous fit. The numbers for* $\Delta\mathrm{BR}(B_J^* \to B^{(*)}\pi\pi)$ *have to be multiplied by 0.75 to account for double counting (see also Section 8.3). The total systematic error of of each fit parameter is the quadratic sum of the individual errors.*

11.4 Systematic errors of the $B\pi^+\pi^-$ analysis

The systematic uncertainty of the $B\pi^+\pi^-$ analysis is dominated by the statistical error of the sideband range normalisation and by experimental uncertainties of light meson production rates decaying into $\pi^+\pi^-$. The errors that have been taken into account for the determination of the product branching ratio are listed in Table 11.4. Details can be found in [61].

source	range	relative error
relative error on selection efficiency		
Monte Carlo statistics		3 %
variation of cut values		4 %
fragmentation model		2 %
relative error on b-purity		
conservative estimate		4 %
relative error on production rate		
sideband normalisation 6.05 – 7.05 GeV/c^2	stat. error	18.3 %
variation of sideband normalisation range	$\pm$200 MeV/c^2	4 %
production rate of ρ^0	$\pm$ 10%	10.2 %
production rate of K_s	$\pm$ 5%	1.2 %
production rate of η	$\pm$ 10%	2.4 %
production rate of η'	$\pm$ 15%	1.4 %
production rate of ω	$\pm$ 10%	7.8 %
variation of cut values		8 %
variation of selection efficiency		7 %
Bose-Einstein correlations		8 %
total systematic error		27 %

Table 11.4: *Sources of systematic error on the product branching ratio* $f(\bar{b} \to B^{(*)\prime}, B^*_J) \cdot BR(B^{(*)\prime}, B^*_J \to B^{(*)}\pi^+\pi^-)$ *[61].*

Chapter 12

Summary and Conclusion

The $B\gamma$, $B\pi^{\pm}$ and $B\pi^{\pm}\pi^{\mp}$ final states have been analysed to reconstruct excited B meson states without strangeness. Due to improved b tagging and B reconstruction methods a sample of inclusively reconstructed B mesons is available with a B direction and energy resolution competitive to other LEP analyses but with superior statistics. A new conversion finder optimised for the energy range below 1 GeV and a reconstruction algorithm for low energetic neutral clusters in the OPAL electromagnetic calorimeter have been used to collect the largest sample of B^* mesons to date. Orbitally-excited B mesons have been analysed by forming combinations of inclusively reconstructed B mesons and charged pions. A new way to determine the combinatorial $B\pi$ background while maintaining high statistics has been presented. The high statistics tag of the decay $B^* \to B\gamma$ is used to obtain B^*_J samples enriched or depleted in their B^* content. For the first time the branching ratio of orbitally-excited B mesons decaying into B^* is measured. The result is

$$\mathrm{BR}(\mathrm{B}^*_J \to \mathrm{B}^*\pi(\pi)) = 0.85\,^{+0.26}_{-0.27} \pm 0.12\,,$$

where the first error is statistical and the second systematic. The measurement does not depend on the shape of $B\pi$ mass distributions or on any specific model. It is in agreement with theoretical predictions and the measured B^* and B^*_J production rates at LEP.

Making further use of the additional B^* information, a simultaneous fit to the B^*_J mass spectra of samples enriched or depleted in their B^* content is performed. In this fit, the masses, widths and production rates of the $B_1(1/2)$ and B^*_2 are constrained to the corresponding properties of their doublet partners B^*_0 and $B_1(3/2)$, respectively. The fit yields

$$\begin{aligned} M(\mathrm{B}_1(3/2)) &= (\,5.738\,^{+\,0.005}_{-\,0.006} \pm 0.007\,)\ \mathrm{GeV}/c^2 \\ \Gamma(\mathrm{B}_1(3/2)) &= (\,18\,^{+\,15\,+\,36}_{-\,13\,-\,29}\,)\ \mathrm{MeV}/c^2 \\ \mathrm{BR}(\mathrm{B}^*_J \to \mathrm{B}^*\pi) &= 0.74\,^{+\,0.12\,+\,0.21}_{-\,0.10\,-\,0.16}\,. \end{aligned}$$

The first error indicates the statistical and the second error the systematic uncertainty. The fit favours a notable contribution of $B_J^* \to B^{(*)}\pi\pi$ decays to the B_J^* signal and a mass of the broad B_J^* states about 100 MeV/c^2 above the narrow B_J^* states. Systematic uncertainties of the reconstruction efficiency and the combinatorial background at low $B\pi$ masses together with a lack of knowledge of the exact functional form of the broad B_J^* states at $B\pi$ threshold do not allow an unambiguous determination of the width and mass of the B_0^* (or $B_1(1/2)$). The fit results are in agreement with predictions from several HQET models. The $M(B_1(3/2))$ result agrees well with a measurement of $M(B_2^*)$ [58]. On the other hand, a recent B_J^* analysis [28] presented masses that disagree with the results of this analysis and with [58]. The measured value of $BR(B_J^* \to B^{(*)}\pi\pi) = 0.25 \pm 0.03 \,^{+\,0.11}_{-\,0.12}$ is consistent with the range 0.1-0.2 predicted by theory [43, 44] and in agreement with an experimental result obtained from the reconstruction of the $B^{(*)}\pi\pi$ final state [27, 60]. The results for $BR(B_J^* \to B^*\pi(\pi))$, $BR(B_J^* \to B^*\pi)$ and $BR(B_J^* \to B^{(*)}\pi\pi)$ are in good agreement with each other, even if large correlations between the errors of the different quantities are assumed.

A signal excess of entries in the $B\pi^+\pi^-$ mass distribution has been obtained by subtraction of the $B\pi^+\pi^+$ like-sign background from the $B\pi^+\pi^-$ unlike-sign sample. The observed signal is interpreted as a combined signal of $B^{(*)\prime} \to B^{(*)}\pi^+\pi^-$ and $B_J^* \to B^{(*)}\pi^+\pi^-$ decays. The measured product branching ratio is

$$f(\bar{b} \to B^{(*)\prime}, B_J^*) \cdot BR(B^{(*)\prime}, B_J^* \to B^{(*)}\pi^+\pi^-) = 0.0350 \pm 0.0070 \pm 0.0095 \ ,$$

where the first error is statistical and the second systematic. This result of the product branching ratio is in agreement with the value for $BR(B_J^* \to B^{(*)}\pi\pi)$ obtained from the fit and $f(\bar{b} \to B_J^*) = 0.25 \pm 0.03$.

Besides the quoted states, no other exited B mesons have been observed in the analysed final states. This thesis covers all low lying non-strange B meson states accessible with the experimental data currently available.

Appendix A

Event Display Pictures

This appendix contains displays of LEP1 events recorded with the OPAL detector. Tracks measured in the central tracking system are shown in light blue. Clusters of energy in the lead glass electromagnetic calorimeter are shown as yellow boxes, of size proportional to their energy. Similarly, clusters of energy in the hadron calorimeter are drawn in magenta, and signals in the time-of-flight system in green. The header of each event display contains the run and event number as well as some basic quantities like beam energy and the number of charged tracks.

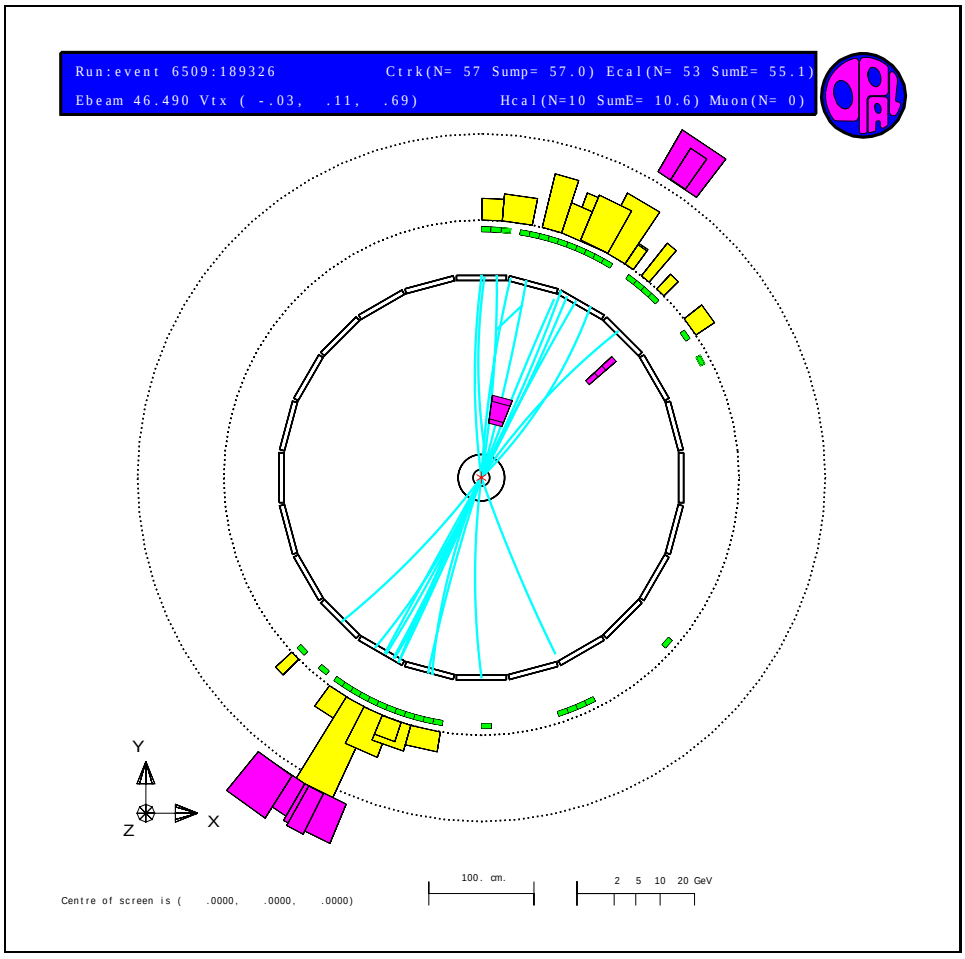

Figure A.1: *Multi-hadronic* Z^0 *decay. A high track multiplicity and high activity in the calorimeters are the characteristics of a* $Z^0 \to q\bar{q}$ *event. A clear 2-jet topology is observed, corresponding to the two primary quarks produced in the decay.*

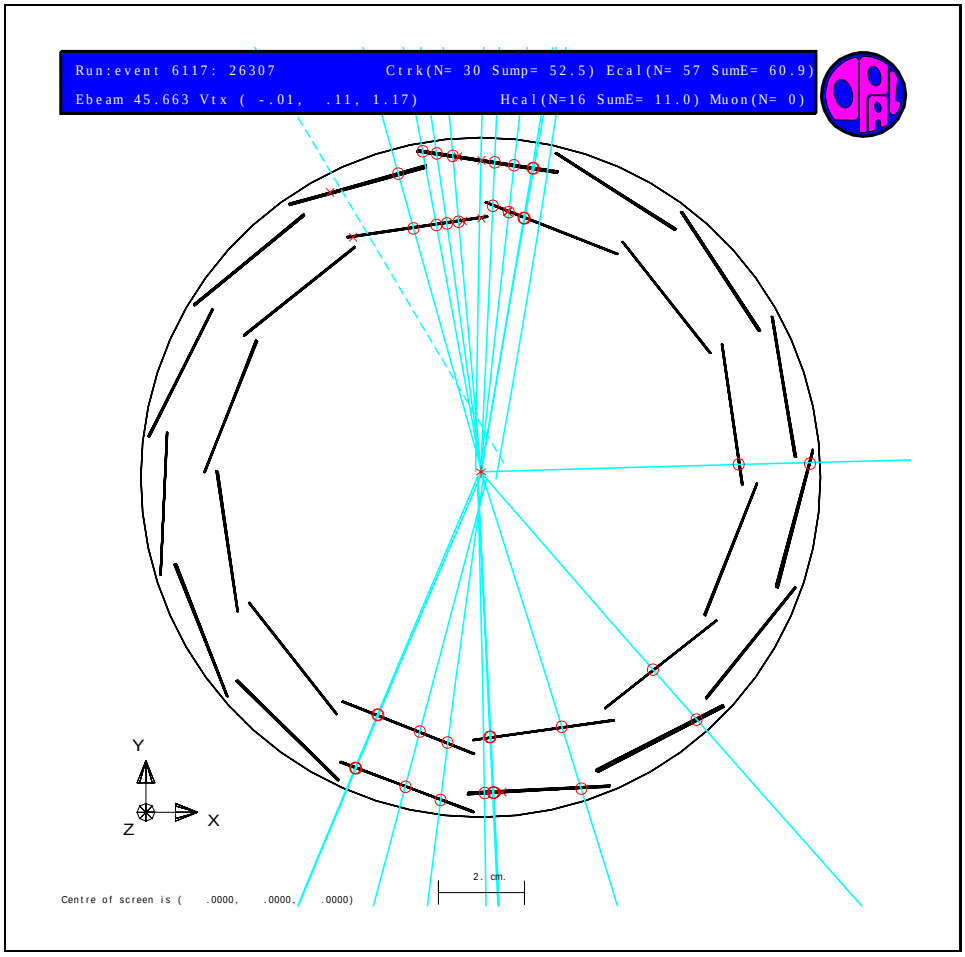

Figure A.2: *Reconstructed tracks of a* $Z^0 \to b\overline{b}$ *event in the inner part of the tracking system. Silicon microvertex hits are indicated in red on the silicon wafers. The interaction point (indicated in red) is close to the origin of the coordinate system. A separated secondary vertex is reconstructed at about* $(x, y) = (0\,cm, -1\,cm)$.

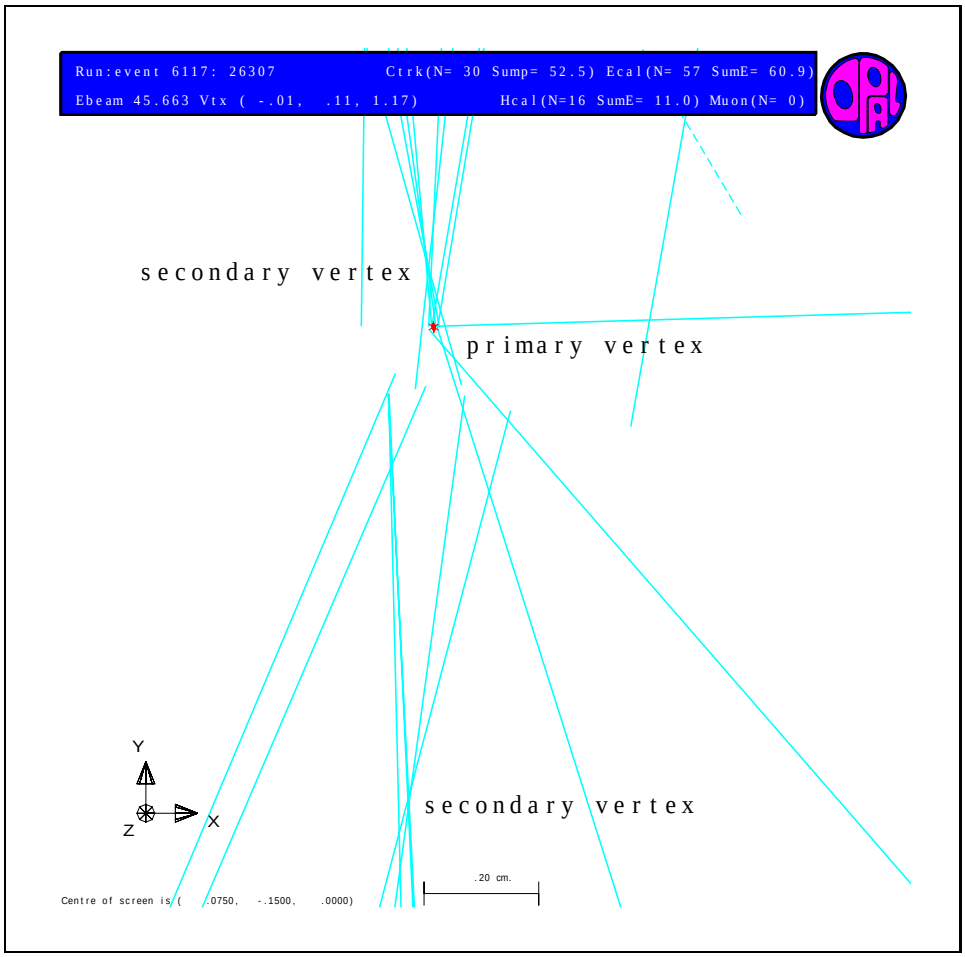

Figure A.3: *Close-up view of the* e^+e^- *interaction region of the same* $Z^0 \to b\overline{b}$ *event shown on the previous page. In the second jet there is also a secondary vertex observed at a distance of about 1 mm from the interaction point. The probability for this event to be a* $Z^0 \to b\overline{b}$ *decay is larger than 0.99.*

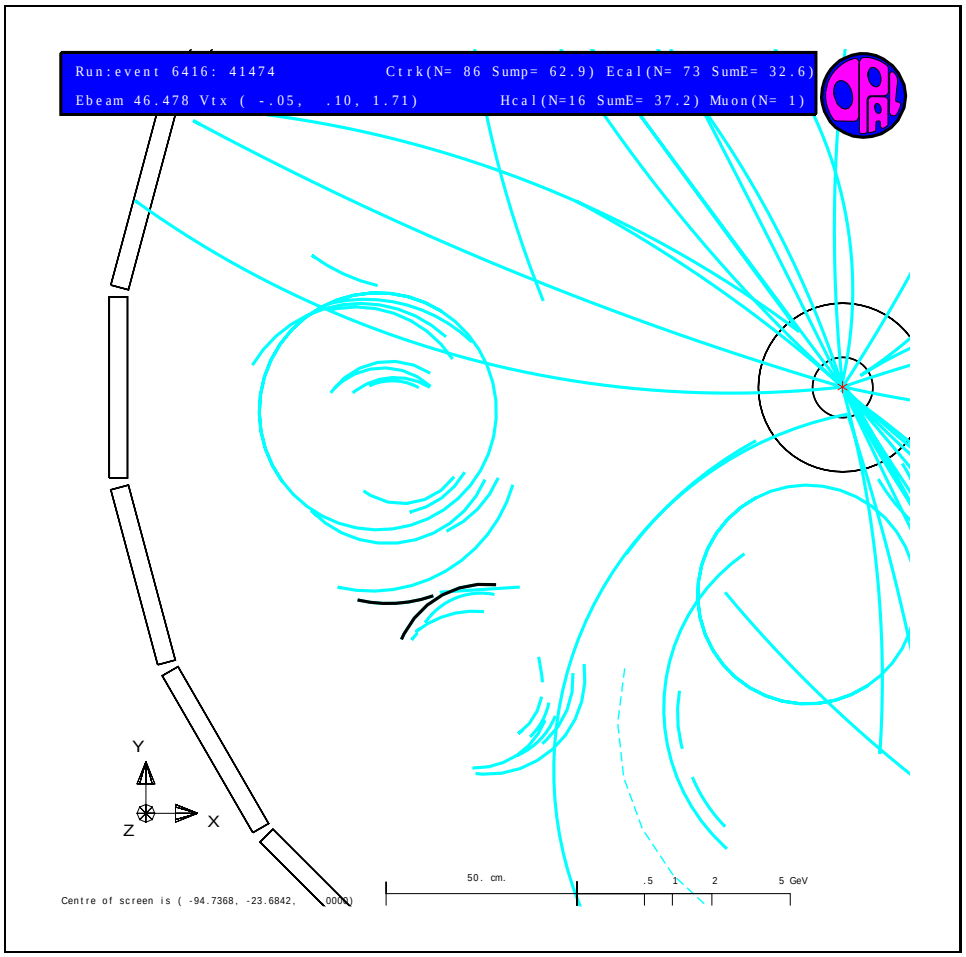

Figure A.4: *Curling of low p_t tracks in CJ. The conversion finder picks up the right track combination highlighted in black.*

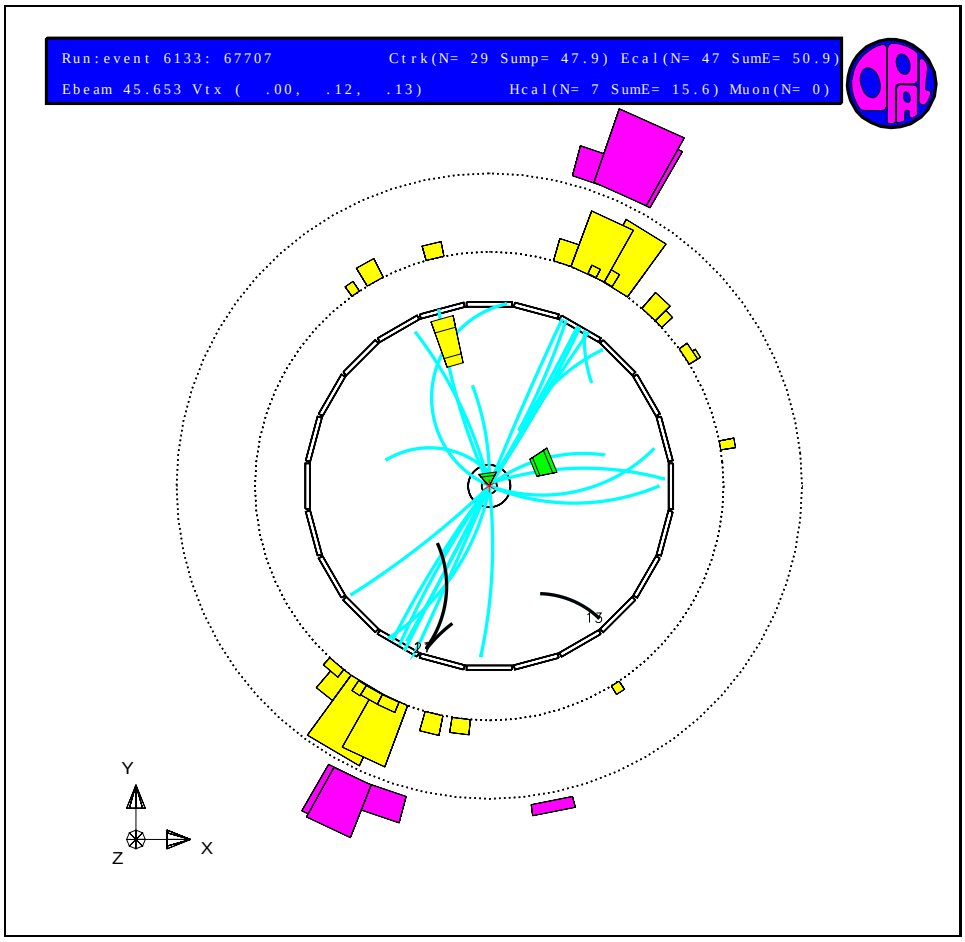

Figure A.5: *A* $Z^0 \to b\overline{b}$ *decay with a conversion candidate originating from material of the outer CJ shell. The corresponding tracks are highlighted in black. The electron track is fragmented in two parts since the track passes CJ sector boundaries and the reconstruction algorithm tends to build tracks in radial direction. Note that the direction of the photon candidate does not point to the primary event vertex. Conversions of this type are produced by hadrons hitting a nucleus in the material of the tracking system. Many low energetic protons, neutrons and pions emerge from the interaction region and eventually a photon from a* π^0 *decay heading back into the tracking system converts into* e^+e^-.

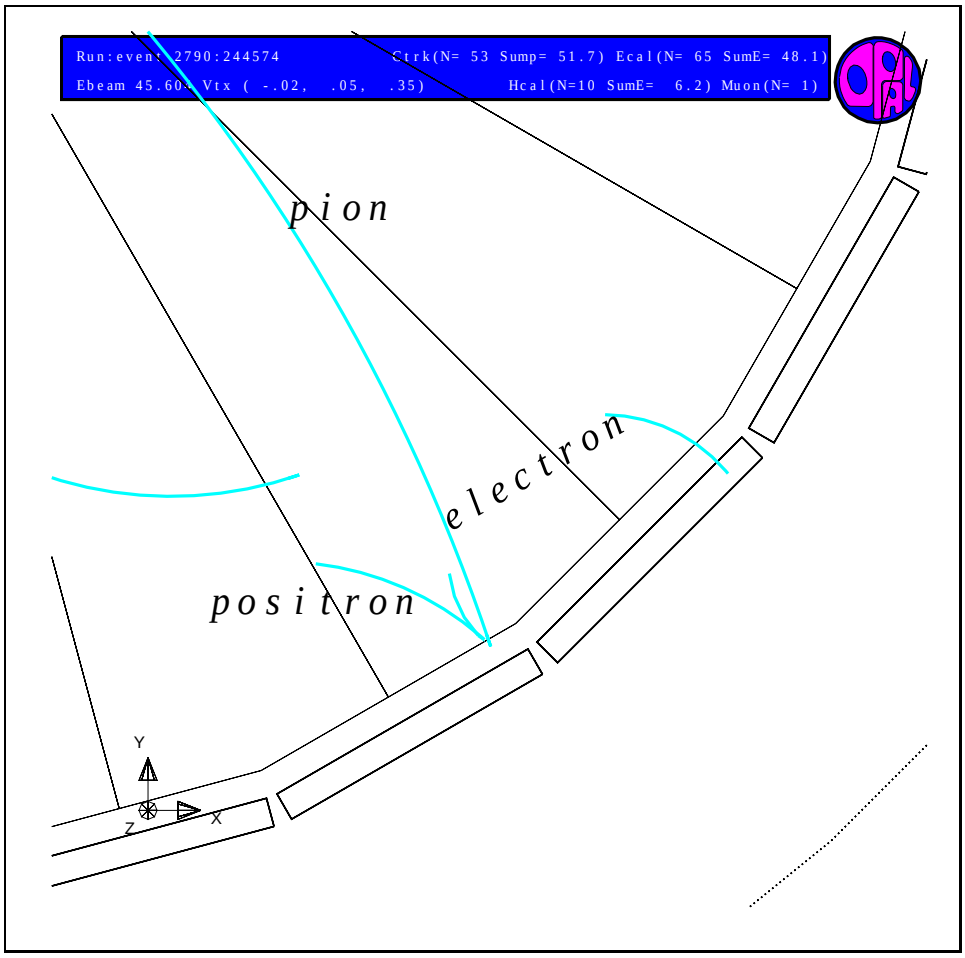

Figure A.6: *Close-up view of a conversion originating from material of the outer CJ shell (Monte Carlo). This simulated conversion corresponds to the data candidate shown in Figure A.5.*

Bibliography

[1] S. L. Glashow. *Nucl. Phys.* **22**, 579 (1961).

[2] P. W. Higgs. *Phys. Lett.* **12**, 132 (1964).

[3] P. W. Higgs. *Phys. Rev. Lett.* **13**, 508 (1964).

[4] T. W. B. Kibble. *Phys. Rev.* **155**, 1554 (1967).

[5] S. Weinberg. *Phys. Rev. Lett* **19**, 1264 (1967).

[6] A. Salam. "Elementary Particle Theory". Almquist and Wiksells, Stockholm (1968).

[7] S. L. Glashow, J. Iliopoulos, and L. Maiani. *Phys. Rev.* **D2**, 1285 (1970).

[8] G. 't Hooft. *Nucl. Phys.* **B33**, 173 (1971).

[9] G. 't Hooft. *Nucl. Phys.* **B35**, 167 (1971).

[10] R. Gupta. *hep-lat* **9807028** (1998). Lectures given at Les Houches Summer School in Theoretical Physics, Session 68: Probing the Standard Model of Particle Interactions, Les Houches, France, 28 Jul - 5 Sep 1997.

[11] J. Mnich. Tests of the standard model. *CERN preprint* **EP-99-143** (1999).

[12] See for example:
OPAL Collaboration. *OPAL Physics Note* **PN421**, (1999). Updated information on Higgs searches of LEP experiments is available at: http://www.cern.ch/LEPHIGGS/.

[13] P. Fisher, B. Kayser, and K. S. McFarland. *hep-ph* **9906244** (1999). Overview, submitted to Ann. Rev. Nucl. Part. Sci.

[14] Y. Nir. Flavour Physics and CP Violation. In "Proceedings of the 1998 European School of High-energy Physics", St. Andrews, Scotland (1998).

[15] A. F. Falk. *hep-ph* **9812217** (1998). Article taken from an introductory chapter of *The BaBar Physics Book*, SLAC-R-504.

[16] J. F. Donoghue, E. Golowich, and B. R. Holstein. "Dynamics of the Standard Model". Cambridge University Press, Cambridge (1992).

[17] T. Muta. "Foundations of Quantum Chromodynamics". Worl Scientific Publishing, Singapore (1987).

[18] W. Marciano and H. Pagels. *Phys. Rept.* **36**, 137 (1978).

[19] S. G. Gorishny. et al. *JETP Lett.* **53**, 127 (1991).

[20] S. Collins et al. *Phys. Rev.* **D60**, 074504 (1999).

[21] A. Ali Khan et al. *Nucl. Phys. Proc. Suppl.* **73**, 345 (1999). and in preparation.

[22] K. Wilson. *Phys. Rev.* **179**, 1499 (1969).

[23] M. Neubert. *hep-ph* **9610385** (1996). Published in Proceedings of the 20$^{\text{th}}$ Johns Hopkins Workshop on Current Problems in Particle Theory, World Scientific, Singapore, 1997.

[24] A. F. Falk. *hep-ph* **9609380** (1996). Published in Proceedings of the 20$^{\text{th}}$ Johns Hopkins Workshop on Current Problems in Particle Theory World Scientific, Singapore, 1997.

[25] D. Ebert, V.O. Galkin, and R.N. Faustov. *Phys. Rev.* **D57**, 5663 (1998). *Erratum* Phys. Rev. **D59** (1999) 019902.

[26] Particle Data Group. C. Caso et al. *Eur. Phys. J.* **C3**, 1 (1998).

[27] G. Eigen. *Int. J. Mod. Phys.* **A12**, 3909 (1997).

[28] L3 Collaboration. M. Acciarri et al. *Phys. Lett.* **B465**, 323 (1999).

[29] K. G. Chetyrkin et al. *Phys. Rept.* **277**, 189 (1996).

[30] B. Andersson, G. Gustafson, and C. Peterson. *Z. Phys.* **C1**, 105 (1979).

[31] C. Peterson et al. *Phys. Rev.* **D27**, 105 (1983).

[32] M. Volonshin and M. Shifman. *Sov. J. Nucl. Phys.* **45**, 292 (1987).

[33] M. Volonshin and M. Shifman. *Sov. J. Nucl. Phys.* **47**, 511 (1988).

[34] S. Nussinov and W. Wetzel. *Phys. Rev.* **D36**, 130 (1987).

[35] N. Isgur and M.B. Wise. *Phys. Lett.* **B232**, 113 (1989).

[36] N. Isgur and M.B. Wise. *Phys. Lett.* **B237**, 527 (1990).

[37] N. Isgur and M.B. Wise. *Phys. Rev. Lett.* **66**, 1130 (1991).

[38] E. Eichten and B. Hill. *Phys. Lett.* **B234**, 511 (1990).

[39] B. Grinstein. *Nucl. Phys.* **B339**, 253 (1990).

[40] H. Georgi. *Phys. Lett.* **B240**, 447 (1990).

[41] A. Falk et al. *Nucl. Phys.* **B343**, 1 (1990).

[42] J.D. Bjorken, I. Dunietz, and J. Taron. *Nucl. Phys.* **B371**, 111 (1990).

[43] E.J. Eichten, C.T. Hill, and C. Quigg. *Phys. Rev. Lett* **71**, 4116 (1993).

[44] E.J. Eichten, C.T. Hill, and C. Quigg. *FERMILAB-CONF* **94-117-T** (May 1994).

[45] S. Godfrey and R. Kokoski. *Phys. Rev.* **D43**, 1679 (1991).

[46] S. Godfrey and N. Isgur. *Phys. Rev.* **D32**, 189 (1985).

[47] M. Gronau and J. Rosner. *Phys. Rev.* **D49**, 254 (1994).

[48] N. Gupta and J.M. Johnson. *Phys. Rev.* **D51**, 168 (1995).

[49] A.F. Falk and T.Mehen. *Phys. Rev.* **D53**, 231 (1996).

[50] Y.-B. Dai and S.-L. Zhu. *Phys. Rev.* **D58**, 074009 (1998).

[51] Y.-B. Dai. et al. *Phys. Rev.* **D58**, 094032 (1998). *Erratum* Phys. Rev. **D59** (1999) 059901.

[52] N. Isgur. *Phys. Rev.* **D57**, 4041 (1998).

[53] A. H. Orsland and H. Hogaasen. *Eur. Phys. J.* **C9**, 503 (1999).

[54] DELPHI Collaboration. P. Abreu et al. *Z. Phys.* **C68**, 353 (1995).

[55] Y.-J. Pei. *Z. Phys.* **C72**, 39 (1996).

[56] OPAL Collaboration. G. Alexander et al. *Z. Phys.* **C66**, 19 (1995).

[57] DELPHI Collaboration. P. Abreu et al. *Phys. Lett.* **B345**, 598 (1995).

[58] ALEPH Collaboration. R. Barate et al. *Phys. Lett.* **B425**, 215 (1998).

[59] ALEPH Collaboration. D. Buskulic et al. *Z. Phys.* **C69**, 393 (1996).

[60] M.-L. Andrieux. *Nucl. Phys. B (Proc. Suppl.)* **55A**, 51 (1997).

[61] A. Leins. Suche nach der ersten radialen Anregung von B- und B*-Mesonen mit dem OPAL-Detektor. Diplomarbeit Albert-Ludwigs Universität Freiburg, (April 1999).

[62] W. Schnell. *IEEE Trans. Nucl. Sci.* **26**, 3130 (1979).

[63] S. Meyers. The LEP Collider, from Design to Commissioning. *Available at:* http://www.cern.ch/CERN/Divisions/SL/history/sl_hist.html (1991 (updated 1995)).

[64] ALEPH Collaboration. D. Decamp et al. *Nucl. Instrum. Meth.* **A294**, 121 (1990).

[65] L3 Collaboration. B. Adeva et al. *Nucl. Instrum. Meth.* **A289**, 35 (1990).

[66] DELPHI Collaboration. P. Aarnio et al. *Nucl. Instrum. Meth.* **A303**, 233 (1991).

[67] OPAL Collaboration. K. Ahmet et al. *Nucl. Instrum. Meth.* **A305**, 275 (1991).

[68] R. Ley. Cern accelerators. Figure courtesy of R. Ley, CERN PS Division. (1996).

[69] H. Burkhardt. Lep1 operation, 1989-1995. In "Proceedings of the 5$^{\text{th}}$ European Particle Accelerator Conference, EPAC 96" (1996).

[70] S. L. Lloyd. The OPALPrimer. Technical Report, (1998).

[71] P. P. Allport et al. *Nucl. Instrum. Meth.* **A324**, 34 (1993).

[72] P. P. Allport et al. *Nucl. Instrum. Meth.* **A346**, 476 (1994).

[73] H. M. Fischer et al. *Nucl. Instrum. Meth.* **A283**, 492 (1989).

[74] M. Hauschild et al. *Nucl. Instrum. Meth.* **A314**, 74 (1992).

[75] O. Biebel et al. *Nucl. Instrum. Meth.* **A323**, 169 (1992).

[76] H. Drumm et al. *Nucl. Instrum. Meth.* **A176**, 333 (1980).

[77] S. Weigel. Erstellung eines Hochspannungs-Monitorprogrammes für den OPAL-Detektor. Zulassungsarbeit Albert-Ludwigs Universität Freiburg, (Mai 1997).

[78] M. Hauschild. The opal jet chamber performance. *Available at:* http://opalinfo.cern.ch/opal/group/cj/faq/performance.html (last update 1998).

[79] M. Arignon et al. *Nucl. Instrum. Meth.* **A313**, 103 (1992).

[80] D. G. Charlton et al. *Nucl. Instrum. Meth.* **A315**, 129 (1993).

[81] M. Arignon et al. *Nucl. Instrum. Meth.* **A333**, 330 (1993).

[82] J. Allison et al. *Nucl. Instrum. Meth.* **A317**, 47 (1992).

[83] D. R. Ward. "A GOPAL Primer". *Available at:* http://www.cern.ch/opal/manuals/go/pro/go133.html (last update 1995).

[84] CERN Computing and Networks Division Application Software Group. "GEANT - Detector Description and Simulation Tool". CERN Program Library Long Writeup W5013. *Available at:* http://wwwinfo.cern.ch/asd/geant/ (1995).

[85] OPAL Collaboration. G. Alexander et al. *Z. Phys.* **C52**, 175 (1991).

[86] N. Brown and W. J. Stirling. *Phys. Lett.* **B252**, 657 (1990).

[87] S. Bethke. et al. *Nucl. Phys.* **B370**, 310 (1992). *Erratum* Nucl. Phys. **B523** (1998) 681.

[88] S. Catani. et al. *Phys. Lett.* **B269**, 432 (1991).

[89] N. Brown and W. J. Stirling. et al. *Z. Phys.* **C53**, 629 (1992).

[90] OPAL Collaboration. K. Ackerstaff et al. *Eur. Phys. J.* **C2**, 213 (1998).

[91] OPAL Collaboration. G. Abbiendi et al. *Eur. Phys. J.* **C7**, 407 (1999).

[92] OPAL Collaboration. K. Ackerstaff et al. *Z. Phys.* **C74**, 1 (1997).

[93] OPAL Collaboration. G. Abbiendi et al. *Eur. Phys. J.* **C8**, 217 (1999).

[94] S. Yamashita and I. Nakamura. LB160: Upgraded b-tagging for LEP 2. Technical Note TN578, OPAL internal (November 1998).

[95] OPAL Collaboration. K. Ackerstaff et al. *Z. Phys.* **C74**, 413 (1997).

[96] OPAL Collaboration. R. Akers et al. *Z. Phys.* **C63**, 197 (1994).

[97] S. Robins. Inclusive Reconstruction of b Hadrons. Technical Note TN594, OPAL internal (January 1999).

[98] C. Peterson, T. Rögnvaldsson, and L. Lönnblad. *Comp. Phys. Comm.* **81**, 185 (1994).

[99] OPAL Collaboration. K. Ackerstaff et al. *Eur. Phys. J.* **C5**, 411 (1998).

[100] OPAL Collaboration. K. Ackerstaff et al. *Z. Phys* **C74**, 413 (1997).

[101] OPAL Collaboration. G. Alexander et al. *Z. Phys* **C73**, 587 (1997).

[102] OPAL Collaboration. G. Alexander et al. *Z. Phys* **C70**, 357 (1996).

[103] O. Cooke and C. Jones. Neural Network Electron and Photon Conversion Identification. Technical Note TN556, OPAL internal (July 1998).

[104] OPAL Collaboration. K. Ackerstaff et al. *Eur. Phys. J.* **C5**, 411 (1998).

[105] OPAL Collaboration. K. Ackerstaff et al. *Z. Phys.* **C74**, 413 (1997).

[106] ALEPH Collaboration. Buskulic et al. *Z. Phys.* **C69**, 393 (1996).

[107] L3 Collaboration. M. Acciarri et al. *Phys. Lett.* **B345**, 589 (1995).

[108] CUSB-II Collaboration. J. Lee-Franzini et al. *Phys. Rev. Lett.* **65**, 2947 (1990).

[109] M. Thiergen. B Spectroscopy and Glueball Searches with the OPAL Detector at LEP. In "Proceedings of the 8^{th} Internatioanl Conference on Hadron Spectroscopy (HADRON 99)". To be published in Nucl. Phys. A (2000).

[110] OPAL Collaboration. R. Akers et al. *Phys. Lett.* **B316**, 435 (1993).

[111] R. Kokoski and N. Isgur. *Phys. Rev.* **D35**, 907 (1987).

[112] CLEO Collaboration. S. Anderson et al. *CLEO conference report* **CLEO-CONF-99-6** (August 1999).

[113] Threshold factors of this type can be found in:
T. Sjöstrand. *Comp. Phys. Comm.* **82**, 74 (1994).

[114] For mass fits the MINUIT package is used:
F. James and M. Roos. *Comput. Phys. Comm.* **10**, 343 (1975).

[115] G. Bauer. (for the CDF Collaboration). *hep-ex* **9909014** (1999).

[116] D. Vučinić. "Observation of Excited B Mesons in $p\bar{p}$ Collisions at $\sqrt{s} = 1.8$ TeV". PhD thesis, Massechusetts Institute of Technology (February 1999).

[117] OPAL Collaboration. contributed paper to HEP99, Tampere and HADRON99, Beijing. *OPAL Physics Note* **PN400** (1999).

[118] DELPHI Collaboration. P. Abreu et al. *Phys. Lett.* **B426**, 231 (1998).

[119] OPAL Collaboration. *OPAL Physics Note* **PN352** (1998).

[120] M. Thiergen. Recent opal results on charm spectroscopy. *Frascati Physics Series* **Vol. XV**, 295 (1999).

[121] J. L. Rodriguez. Hadronic decays of beauty and charm from cleo. *hep-ex* **9901008** (1999).

[122] A.F. Falk and M. E. Peskin. *Phys. Rev.* **D49**, 3320 (1994).

[123] OPAL Collaboration. G. Abbiendi et al. *Eur. Phys. J.* **C8**, 573 (1999).

[124] DELPHI Collaboration. P. Abreu et al. *Phys. Lett.* **B425**, 399 (1998).

[125] L3 Collaboration. Acciari et al. *Phys. Lett.* **B416**, 220 (1998).

[126] OPAL Collaboration. R. Akers et al. *Zeit. Phys.* **C61**, 209 (1994).